Operando-informed precatalyst programming strategies towards reliable high current density electrolysis

Lu Xia,[1, 2, #] Bruna Ferreira Gomes,[3, #] Wulyu Jiang,[1, #] Daniel Escalera-López,[5] Yang Wang,[4] Yang Hu,[8] Alaa Y. Faid,[6] Kaiwen Wang,[2] Tengyu Chen,[2] Kaiqi Zhao,[2] Xu Zhang,[9] Yingtang Zhou,[7] Ranit Ram,[2] Barbara Polesso,[2] Anku Guha,[2] Jiaqi Su,[10] Carlos M. S. Lobo,[3] Michael Haumann,[11] Robert Spatschek,[8] Svein Sunde,[6] Lin Gan,[12] Ming Huang,[13] Xiaoyuan Zhou,[4] Christina Roth, [3] Werner Lehnert,[1] Serhiy Cherevko,[5] Liyong Gan,[4, *] F. Pelayo García de Arquer,[2, *] and Meital Shviro[1, ¥ *]

[1]Institute of Energy and Climate Research, Electrochemical Process Engineering (IEK-14), Forschungszentrum Jülich GmbH, 52425 Jülich, Germany

[2]ICFO–Institut de Ciències Fotòniques, The Barcelona Institute of Science and Technology, 08860 Castelldefels, Barcelona, Spain

[3]Electrochemical Process Engineering, University of Bayreuth, 95447 Bayreuth, Germany

[4]College of Physics and Center of Quantum Materials and Devices, Chongqing University, Chongqing 401331, P. R. China

[5]Helmholtz-Institute Erlangen-Nürnberg for Renewable Energy (IEK-11), Forschungszentrum Jülich GmbH, Erlangen 91058, Germany

[6]Department of Materials Science and Engineering Norwegian University of Science and Technology, Trondheim N-7491, Norway

[7]National Engineering Research Center for Marine Aquaculture, Marine Science and Technology College, Zhejiang Ocean University, Zhoushan, Zhejiang Province 316004, China

[8]Institute of Energy and Climate Research, Structure and Function of Materials (IEK-2), Forschungszentrum Jülich GmbH, 52425 Jülich, Germany

[9]Beijing Key Laboratory of Microstructure and Properties of Solids, Faculty of Materials and Manufacturing, Beijing University of Technology, Beijing 100124, China.

[10]Department of Health Sciences and Technology, ETH Zurich, Zurich, Switzerland

[11]Department of Physics, Freie Universität Berlin, Arnimallee 14, 14195 Berlin, Germany

[12]Institute of Materials Research, Tsinghua Shenzhen International Graduate School, Tsinghua University, Shenzhen 518055, Guangdong, China

[13]Institute of Fundamental and Frontier Sciences, University of Electronic Science and Technology of China, Chengdu, China

[¥]Current address: Chemistry and Nanoscience Center, National Renewable Energy Laboratory (NREL), Golden, CO 80401, USA

[#]These authors contribute equally

[*]Corresponding Author:

ganly@cqu.edu.cn; pelayo.garciadearquer@icfo.eu; meital.shviro@nrel.gov

Part 1: Synthesis and characterizations

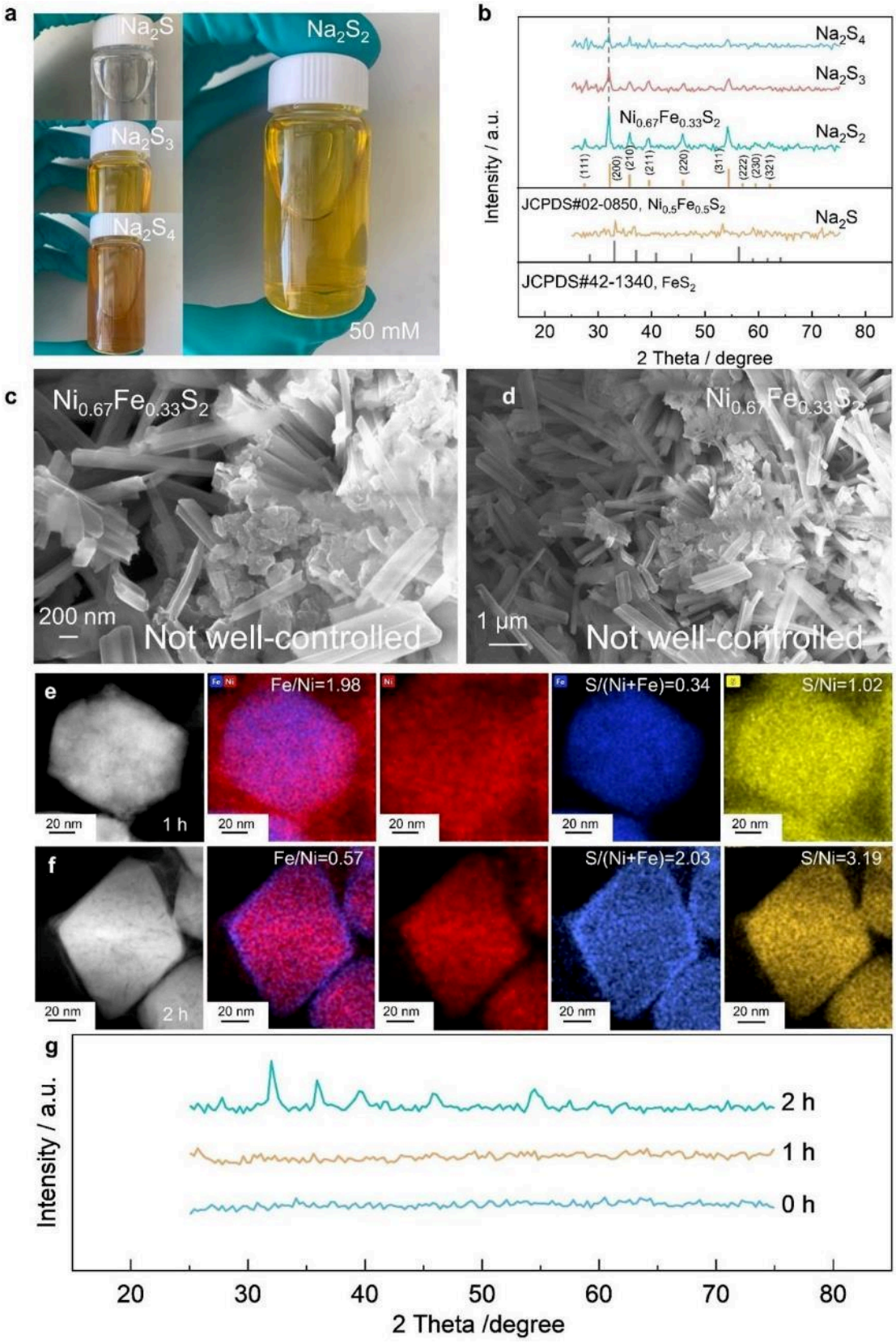

Fig. S1 | Morphology and phase structures at different time. a, Photos of different anion

precursors and **b,** corresponding XRD patterns of obtained $Ni_{0.67}Fe_{0.33}S_2$ catalysts. **c-d,** SEM images for $Ni_{0.67}Fe_{0.33}S_2$ mixture composed of nanorods synthesized by without adding NaOH. HAADF-STEM image of sulfide-based catalysts with the input Ni/Fe ratio of 2:1 after **e,** 1 h and **f,** 2 h of hydrothermal reaction, and corresponding elemental mapping of integrated Ni/Fe and single Ni, Fe, and S. **g,** XRD patterns before and after 1-2 h.

At the beginning, utilizing Na_2S as the anion precursor did not produce crystals after 1-2 hours at 200℃ in an autoclave (**Fig. S1b**). We tried different temperatures from 200-300℃ and still got the same result. Subsequently, we elevated the atomic percentage of sulfur by introducing elemental S to S^{2-}, leading to the formation of either nanorods or a mixture of nanoparticles and nanorods (**Fig. S1c, d**).

Next, we assessed whether the sulfide ion concentration was insufficient and doubled the S^{2-} concentration. Despite these adjustments, we arrived at a similar result as before. Subsequently, we contemplated whether the incorporation of S_x^{2-} was necessary for facilitating crystallization (**Fig. S1a**).

Na_2S_x is synthesized from S^{2-} and S according to a certain stoichiometric ratio (1: x). Since polysulfides exist in the form of mixed ions in the liquid phase, x here is only calculated based on the input ratio, rather than the actual proportion. We observed that, regardless of the value of x, the material exhibits very low crystallinity.

Then we considered that the hydrolysis of S^{2-} ions at elevated temperatures may play a role. Thus, we synthesized Na_2S_x from S^{2-}, NaOH and S according to a certain stoichiometric ratio (1: 1: x). We observed that as the value of x approaches 1, the crystallinity of the material increases over a span of 1-2 hours (**Fig. S1e-g**). In the end, we achieved successful incorporation of Ni ions into the lattice of various amorphous Fe sulfides using S_2^{2-} (atomic ratio of S^{2-}: OH: S=1: 1: 1 for the preparation of S_2^{2-}) for 2 hours at 200℃. This yielded $NixFe_{1-x}S_2$ (0.67, 0.75, 0.80) with a uniform nano-octahedron morphology and similar size.

We identified a crucial step: introducing NaOH during the preparation of S_x^{2-} to prevent the hydrolysis of S^{2-} ions to HS^-/HS^{2-} and HSO^{3-}/HSO^{4-} species at elevated temperatures.

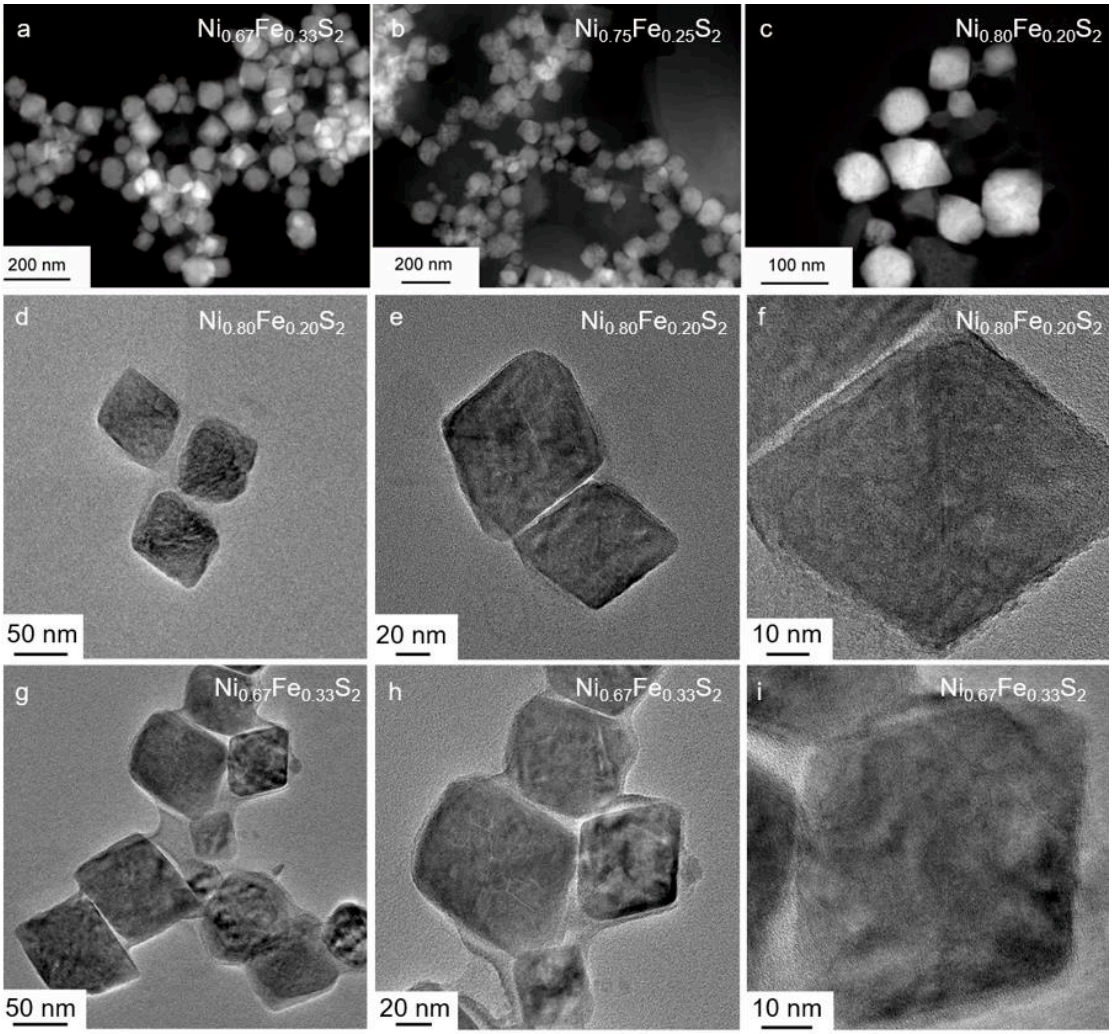

Fig. S2 | Morphology and crystal planes of $Ni_xFe_{1-x}S_2$. a-c, HAADF image of $Ni_xFe_{1-x}S_2$ (0.67, 0.75, 0.80). HRTEM images of **d-f,** $Ni_{0.80}Fe_{0.20}S_2$ and **g-i** $Ni_{0.67}Fe_{0.33}S_2$.

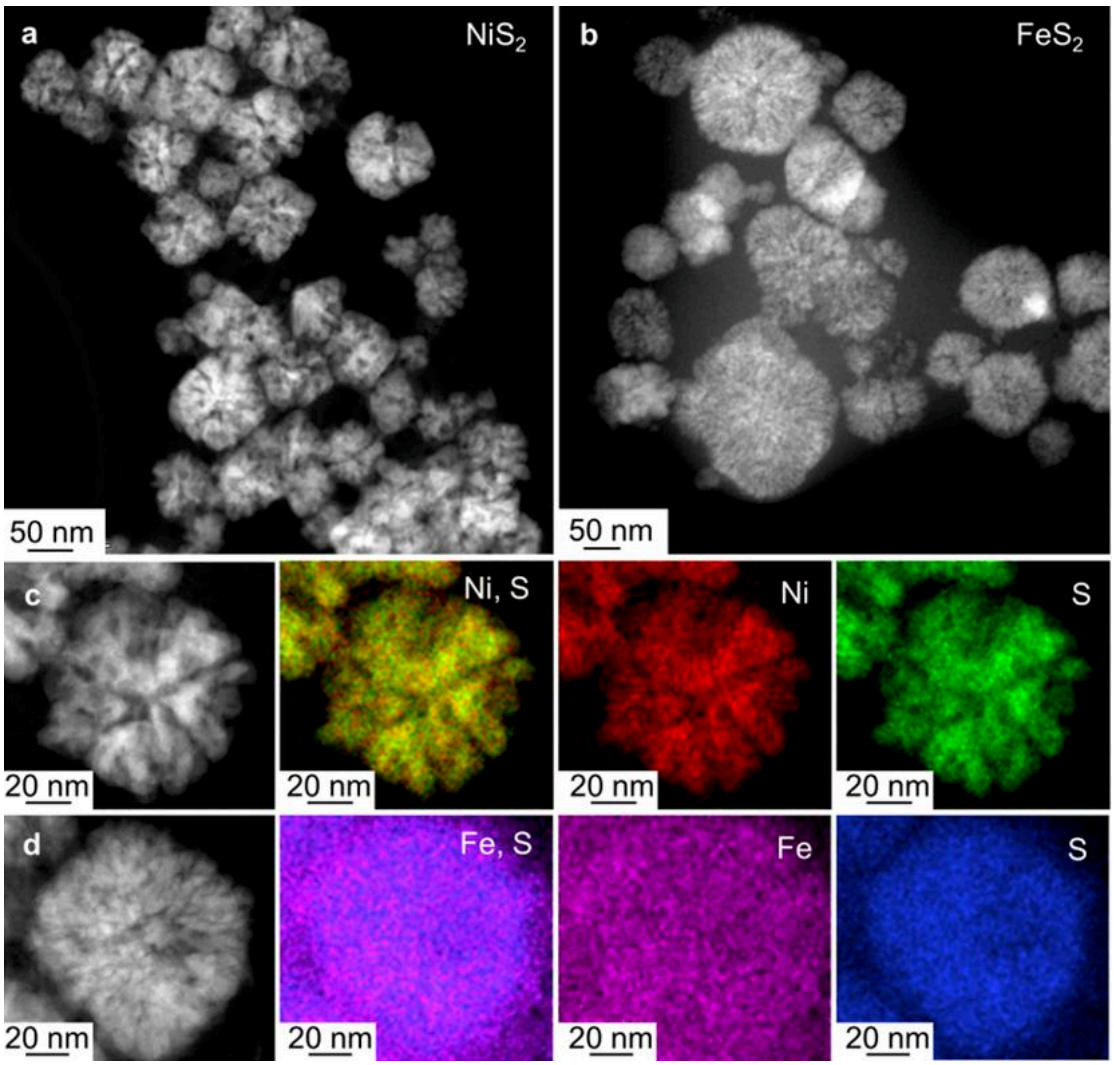

Fig. S3 | Morphology of NiS_2 and FeS_2. HAADF-STEM image of **a, c,** NiS_2 and **b, d,** FeS_2 and corresponding elemental mapping of integrated Ni/S, Fe/S and single Ni, Fe, and S.

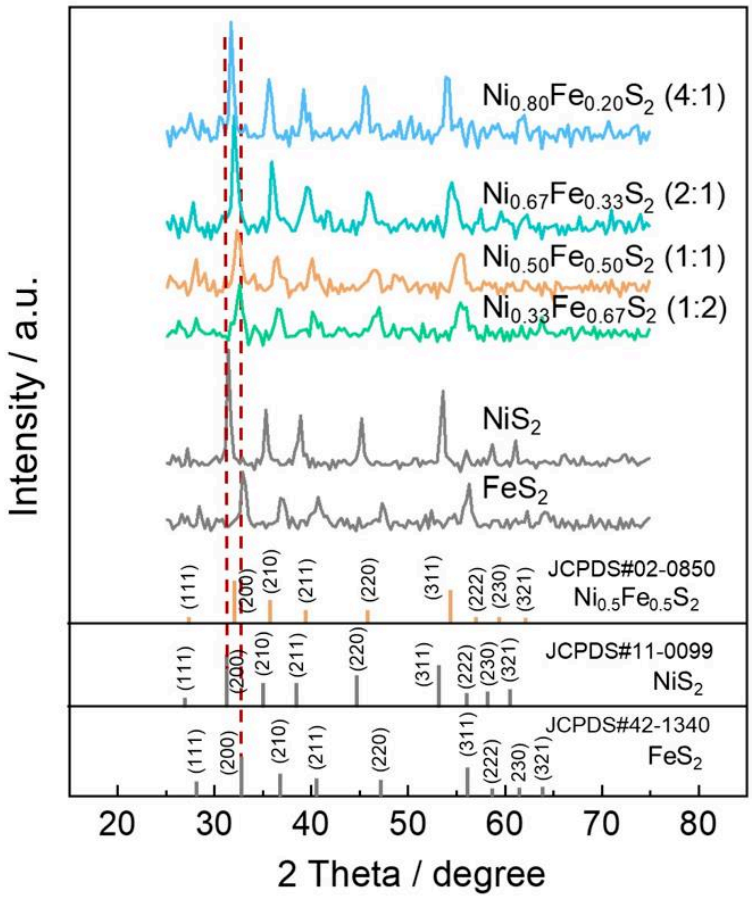

Fig. S4 | Characterizations of phase structures for $Ni_xFe_{1-x}S_2$ (x ranging from 0-1). XRD patterns of $Ni_xFe_{1-x}S_2$ catalysts (x=0.00, 0.33, 0.50, 0.67, 0.80, 1.00) with 2θ degree ranging from 25-75°.

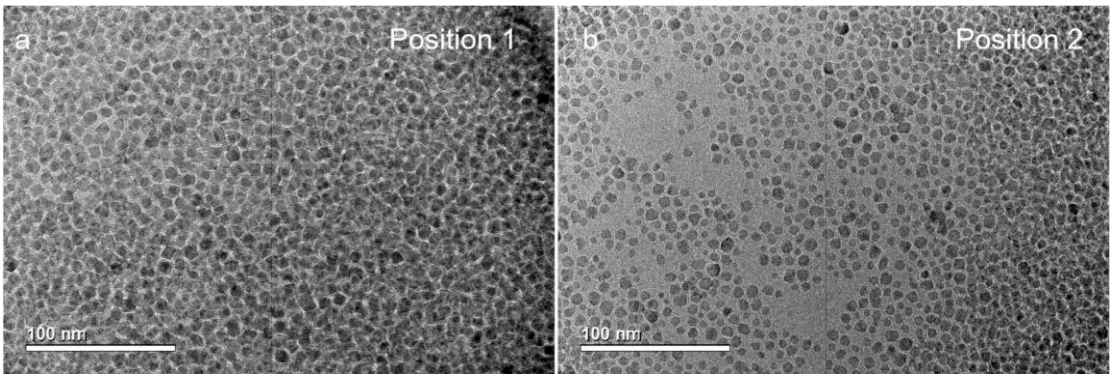

Fig. S5 | Morphology of Fe_3O_4. HRTEM images of Fe_3O_4 in **a,** position 1 and **b,** position 2.

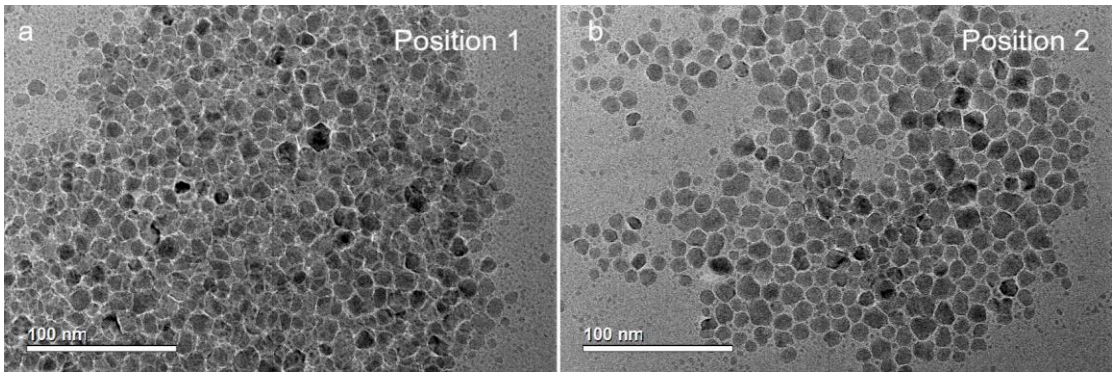

Fig. S6 | Morphology of $NiFe_2O_4$. HRTEM images of $NiFe_2O_4$ in **a,** position 1 and **b,** position 2.

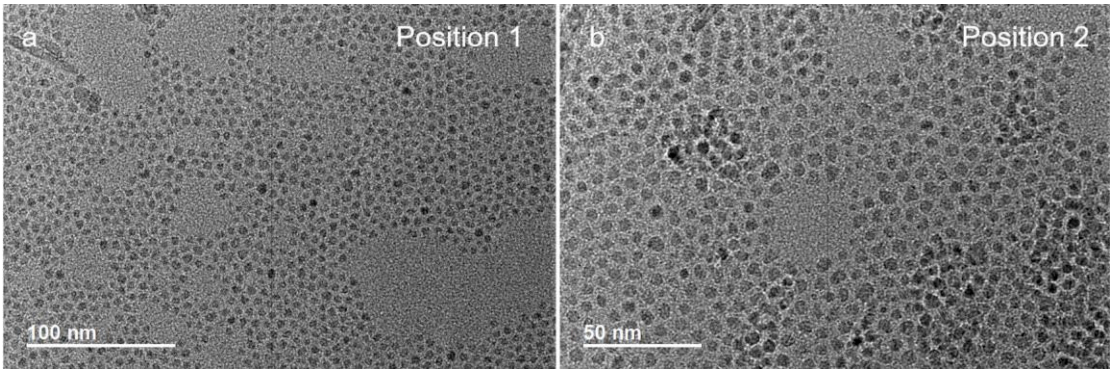

Fig. S7 | Morphology of $CoFe_2O_4$. HRTEM images of $CoFe_2O_4$ in **a,** position 1 and **b,** position 2.

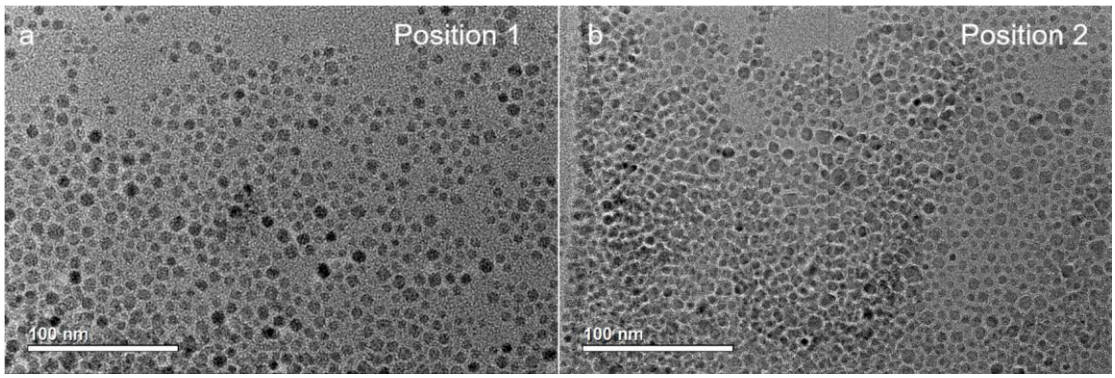

Fig. S8 | Morphology of $MnFe_2O_4$. HRTEM images of $MnFe_2O_4$ in **a,** position 1 and **b,** position 2.

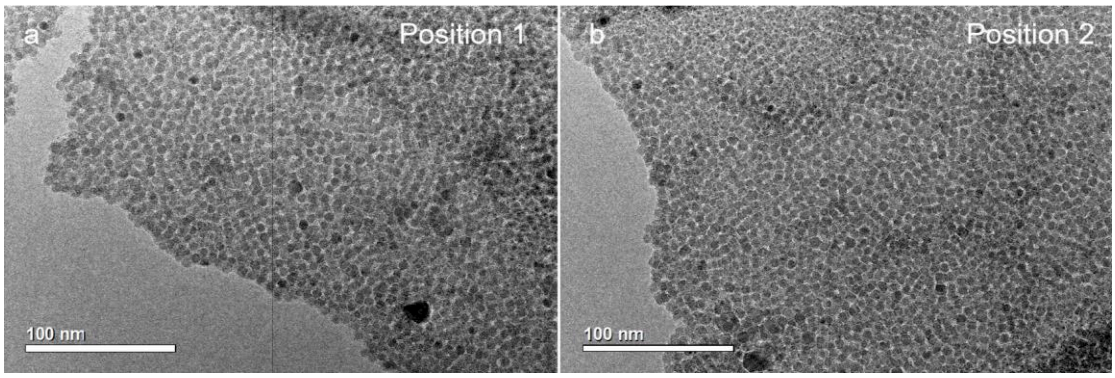

Fig. S9 | Morphology of $CuFe_2O_4$. HRTEM images of $CuFe_2O_4$ in **a,** position 1 and **b,** position 2.

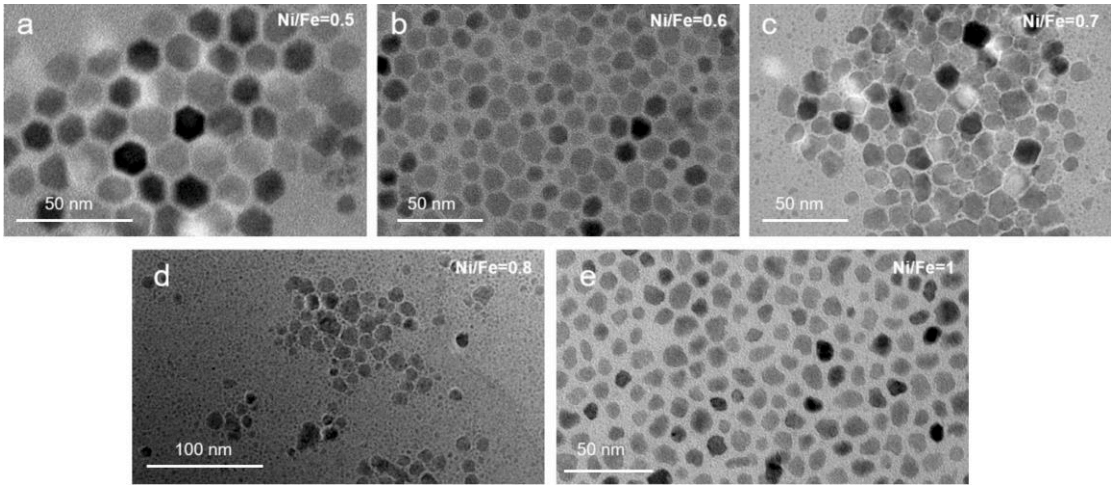

Fig. S10 | Morphology of $Ni_xFe_yO_4$. HRTEM images of $Ni_xFe_yO_4$ in **a,** x/y=0.5, **b,** x/y=0.6, **c,** x/y=0.7, **d,** x/y=0.8, **e,** x/y=1.

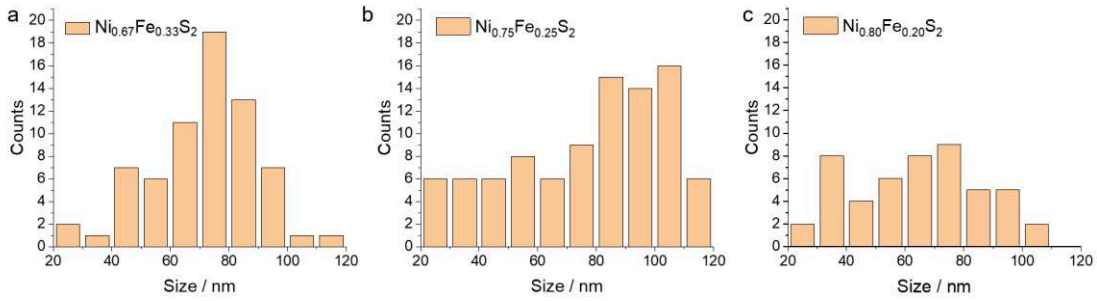

Fig. S11 | Particle size analysis $Ni_xFe_{1-x}S_2$. Size distribution of $Ni_xFe_{1-x}S_2$**: a,** $Ni_{0.67}Fe_{0.33}S_2$ (Maximum size = 112.11 nm, Minimum size = 25.05 nm, **Mean size = 71.30 nm**)**, b,** $Ni_{0.75}Fe_{0.25}S_2$ (Maximum size = 123.74 nm, Minimum size = 20.24 nm, **Mean size = 79.33 nm**)**, c,** $Ni_{0.80}Fe_{0.20}S_2$ (Maximum size = 100.88 nm, Minimum size = 14.78 nm, **Mean size = 63.65 nm**).

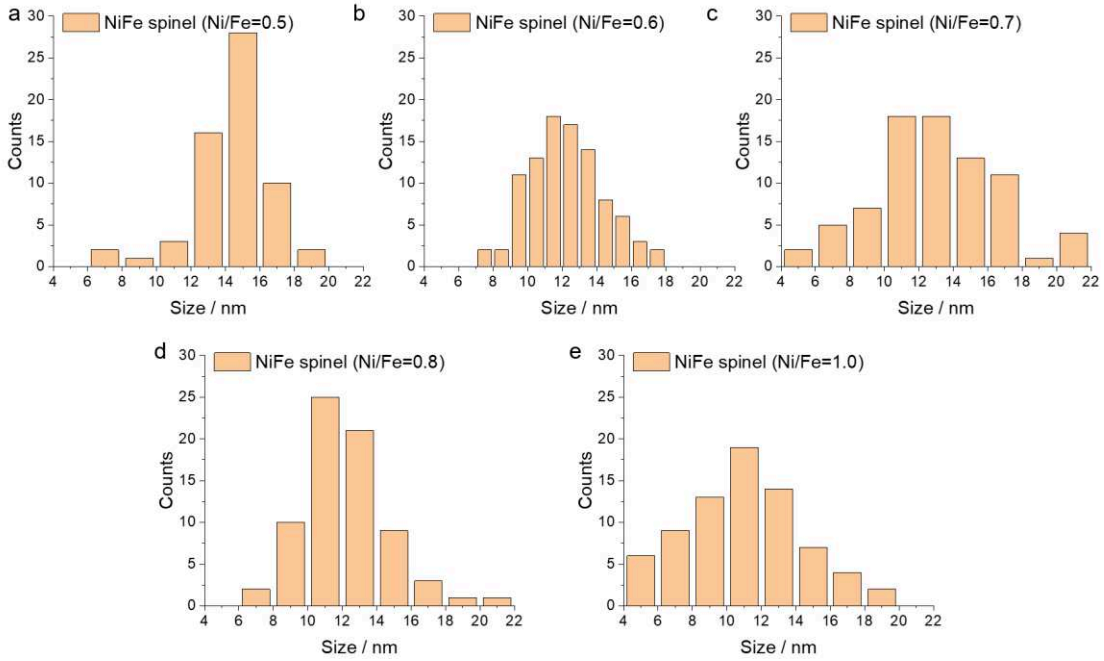

Fig. S12 | Particle size analysis NiFe spinel catalysts. The particle size distribution statistics for five NiFe spinel catalysts with different Ni/Fe ratios: **a,** Ni/Fe = 0.5: Maximum size = 18.41 nm, Minimum size = 7.10 nm, **Mean size = 14.53 nm**. **b,** Ni/Fe = 0.6: Maximum size = 17.92 nm, Minimum size = 7.80 nm, **Mean size = 12.29 nm**. **c,** Ni/Fe = 0.7: Maximum size = 20.52 nm, Minimum size = 4.97 nm, **Mean size = 12.97 nm**. **d,** Ni/Fe = 0.8: Maximum size = 24.15 nm, Minimum size = 7.24 nm, **Mean size = 12.12 nm**. **e,** Ni/Fe = 1.0: Maximum size = 18.28 nm, Minimum size = 4.82 nm, **Mean size = 11.04 nm**.

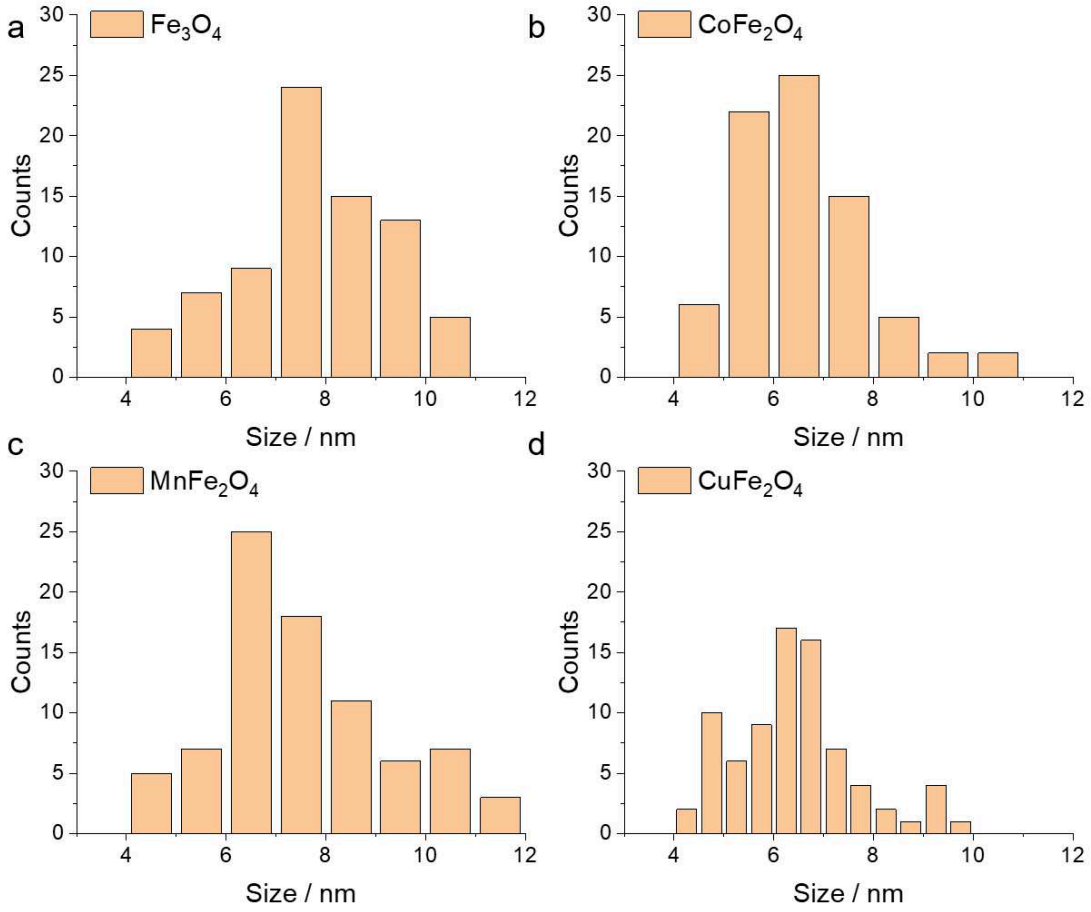

Fig. S13 | Particle size analysis of Fe_3O_4 and XFe_3O_4 (M = Co, Mn, Cu) catalysts. The particle size distribution statistics for

a, Fe_3O_4 (Maximum size = 10.97 nm, Minimum size = 4.01 nm, **Mean size = 7.78 nm**). **b,** $CoFe_3O_4$ (Maximum size = 10.21 nm, Minimum size = 4.50 nm, **Mean size = 6.45 nm**). **c,** $MnFe_3O_4$ (Maximum size = 11.60 nm, Minimum size = 4.23 nm, **Mean size = 7.48 nm**). **d,** $CuFe_3O_4$ (Maximum size = 9.38 nm, Minimum size = 4.20 nm, **Mean size = 6.33 nm**).

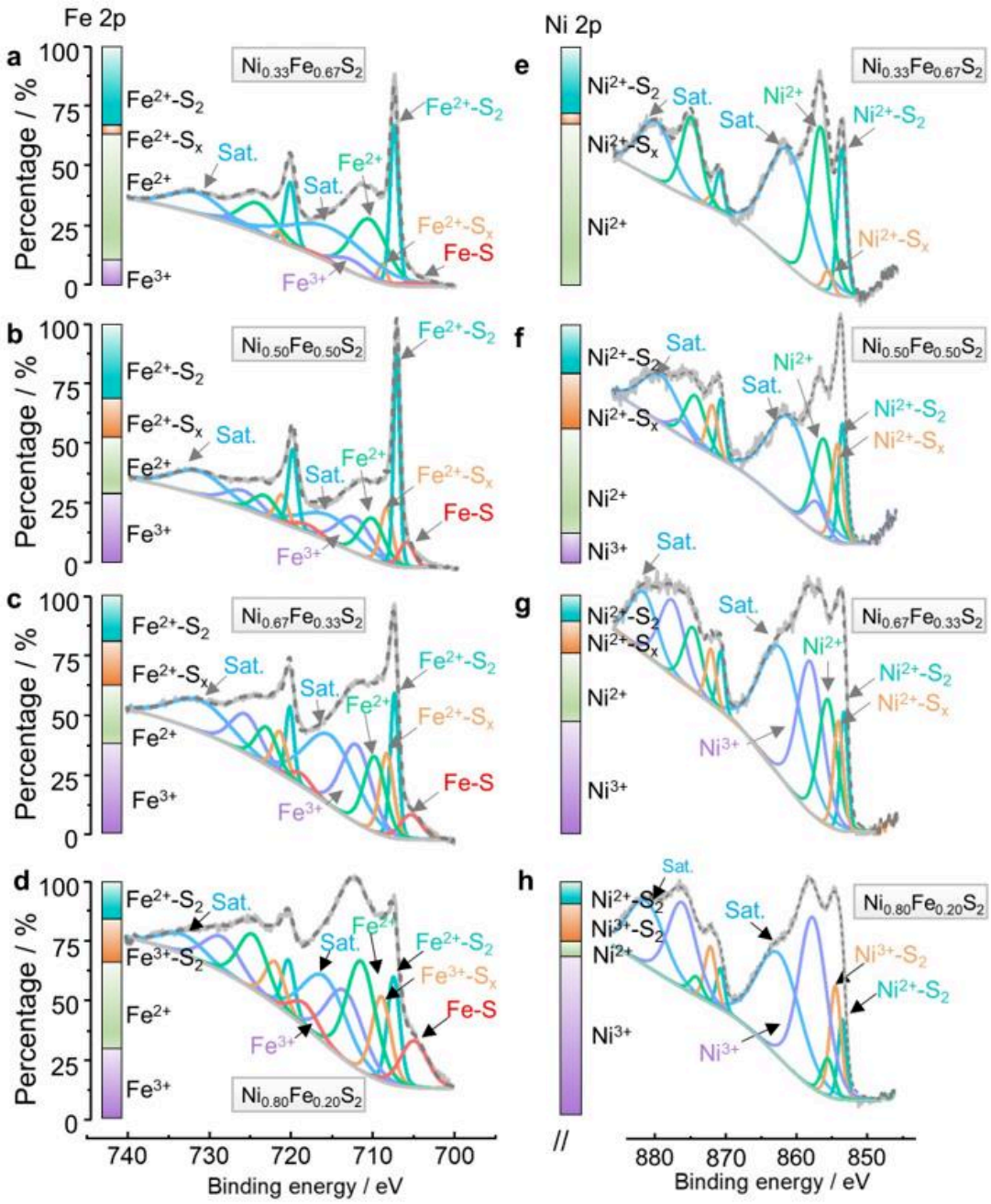

Fig. S14 | Analysis of surface chemical states for $Ni_xFe_{1-x}S_2$ (x=0.33, 0.50, 0.67, 0.80): Fe and Ni. High-resolution XPS spectra of $Ni_xFe_{1-x}S_2$ in **a-d,** Fe 2p, **e-h,** Ni 2p regions and corresponding percentage of chemical states.

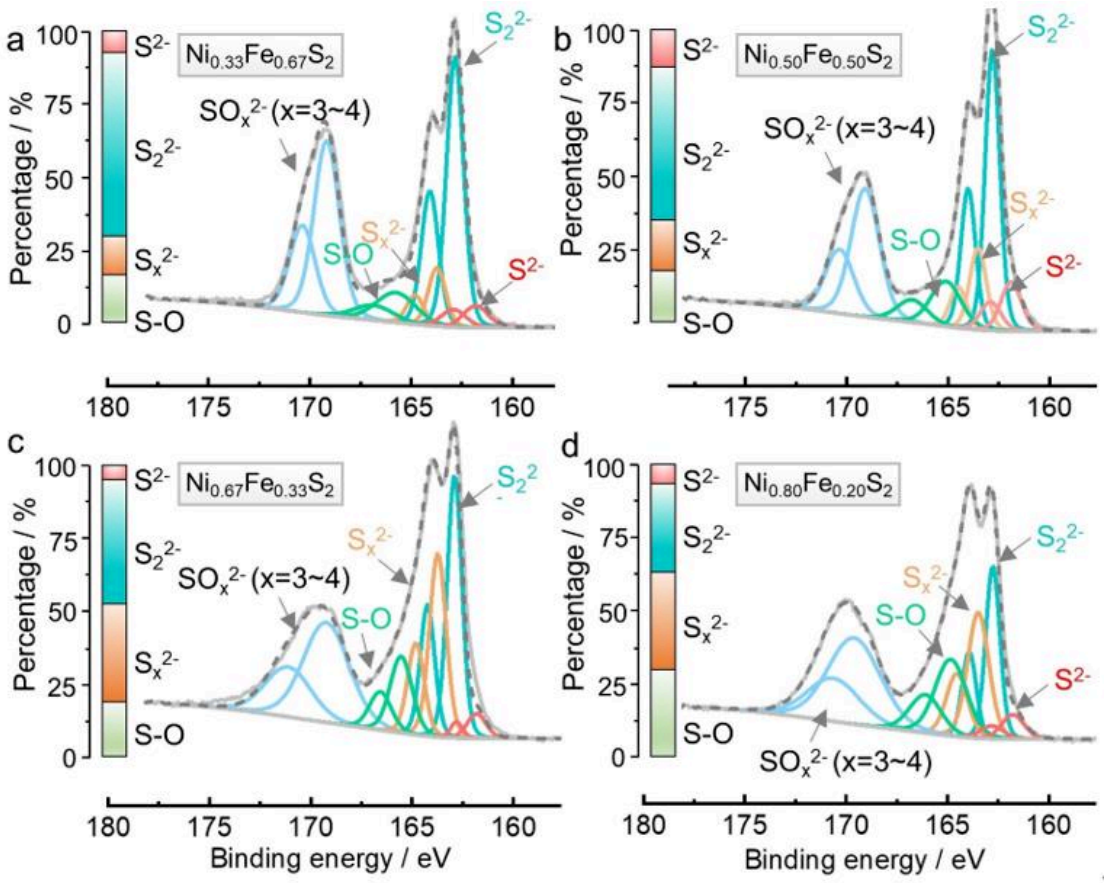

Fig. S15 | Analysis of surface chemical states for $Ni_xFe_{1-x}S_2$ (x=0.33, 0.50, 0.67, 0.80): S. High-resolution XPS spectra of $Ni_xFe_{1-x}S_2$ in S 2p: **a,** $Ni_{0.33}Fe_{0.67}S_2$, **b,** $Ni_{0.50}Fe_{0.50}S_2$ **c,** $Ni_{67}Fe_{0.33}S_2$, d, $Ni_{0.80}Fe_{0.20}S_2$ and corresponding percentage of chemical states.

Tab. S1 | XPS peak fitting for Ni, Fe, S 2p regions.[1-6]

Regions	i	ii	iii	iv	v
Fe 2p	Fe^{2+}-S	Fe^{2+}-S_2	Fe^{2+}-S_x	Fe^{2+}	Fe^{3+}
2p 3/2 (eV)	706.3	707.3	708.6	710.6	712.8
2p 1/2 (eV)	719.1	720.1	721.5	723.5	725.7
Ni 2p (eV)	Ni^{2+}-S_2	Ni^{2+}-S_x	Ni^{2+}	Ni^{3+}	-
2p 3/2 (eV)	853.5	854.4	856.2	857.5	-
2p 1/2 (eV)	870.6	871.6	873.8	875.8	-
S 2p	S^{2-}	S_2^{2-}	S_x^{2-}	S-O	SO_4^{2-}
2p 3/2 (eV)	161.7	162.8	163.7	165.7	169.2
2p 1/2 (eV)	162.9	164.0	164.8	166.9	170.4

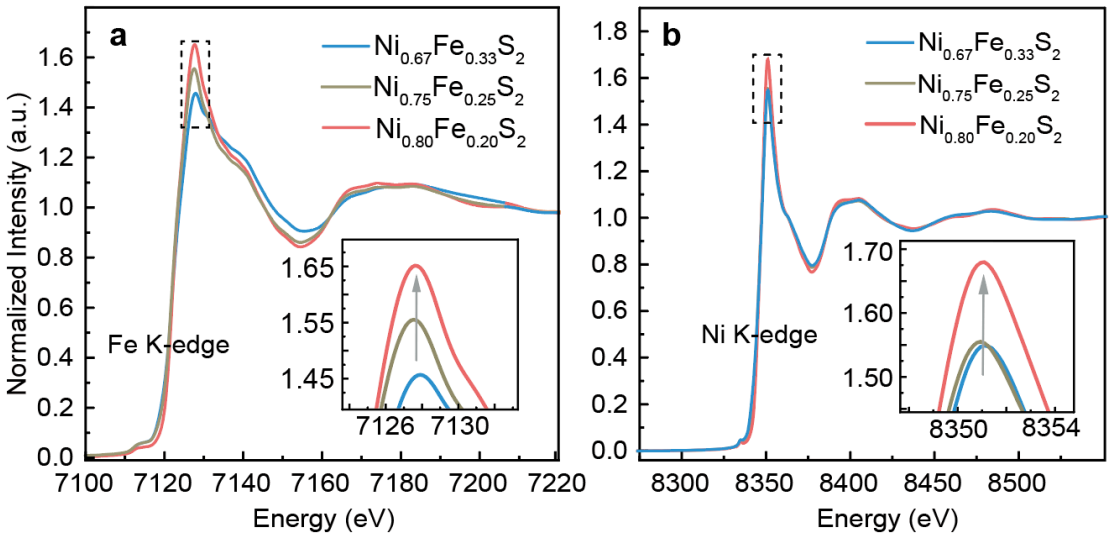

Fig. S16 | Electronic structure of $Ni_xFe_{1-x}S_2$. **a, b** XANES spectra at the Fe and Ni K-edges for $Ni_xFe_{1-x}S_2$ materials (x = 0.67, 0.75, 0.80) under ex-situ conditions. Insets show magnified white-line peak amplitudes.

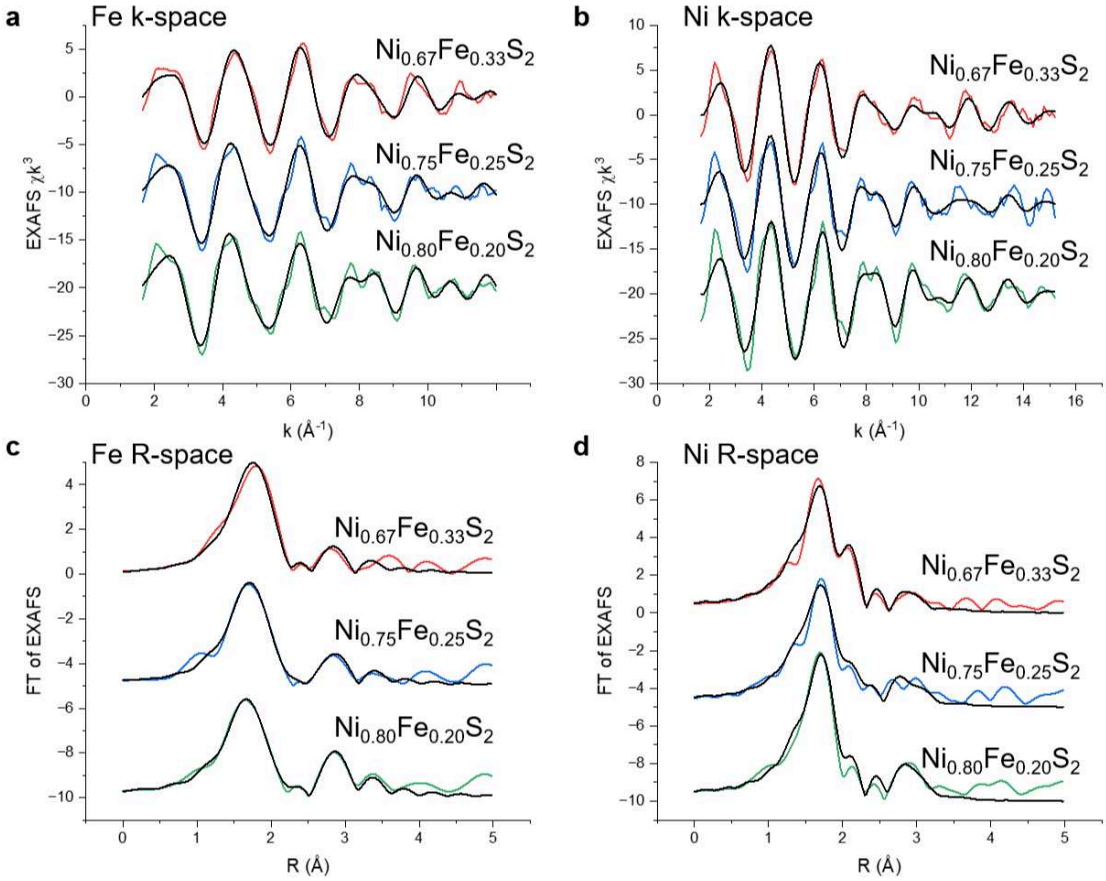

Fig. S17 | EXAFS analysis of $Ni_xFe_{1-x}S_2$ (x=0.67, 0.75, 0.80). Left panels: Fe spectra. Right panels: Ni spectra. Colored lines show experimental data and black lines show simulations. **a, b,** Fe/Ni k-space. **c, d,** Fe/Ni R-space.

The EXAFS spectra show similar shapes at the Fe and Ni K-edges, featuring a slight increase of the first Fourier transform (FT) peak due to metal-ligand bonds and an increasing second FT peak at ~2.80 Å due to metal-metal distance contributions for increasing Ni contents. EXAFS simulation analysis revealed similar Fe/Ni-O bond lengths (~2.05±0.20 Å) and metal-metal distances (in the range of ca. 2.75-3.40 Å) in the three sample types.

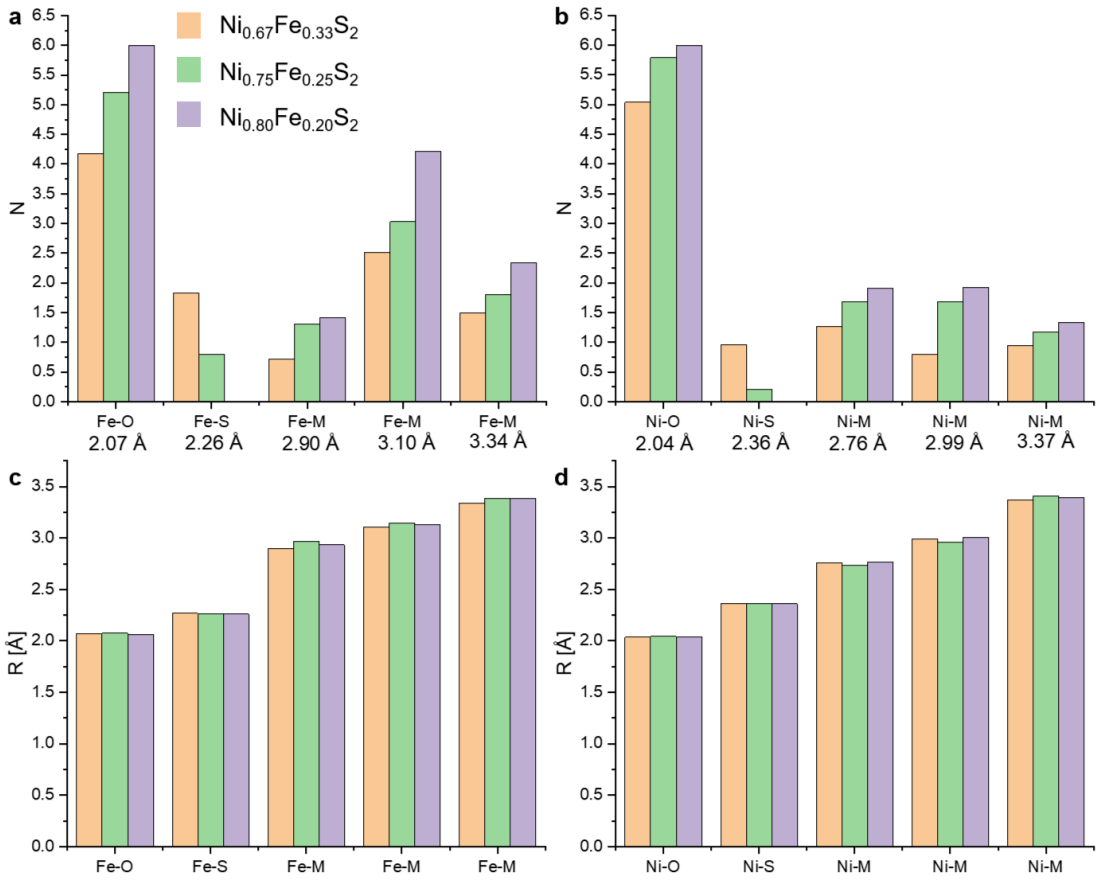

Fig. S18 | Summary of elemental coordination for $Ni_xFe_{1-x}S_2$. a, b, Coordination number of Fe and Ni K-edge for $Ni_xFe_{1-x}S_2$ (x=0.67, 0.75, 0.80) and **c, d,** coordination distance of Fe and Ni, respectively.

Tab. S2 | EXAFS simulation parameters for $Ni_xFe_{1-x}S_2$: Fe

	$Ni_{0.67}Fe_{0.33}S_2$			$Ni_{0.75}Fe_{0.25}S_2$			$Ni_{0.80}Fe_{0.20}S_2$		
	R [Å]	N	$2\sigma^2$	R [Å]	N	$2\sigma^2$	R [Å]	N	$2\sigma^2$
Fe-O	2.07	4.17	0.022	2.07	5.21	0.022	2.06	6.00	0.024
Fe-S	2.27	1.83	0.022	2.27	0.79	0.022	2.27	0	0.024
Fe-M	2.90	0.72	0.020	2.97	1.31	0.020	2.93	1.41	0.020
Fe-M	3.10	2.51	0.020	3.15	3.03	0.020	3.13	4.22	0.020
Fe-M	3.34	1.49	0.020	3.39	1.80	0.020	3.38	2.34	0.020

Tab. S3 | EXAFS simulation parameters for $Ni_xFe_{1-x}S_2$: Ni

	$Ni_{0.67}Fe_{0.33}S_2$			$Ni_{0.75}Fe_{0.25}S_2$			$Ni_{0.80}Fe_{0.20}S_2$		
	R [Å]	N	$2\sigma^2$	R [Å]	N	$2\sigma^2$	R [Å]	N	$2\sigma^2$
Ni-O	2.04	5.04	0.013	2.05	5.79	0.016	2.04	6.00	0.013
Ni-S	2.36	0.96	0.013	2.36	0.21	0.016	2.36	0	0.013
Ni-M	2.76	1.26	0.020	2.73	1.68	0.020	2.77	1.91	0.020
Ni-M	2.99	0.80	0.020	2.96	1.68	0.020	3.00	1.92	0.020
Ni-M	3.37	0.94	0.020	3.41	1.17	0.020	3.40	1.33	0.020

Part 2: DFT prediction of catalyst activation

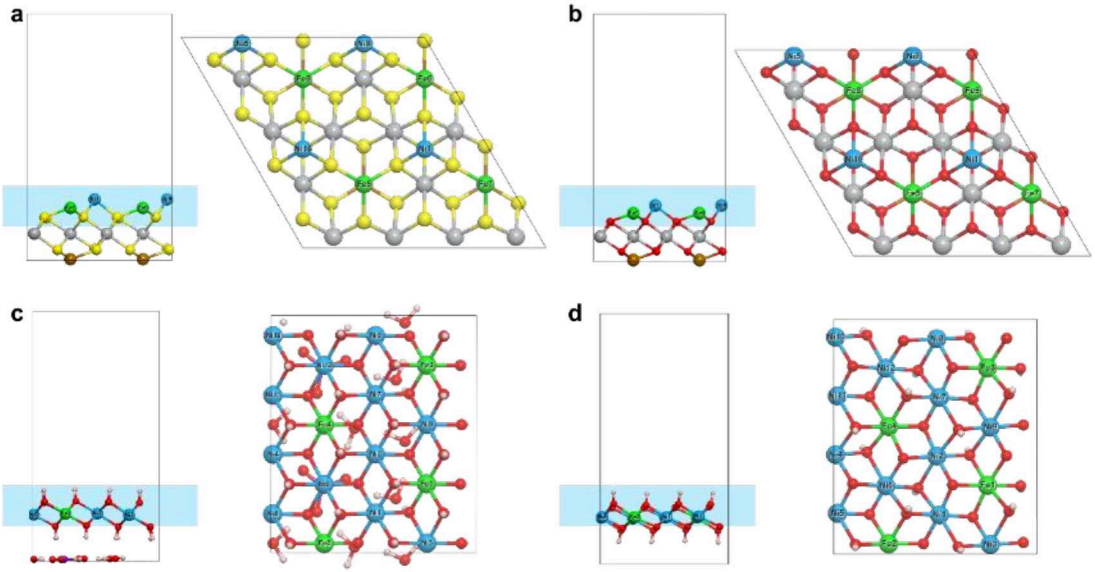

Fig. S19 | Slab models used for DFT calculation. a, side (left) and top (right) view of the (2×2) $NiFe_2$ sulfide (111), which contains totally 56 atoms (24 Ni + Fe and 32 S atoms). **b,** side (left) and top (right) view of (2×2) $NiFe_2$ oxide (111), which contains totally 56 atoms (24 Ni and Fe and 32 O atoms). **c,** side (left) and top (right) view of (1×2) Ni_3Fe LDH (001), which contains totally 112 atoms (16 Ni+Fe, 46 O, 48 H and 2 C atoms). **d,** side (left) and top (right) view of (1×2) Ni_3FeOOH (001), which contains totally 64 atoms (16 Ni+Fe, 32 O and 16 H atoms). The grey, brown, yellow, red, purple and white balls represent Ni, Fe, S, O, C and H atoms, respectively. Especially, the Ni and Fe atoms in the top layer (blue areas in the side views) have highlighted by blue and green balls, respectively.

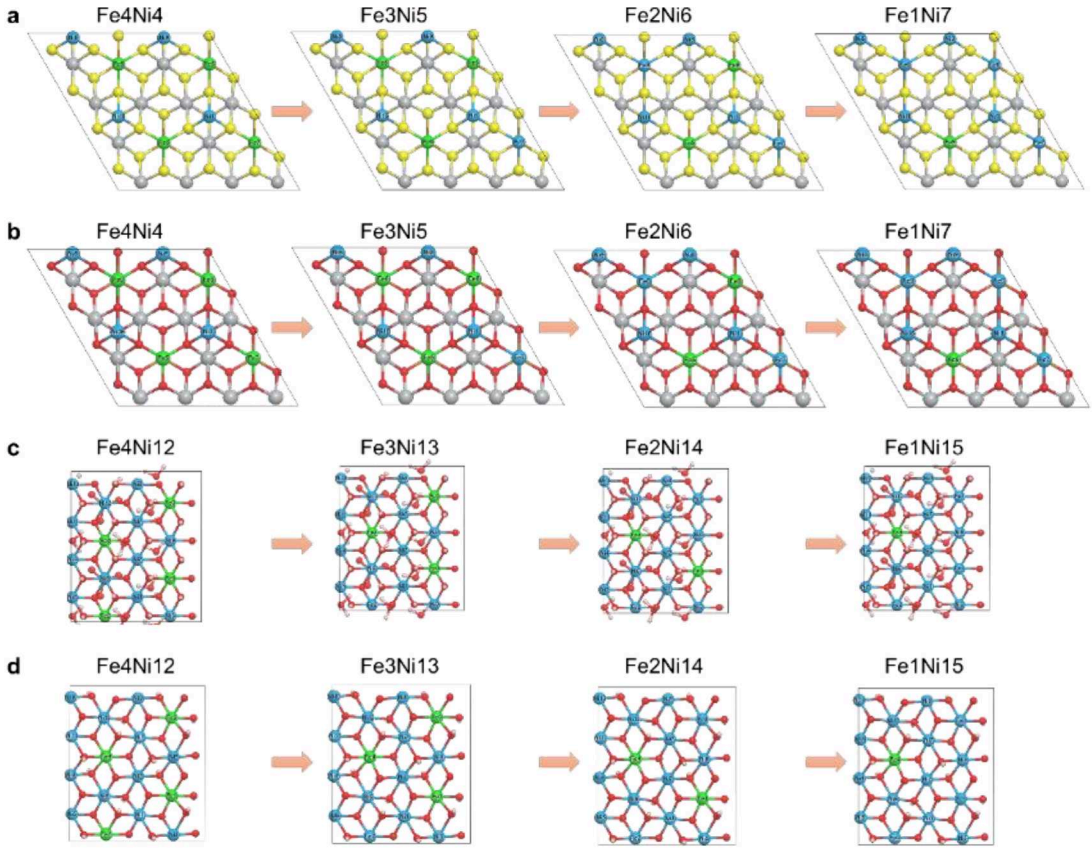

Fig. S20 | Schematic structure illustrates the creation of different Fe concentrations in the slab models. a, top view of (2×2) $NiFe_2$ sulfide (111) with different surface Fe concentrations from Fe_4Ni_4 to Fe_1Ni_7. **b,** top view of (2×2) $NiFe_2$ oxide (111) with different surface Fe concentrations from Fe_4Ni_4 to Fe_1Ni_7. **c,** top view of (1×2) Ni_3Fe LDH (001) with different surface Fe concentrations from Fe_4Ni_{12} to Fe_1Ni_{15}. **d,** top view of (1×2) Ni_3FeOOH (001) with different surface Fe concentrations from Fe_4Ni_{12} to Fe_1Ni_{15}.

The slab models of $NiFe_2$ sulfide (111), $NiFe_2$ oxide (111), Ni_3Fe LDH (001) and Ni_3FeOOH (001) were constructed, containing totally 8, 8, 16 and 16 Ni+Fe atoms in the top layer, respectively (**Suppl. Fig. 19**). Then, surface Ni atoms were gradually substituted with Fe to model the structures with different Fe concentrations, i.e., Fe_4Ni_4, Fe_3Ni_5, Fe_2Ni_6, Fe_1Ni_7 in $NiFe_2$ sulfide (111) and $NiFe_2$ oxide (111), and Fe_4Ni_{12}, Fe_3Ni_{13}, Fe_2Ni_{14}, Fe_1Ni_{15} in Ni_3Fe LDH (001) and Ni_3FeOOH (001) (**Suppl. Fig. 20**).

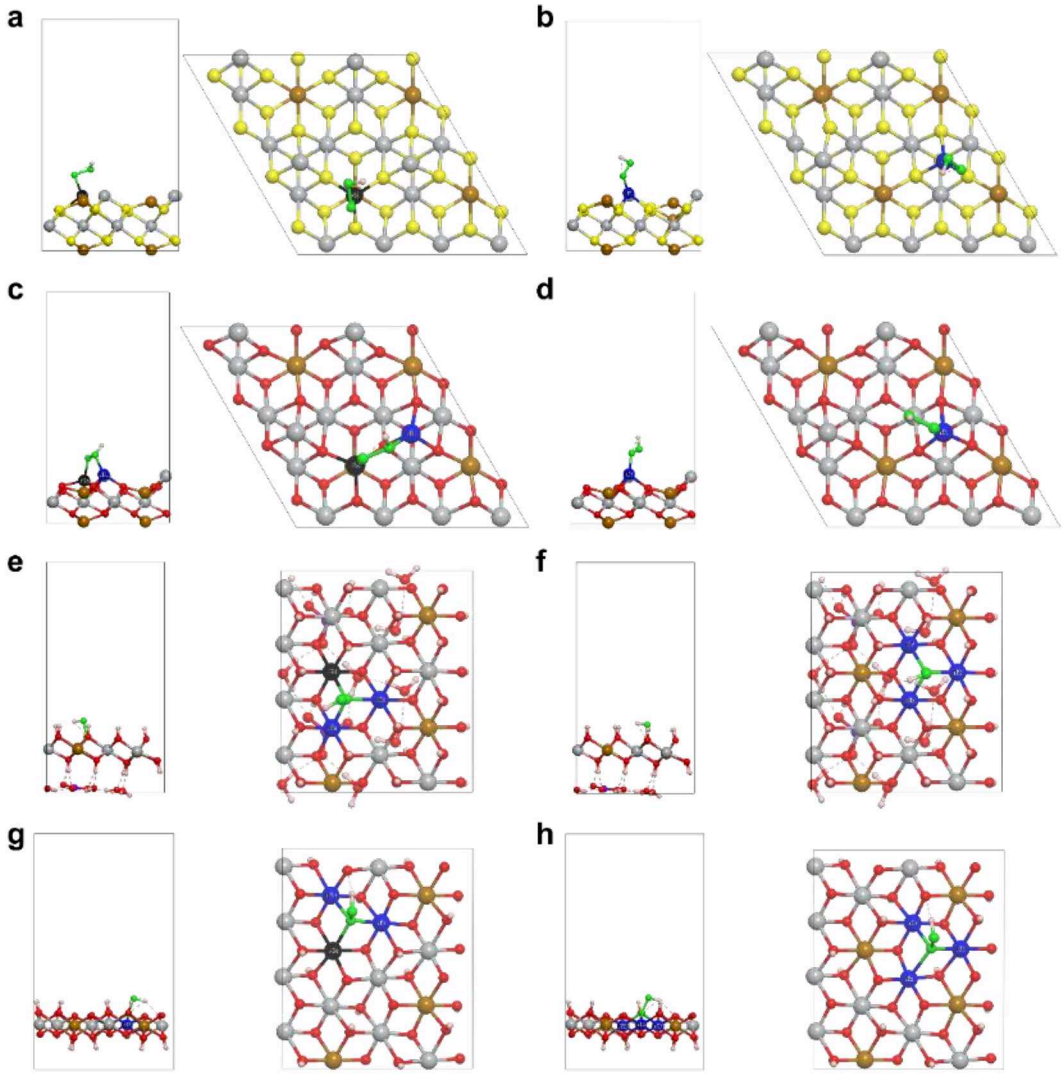

Fig. S21 | Side (left) and top (right) view of *OOH adsorption configurations at Fe and Ni sites on different surfaces. a, b, $NiFe_2$ sulfide (111), **c, d**, $NiFe_2$ oxide (111), **e, f**, Ni_3Fe LDH (001) and **g, h**, Ni_3FeOOH (001). The grey, brown, yellow, red, purple and white balls represent Ni, Fe, S, O, C and H atoms, respectively. Especially, the Ni and Fe atoms bonded with *OOH are highlighted by blue and black balls, while the O atom in *OOH is highlighted by green blue.

It is noteworthy that the adsorption configuration of *OOH depends on the material types (**Suppl. Fig. 21**). For $FeNi_2$ sulfide (111), *OOH was adsorbed at the Fe or Ni site via a single bond, while for Ni_3Fe LDH (001) and Ni_3FeOOH (001), *OOH bonds to three surface metal atoms. Therefore, the relatively simple weighted d-band center model was used to rationalize the adsorption strengths on Ni_3Fe LDH (001) and Ni_3FeOOH (001).[7]

$$\varepsilon_d = \frac{\sum_M V_M^2 E_d^M N^M}{\sum_M V_M^2 N^M}$$

where V_M^2 represents the d-band coupling matrix element for the surface metal atom M.[8] Specifically, V_{Fe}^2 and V_{Ni}^2 are 1.59 and 1.16, respectively. E_d^M is the d-band center of surface

metal atom M. N^M is the number of bonds between surface metal atom M and *OOH species. The calculated d band centers on Fe_2Ni sulfide and Fe_2Ni oxide for Ni and Fe sites are shown in **Suppl. Fig. 22a, b**, respectively, while the weighted d band centers on Ni_3Fe LDH and Ni_3FeOOH for Ni and Fe sites are shown in **Suppl. Fig. 22c, d**, respectively.

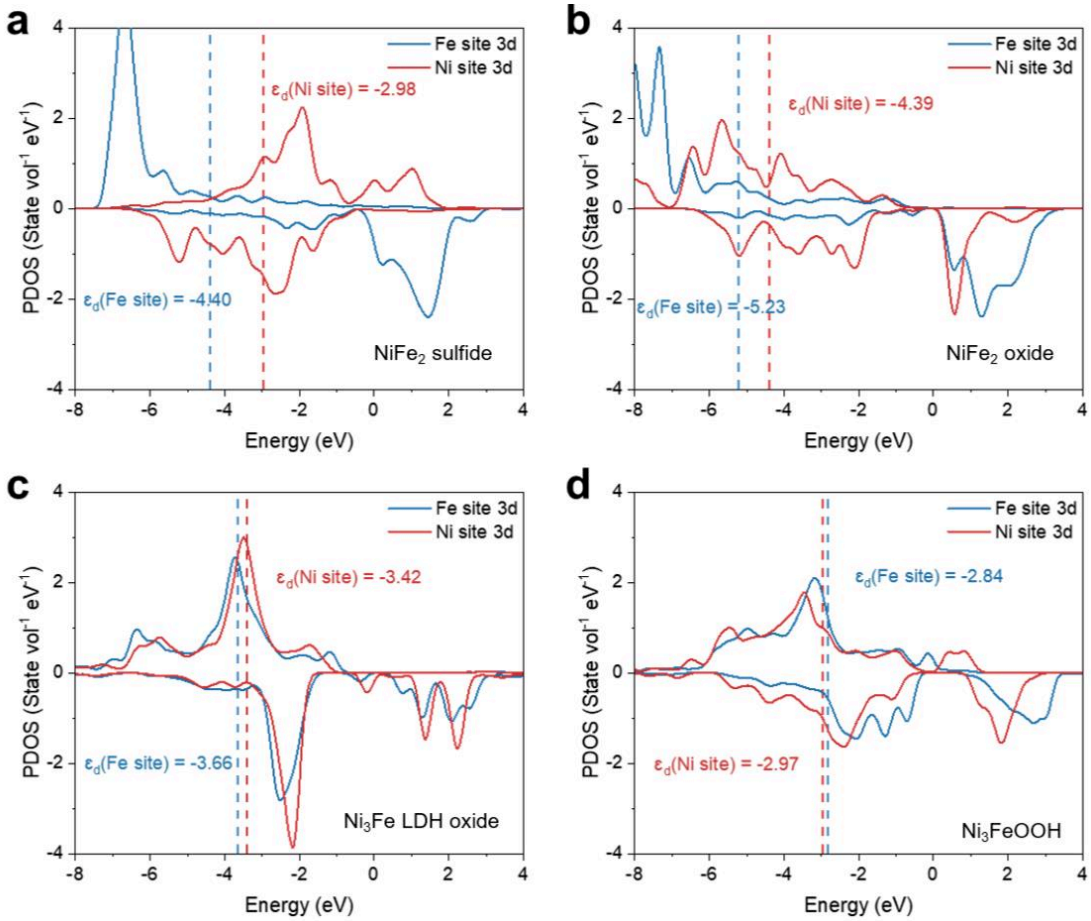

Fig. S22 | The d-band centers illustrate the difference of *OOH adsorption energy. The projected density of states (PDOS) of 3d states for Fe and Ni sites in **a,** $NiFe_2$ sulfide (111), **b,** $NiFe_2$ oxide (111), **c,** Ni_3Fe LDH (001) and **d,** Ni_3FeOOH (001). The d-band center (ε_d) of Fe and Ni sites is marked by blue and red dashed lines, respectively.

Part 3: Activation of the anodes by CV

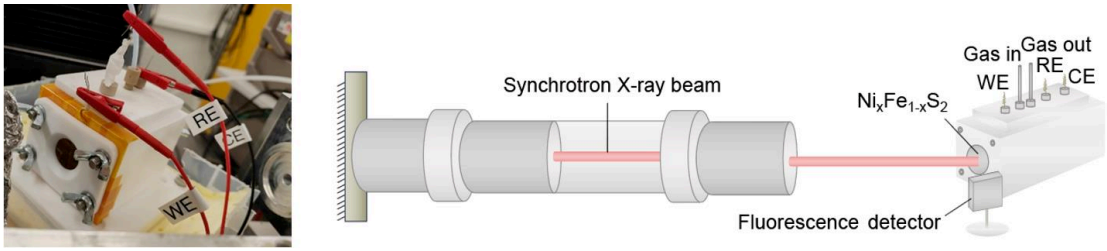

Fig. S23 | Photo and illustration of the cell for operando XANES cell. A three-electrode electrolytic cell is used in operando XANES experiments for electrochemical investigations, allowing for controlled electrochemical reactions while analyzing samples in the X-ray beam.

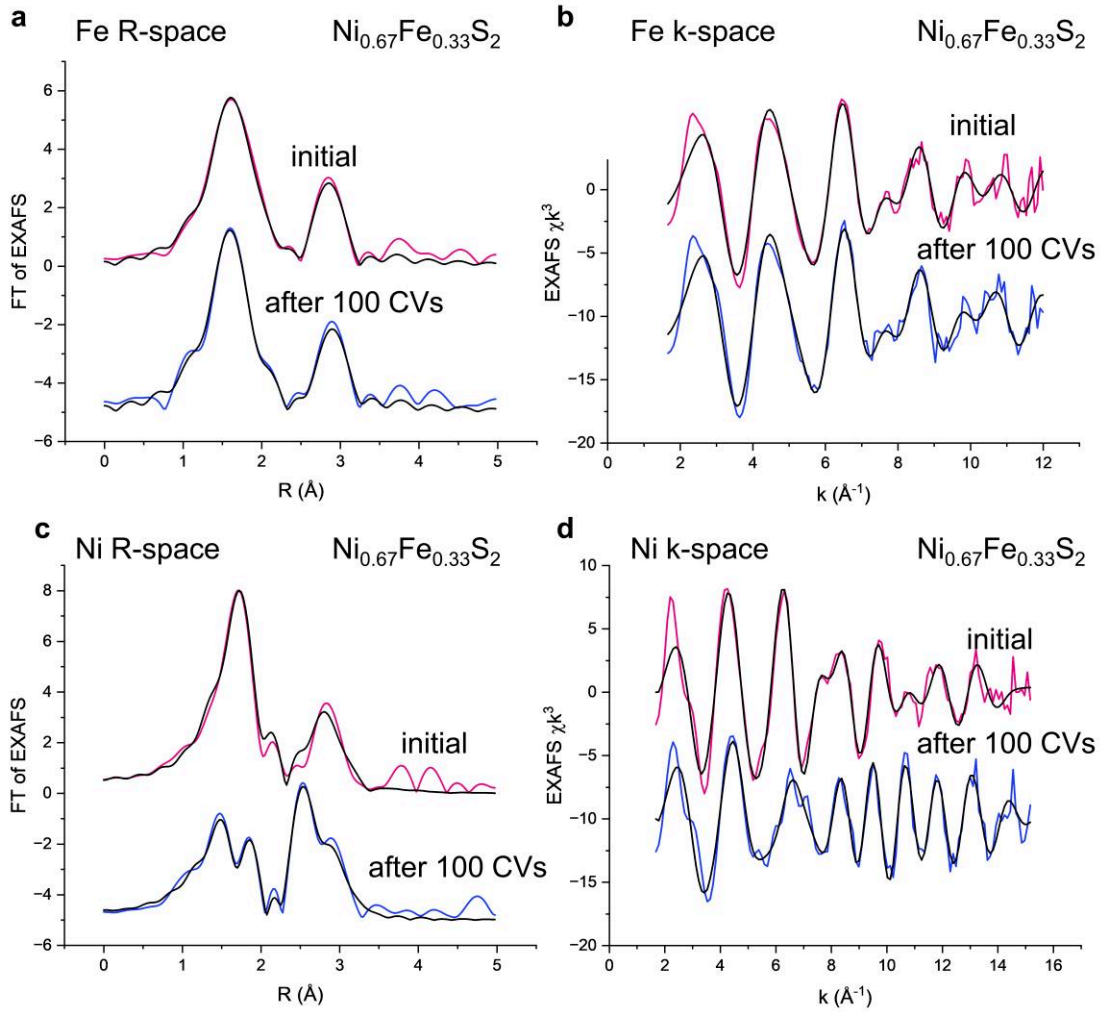

Fig. S24 | EXAFS analysis of $Ni_{0.67}Fe_{0.33}S_2$. a, b, Fe and **c, d,** Ni EXAFS spectra before and after CV activation. Colored lines, experimental data; black lines, simulations. 100 CVs cycles were done in a 1.0-1.7 V range at 100 $mV \cdot s^{-1}$.

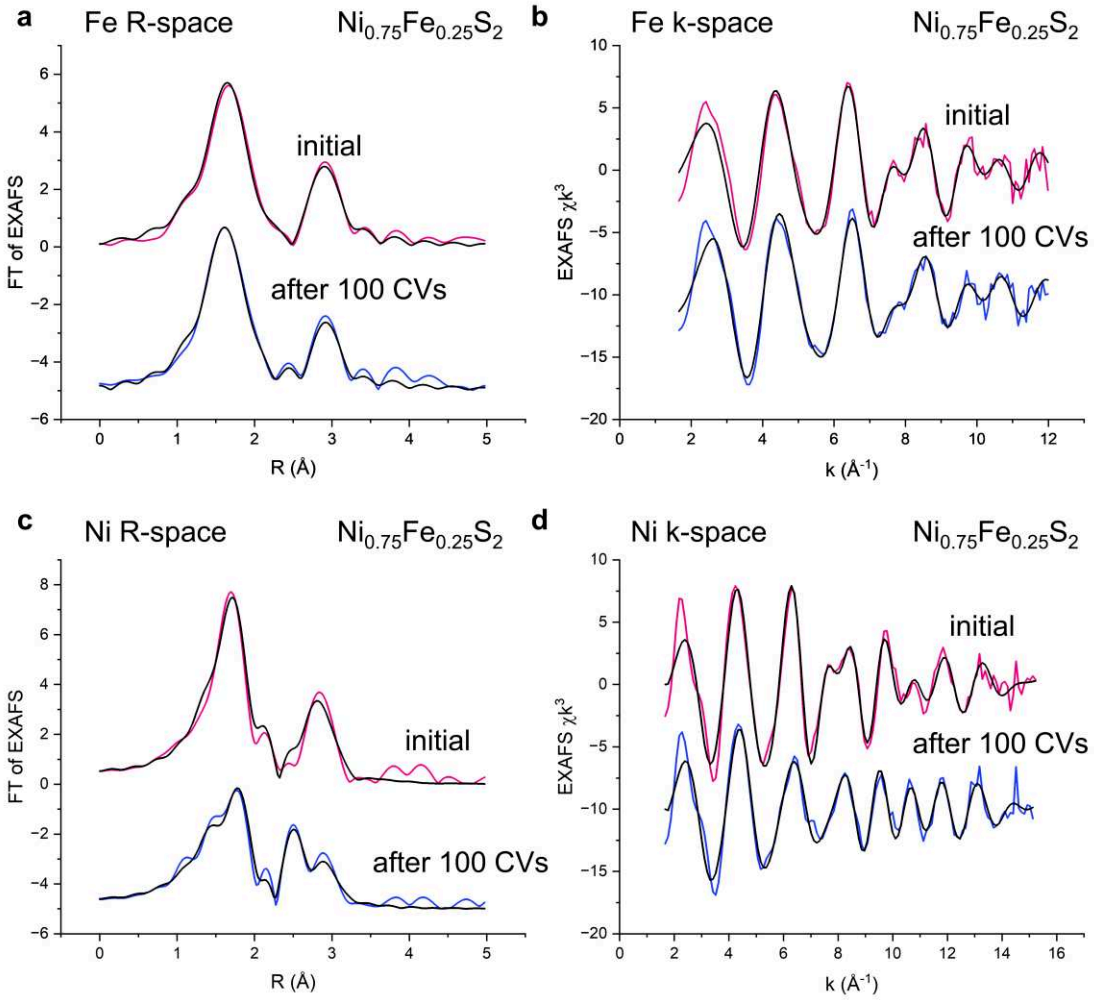

Fig. S25 | EXAFS analysis of $Ni_{0.75}Fe_{0.25}S_2$. a, b, Fe and **c, d,** Ni EXAFS spectra before and after CV activation. Colored lines, experimental data; black lines, simulations. 100 CVs cycles were done in a 1.0-1.7 V range at 100 $mV \cdot s^{-1}$.

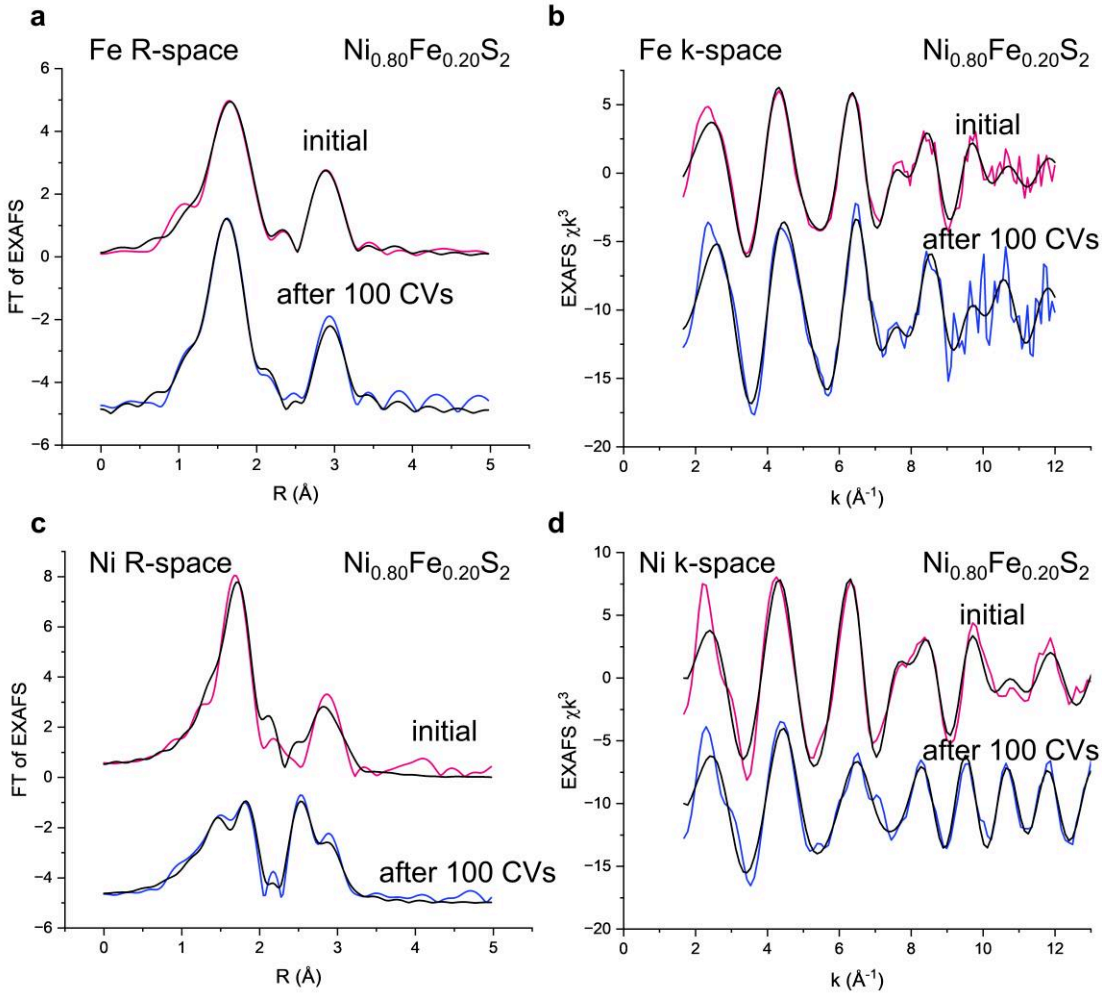

Fig. S26 | EXAFS analysis of $Ni_{0.80}Fe_{0.20}S_2$. a, b, Fe and **c, d,** Ni EXAFS spectra before and after CV activation. Colored lines, experimental data; black lines, simulations. 100 CVs cycles were done in a 1.0-1.7 V range at 100 $mV \cdot s^{-1}$.

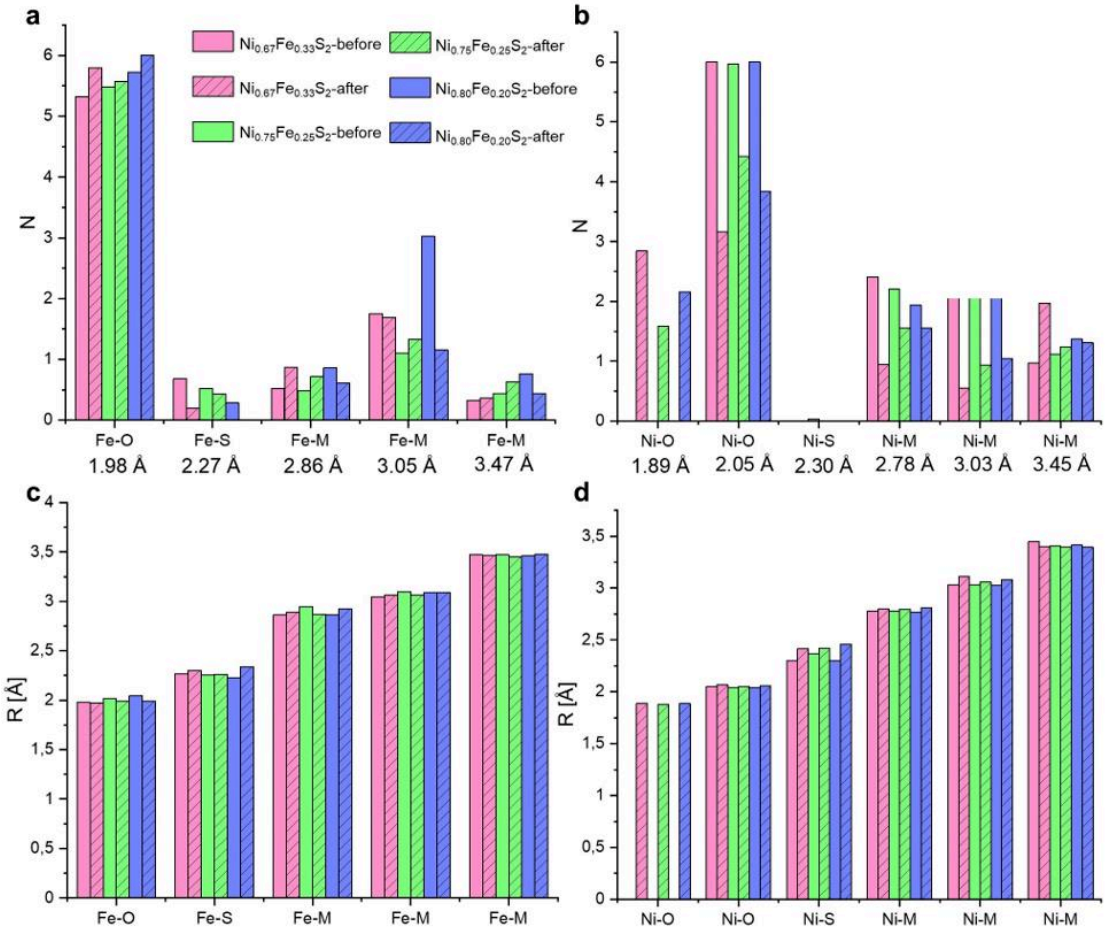

Fig. S27 | EXAFS simulation parameters (N and R) before and after CV activation of $Ni_xFe_{1-x}S_2$ (x=0.67, 0.75, 0.80). a, b, coordination numbers, N. **c, d,** interatomic distances, R.

Tab. S4 | EXAFS simulation parameters for $Ni_xFe_{1-x}S_2$ before and after CV activation: Fe.

	$Ni_{0.67}Fe_{0.33}S_2$ before CV			$Ni_{0.67}Fe_{0.33}S_2$ after CV		
	R [Å]	N	$2\sigma^2$	R [Å]	N	$2\sigma^2$
Fe-O	1.98	5.32	0.018	1.98	5.80	0.018
Fe-S	2.27	0.68	0.018	2.30	0.20	0.018
Fe-M	2.86	0.52	0.009	2.89	0.87	0.007
Fe-M	3.05	1.75	0.009	3.06	1.69	0.007
Fe-M	3.47	0.33	0.009	3.47	0.37	0.007

	$Ni_{0.75}Fe_{0.25}S_2$ before CV			$Ni_{0.75}Fe_{0.25}S_2$ after CV		
	R [Å]	N	$2\sigma^2$	R [Å]	N	$2\sigma^2$
Fe-O	2.02	5.48	0.019	1.99	5.57	0.020
Fe-S	2.26	0.52	0.019	2.26	0.43	0.020
Fe-M	2.95	0.49	0.003	2.87	0.72	0.009
Fe-M	3.10	1.10	0.003	3.06	1.33	0.009
Fe-M	3.47	0.44	0.003	3.45	0.63	0.009

	$Ni_{0.80}Fe_{0.20}S_2$ before CV			$Ni_{0.80}Fe_{0.20}S_2$ after CV		
	R [Å]	N	$2\sigma^2$	R [Å]	N	$2\sigma^2$
Fe-O	2.04	5.72	0.022	1.99	6.00	0.018
Fe-S	2.23	0.28	0.022	2.34	0	0.018
Fe-M	2.86	0.86	0.019	2.92	0.61	0.003
Fe-M	3.09	3.03	0.019	3.09	1.16	0.003
Fe-M	3.46	0.77	0.019	3.48	0.44	0.003

Tab. S5 | EXAFS simulation parameters for $Ni_xFe_{1-x}S_2$ before and after CV activation: Ni.

	$Ni_{0.67}Fe_{0.33}S_2$ before CV				$Ni_{0.67}Fe_{0.33}S_2$ after CV		
	R [Å]	N	$2\sigma^2$		R [Å]	N	$2\sigma^2$
Ni-O	2.05	6.00	0.012	Ni-O	1.89	2.84	0.013
Ni-S	2.30	0	0.012	Ni-O	2.07	3.16	0.013
Ni-M	2.78	2.41	0.020	Ni-M	2.80	0.95	0.003
Ni-M	3.03	3.76	0.020	Ni-M	3.11	0.55	0.003
Ni-M	3.45	0.97	0.020	Ni-M	3.40	1.97	0.003

	$Ni_{0.75}Fe_{0.25}S_2$ before CV				$Ni_{0.75}Fe_{0.25}S_2$ after CV		
	R [Å]	N	$2\sigma^2$		R [Å]	N	$2\sigma^2$
Ni-O	2.04	5.97	0.013	Ni-O	1.88	1.58	0.013
Ni-S	2.37	0.03	0.013	Ni-O	2.05	4.42	0.013
Ni-M	2.78	2.20	0.020	Ni-M	2.80	1.56	0.012
Ni-M	3.03	3.76	0.020	Ni-M	3.06	0.94	0.012
Ni-M	3.41	1.12	0.020	Ni-M	3.40	1.24	0.020

	$Ni_{0.80}Fe_{0.20}S_2$ before CV				$Ni_{0.80}Fe_{0.20}S_2$ after CV		
	R [Å]	N	$2\sigma^2$		R [Å]	N	$2\sigma^2$
Ni-O	2.04	5.97	0.013	Ni-O	1.88	1.58	0.013
Ni-S	2.37	0.03	0.013	Ni-O	2.05	4.42	0.013
Ni-M	2.78	2.20	0.020	Ni-M	2.80	1.56	0.012
Ni-M	3.03	3.76	0.020	Ni-M	3.06	0.94	0.012
Ni-M	3.41	1.12	0.020	Ni-M	3.40	1.24	0.020

Part 3: Activation of the anodes by CP

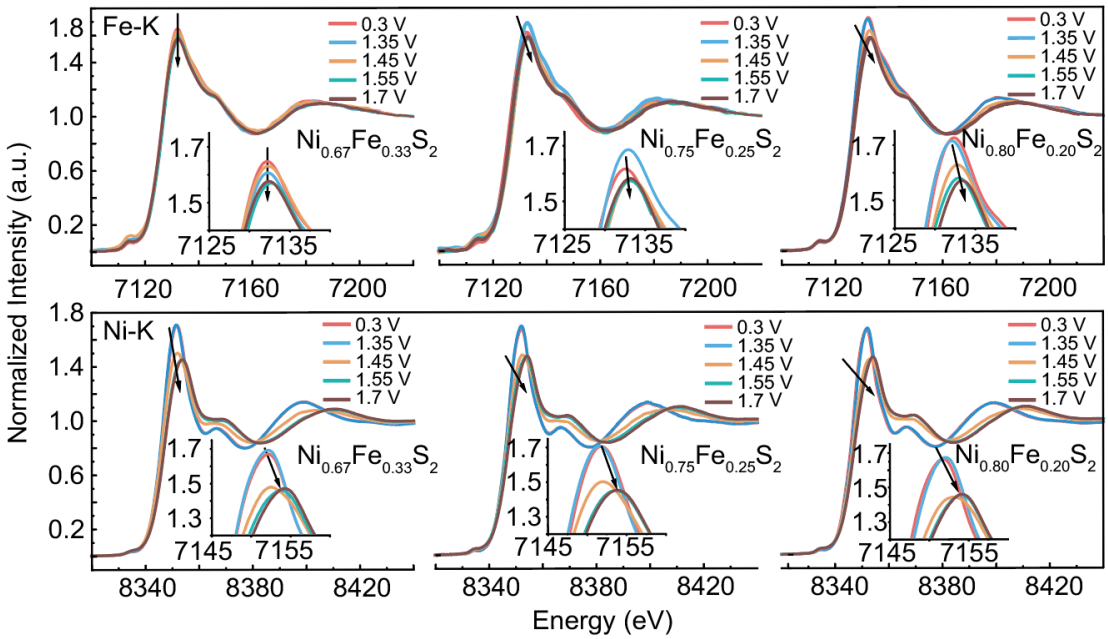

Fig. S28 | Operando XANES spectra at varying potentials for $Ni_xFe_{1-x}S_2$ (x=0.67, 0.75, 0.80). CP at OCP, 1.35, 1.45, 1.55 and 1.7 V at the Fe and Ni K-edges, respectively.

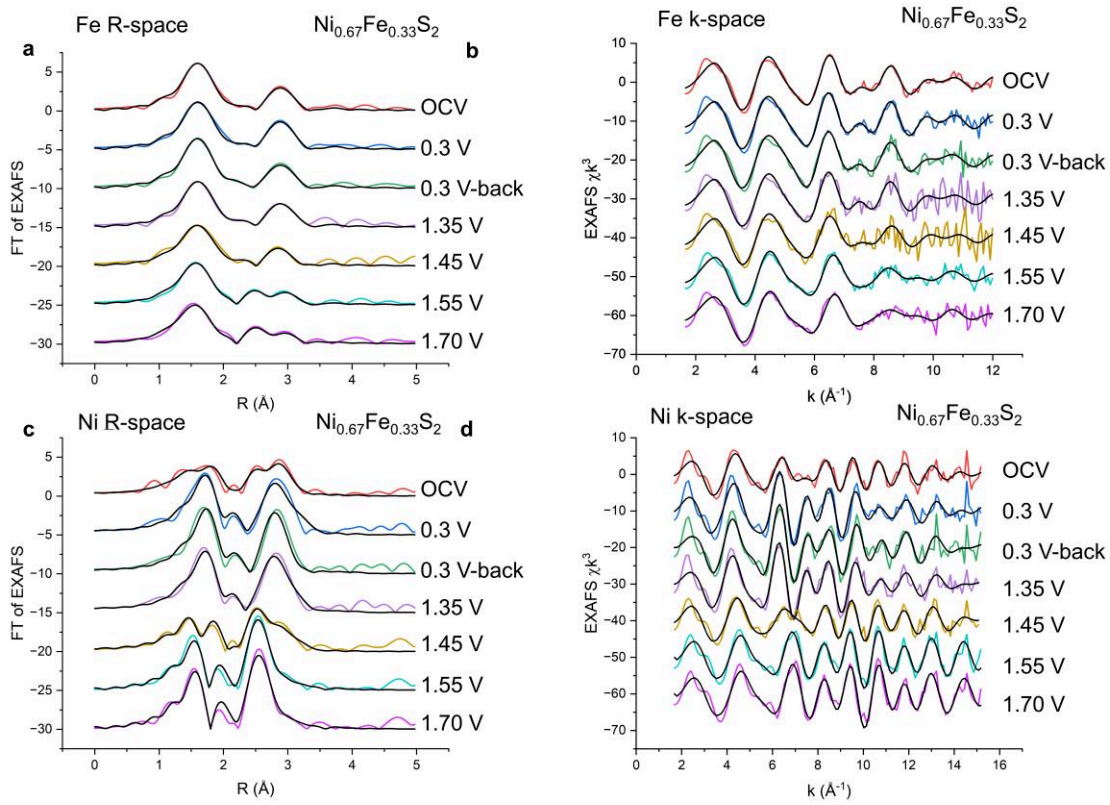

Fig. S29 | Operando EXAFS spectra at varying potentials for $Ni_{0.67}Fe_{0.33}S_2$. a, b, Fe K-edge. **c, d,** Ni K-edge. Spectra were collected at the indicated electrochemical potentials under operando-XAS conditions (back =respective potential revisited after application of 1.7 V). Colored lines, experimental data: black lines, simulations. Spectra are vertically stacked for clarity.

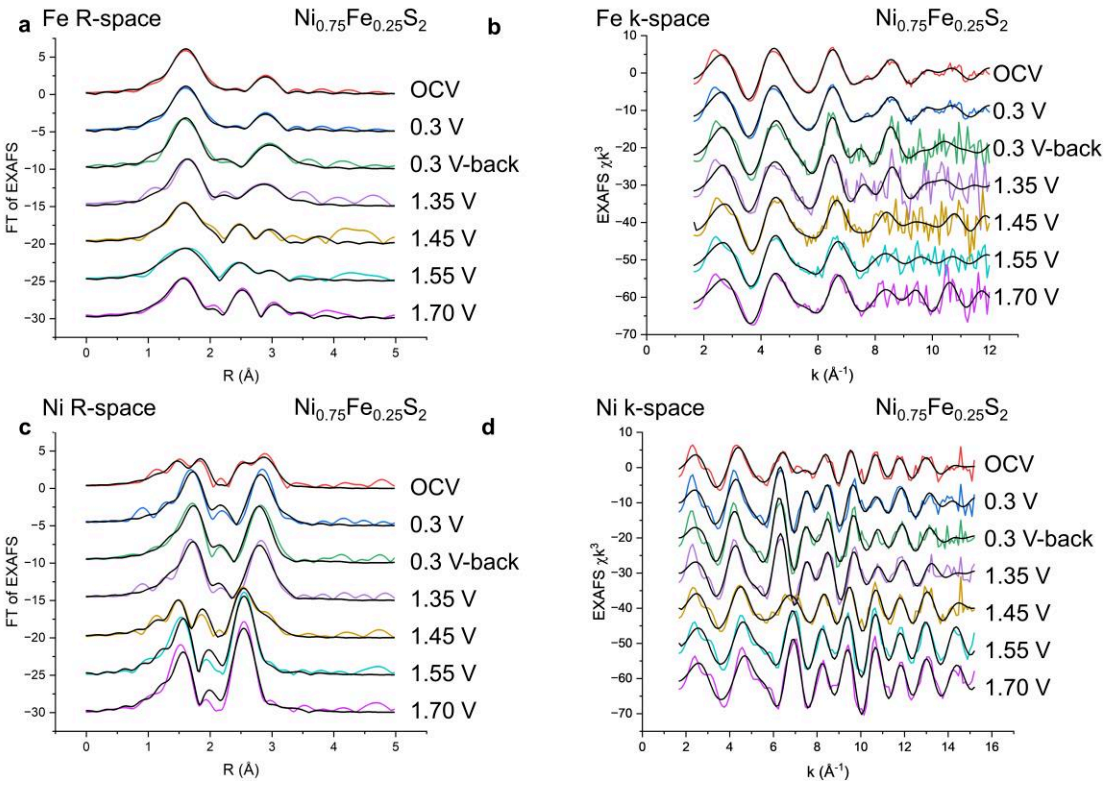

Fig. S30 | EXAFS spectra at varying potentials for $Ni_{0.75}Fe_{0.25}S_2$. a, b, Fe K-edge. **c, d,** Ni K-edge. Spectra were collected at the indicated electrochemical potentials under operando-XAS conditions (back =respective potential revisited after application of 1.7 V). Colored lines, experimental data: black lines, simulations. Spectra are vertically stacked for clarity.

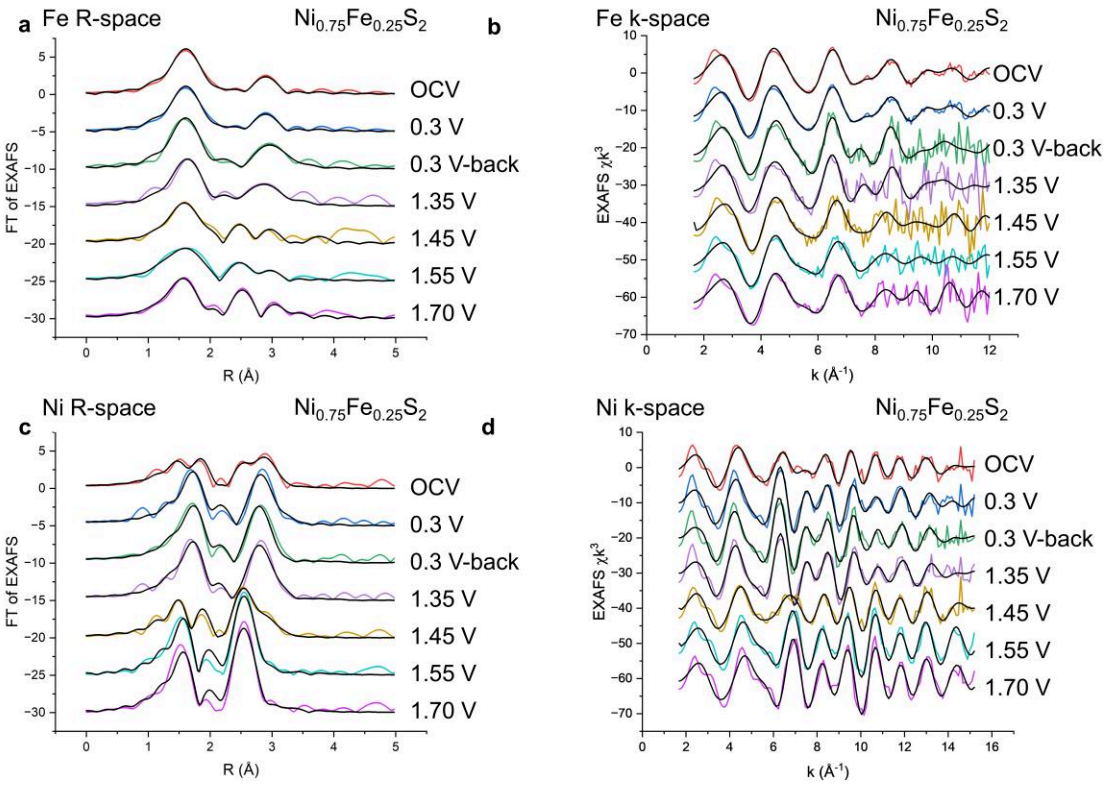

Fig. S31 | EXAFS spectra at varying potentials for $Ni_{0.80}Fe_{0.20}S_2$. a, b, Fe K-edge. **c, d,** Ni K-edge. Spectra were collected at the indicated electrochemical potentials under operando-XAS conditions (back =respective potential revisited after application of 1.7 V). Colored lines, experimental data: black lines, simulations. Spectra are vertically stacked for clarity.

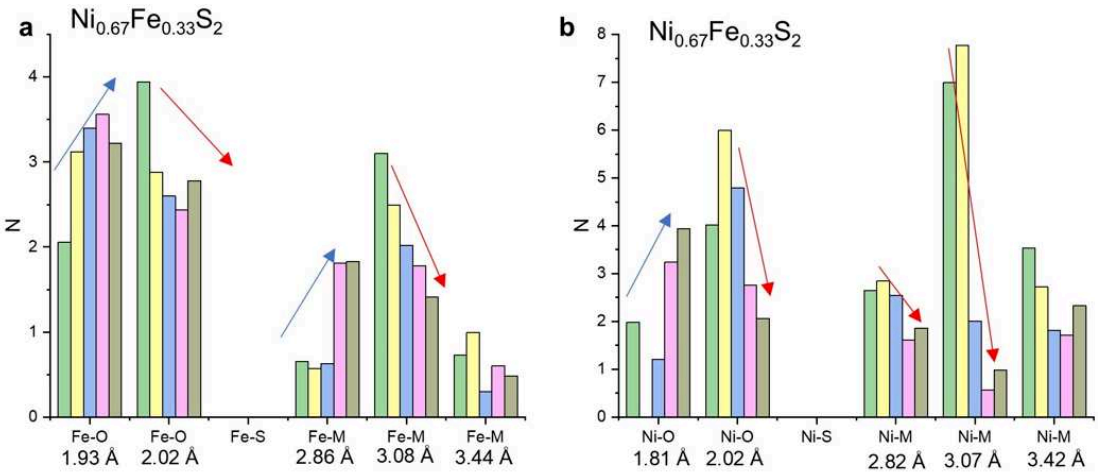

Fig. S32 | Coordination number during activation by CP. Coordination number changes in $Ni_{0.67}Fe_{0.33}S_2$ in a 0.3-1.7 V potential range (green to brown colors and arrows). **a,** iron data, **b,** nickel data.

Tab. S6 | EXAFS simulation parameters for $Ni_{0.67}Fe_{0.33}S_2$ during activation at CP: Fe.

	$Ni_{0.67}Fe_{0.33}S_2$ OCV			$Ni_{0.67}Fe_{0.33}S_2$ 0.30 V		
	R [Å]	N	$2\sigma^2$	R [Å]	N	$2\sigma^2$
Fe-O	1.98	5.74	0.018	1.93	2.06	0.015
Fe-O	2.02	0.26	0.018	2.02	3.94	0.015
Fe-M	2.85	0.94	0.015	2.86	0.66	0.015
Fe-M	3.05	2.57	0.015	3.08	3.10	0.015
Fe-M	3.48	0.82	0.015	3.49	0.73	0.015

	$Ni_{0.67}Fe_{0.33}S_2$ 0.30 V back			$Ni_{0.67}Fe_{0.33}S_2$ 1.35 V		
	R [Å]	N	$2\sigma^2$	R [Å]	N	$2\sigma^2$
Fe-O	1.98	5.83	0.017	1.98	5.11	0.019
Fe-O	2.02	0.17	0.017	2.02	0.89	0.019
Fe-M	2.90	0.75	0.015	2.84	0.59	0.015
Fe-M	3.07	2.66	0.015	3.06	2.47	0.015
Fe-M	3.50	0.75	0.015	3.50	1.05	0.015

	$Ni_{0.67}Fe_{0.33}S_2$ 1.45 V			$Ni_{0.67}Fe_{0.33}S_2$ 1.55 V		
	R [Å]	N	$2\sigma^2$	R [Å]	N	$2\sigma^2$
Fe-O	1.95	3.40	0.020	1.93	3.56	0.017
Fe-O	2.02	2.60	0.020	2.02	2.44	0.017
Fe-M	2.83	0.63	0.015	2.86	1.81	0.015
Fe-M	3.05	2.02	0.015	3.05	1.78	0.015
Fe-M	3.51	0.30	0.015	3.52	0.60	0.015

	$Ni_{0.67}Fe_{0.33}S_2$ 1.70 V					
	R [Å]	N	$2\sigma^2$			
Fe-O	1.90	3.22	0.014			
Fe-O	2.02	2.78	0.014			
Fe-M	2.86	1.83	0.015			
Fe-M	3.04	1.41	0.015			
Fe-M	3.46	0.49	0.015			

Tab. S7 | EXAFS simulation parameters for $Ni_{0.67}Fe_{0.33}S_2$ during activation at CP: Ni.

	$Ni_{0.67}Fe_{0.33}S_2$ OCV			$Ni_{0.67}Fe_{0.33}S_2$ 0.30 V		
	R [Å]	N	$2\sigma^2$	R [Å]	N	$2\sigma^2$
Ni-O	1.87	1.82	0.015	1.96	1.97	0.005
Ni-O	2.04	4.18	0.015	2.07	4.03	0.005
Ni-M	2.81	1.20	0.008	2.77	2.65	0.020
Ni-M	3.07	1.51	0.008	3.03	6.97	0.020
Ni-M	3.41	0.97	0.008	3.43	3.60	0.020

	$Ni_{0.67}Fe_{0.33}S_2$ 0.30 V back			$Ni_{0.67}Fe_{0.33}S_2$ 1.35 V		
	R [Å]	N	$2\sigma^2$	R [Å]	N	$2\sigma^2$
Ni-O			0.010			0.010
Ni-O	2.05	5.84	0.010	2.04	5.78	0.010
Ni-M	2.80	2.95	0.020	2.77	2.80	0.020
Ni-M	3.05	8.54	0.020	3.04	7.67	0.020
Ni-M	3.44	2.37	0.020	3.44	2.76	0.020

	$Ni_{0.67}Fe_{0.33}S_2$ 1.45 V			$Ni_{0.67}Fe_{0.33}S_2$ 1.55 V		
	R [Å]	N	$2\sigma^2$	R [Å]	N	$2\sigma^2$
Ni-O	1.87	2.67	0.011	1.87	3.91	0.010
Ni-O	2.05	3.33	0.011	2.05	2.09	0.010
Ni-M	2.79	1.47	0.007	2.80	1.91	0.004
Ni-M	3.08	1.00	0.007	3.11	0.48	0.004
Ni-M	3.41	0.83	0.007	3.40	0.42	0.004

	$Ni_{0.67}Fe_{0.33}S_2$ 1.70 V					
	R [Å]	N	$2\sigma^2$			
Ni-O	1.88	4.13	0.009			
Ni-O	2.05	1.87	0.009			
Ni-M	2.81	2.39	0.005			
Ni-M	3.13	0.69	0.005			
Ni-M	3.37	0.44	0.005			

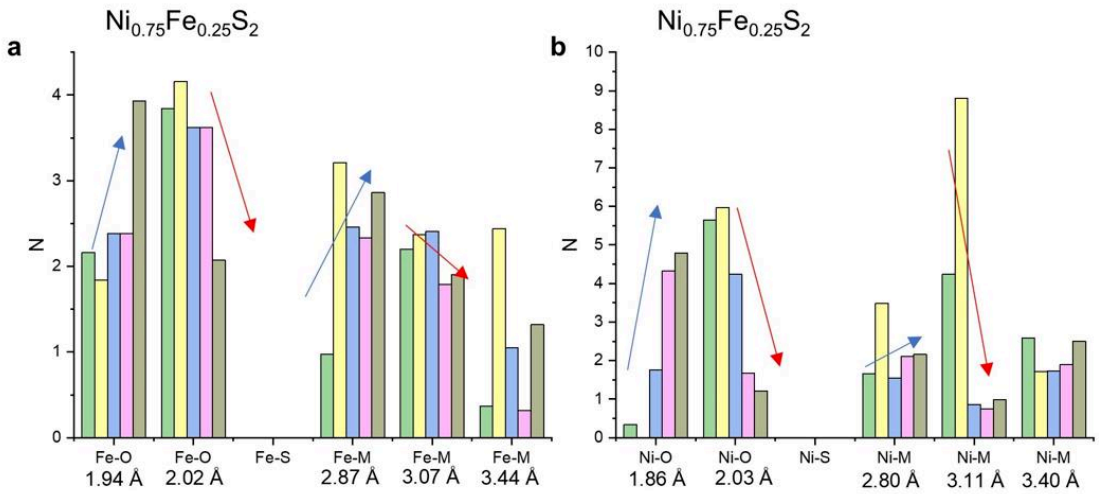

Fig. S33 | Coordination number during activation by CP. Coordination number changes in $Ni_{0.75}Fe_{0.25}S_2$ in a 0.3-1.7 V potential range (green to brown colors and arrows). **a,** iron data, **b,** nickel data.

Tab. S8 | EXAFS simulation parameters for $Ni_{0.75}Fe_{0.25}S_2$ during activation at CP: Fe.

	$Ni_{0.75}Fe_{0.25}S_2$ OCV			$Ni_{0.75}Fe_{0.25}S_2$ 0.30 V		
	R [Å]	N	$2\sigma^2$	R [Å]	N	$2\sigma^2$
Fe-O	1.99	5.84	0.019	1.94	2.16	0.017
Fe-O	2.02	0.17	0.019	2.02	3.84	0.017
Fe-M	2.86	0.95	0.015	2.87	0.97	0.015
Fe-M	3.06	2.07	0.015	3.07	2.20	0.015
Fe-M	3.44	0.54	0.015	3.44	0.37	0.015

	$Ni_{0.75}Fe_{0.25}S_2$ 0.30 V back			$Ni_{0.75}Fe_{0.25}S_2$ 1.35 V		
	R [Å]	N	$2\sigma^2$	R [Å]	N	$2\sigma^2$
Fe-O	1.98	5.87	0.017	1.95	1.84	0.016
Fe-O	2.02	0.13	0.017	2.02	4.16	0.016
Fe-M	2.82	0.15	0.015	3.04	3.21	0.015
Fe-M	3.06	1.86	0.015	3.21	2.37	0.015
Fe-M	3.52	2.52	0.015	3.46	2.44	0.015

	$Ni_{0.75}Fe_{0.25}S_2$ 1.45 V			$Ni_{0.75}Fe_{0.25}S_2$ 1.55 V		
	R [Å]	N	$2\sigma^2$	R [Å]	N	$2\sigma^2$
Fe-O	1.91	2.38	0.017	1.86	2.38	0.008
Fe-O	2.02	3.62	0.017	2.02	3.62	0.008
Fe-M	2.87	2.46	0.015	2.85	2.33	0.015
Fe-M	3.08	2.41	0.015	3.04	1.79	0.015
Fe-M	3.95	1.05	0.015	3.48	0.32	0.015

	$Ni_{0.75}Fe_{0.25}S_2$ 1.70 V					
	R [Å]	N	$2\sigma^2$			
Fe-O	1.92	3.93	0.018			
Fe-O	2.02	2.07	0.018			
Fe-M	2.88	2.86	0.015			
Fe-M	3.12	1.90	0.015			
Fe-M	3.43	1.32	0.015			

Tab. S9 | EXAFS simulation parameters for $Ni_{0.75}Fe_{0.25}S_2$ during activation at CP: Ni.

	$Ni_{0.75}Fe_{0.25}S_2$ OCV			$Ni_{0.75}Fe_{0.25}S_2$ 0.30 V		
	R [Å]	N	$2\sigma^2$	R [Å]	N	$2\sigma^2$
Ni-O	1.89	2.39	0.011	1.80	0.35	0.012
Ni-O	2.06	3.61	0.011	2.04	5.65	0.012
Ni-M	2.81	2.41	0.015	2.84	1.66	0.020
Ni-M	3.08	3.33	0.015	3.06	4.24	0.012
Ni-M	3.39	2.22	0.015	3.45	2.58	0.020

	$Ni_{0.75}Fe_{0.25}S_2$ 0.30 V back			$Ni_{0.75}Fe_{0.25}S_2$ 1.35 V		
	R [Å]	N	$2\sigma^2$	R [Å]	N	$2\sigma^2$
Ni-O						
Ni-O	2.05	6.00	0.012	2.05	5.97	0.012
Ni-M	2.81	3.35	0.020	2.80	3.49	0.020
Ni-M	3.05	9.59	0.020	3.04	8.80	0.020
Ni-M	5.70	3.29	0.020	3.45	1.72	0.020

	$Ni_{0.75}Fe_{0.25}S_2$ 1.45 V			$Ni_{0.75}Fe_{0.25}S_2$ 1.55 V		
	R [Å]	N	$2\sigma^2$	R [Å]	N	$2\sigma^2$
Ni-O	1.86	1.76	0.004	1.89	4.32	0.009
Ni-O	2.03	4.24	0.020	2.13	1.68	0.009
Ni-M	2.80	1.54	0.005	2.81	2.11	0.003
Ni-M	3.11	0.86	0.005	3.14	0.75	0.003
Ni-M	3.40	1.73	0.020	3.32	1.90	0.020

	$Ni_{0.75}Fe_{0.25}S_2$ 1.70 V					
	R [Å]	N	$2\sigma^2$			
Ni-O	1.88	4.79	0.011			
Ni-O	2.16	1.21	0.011			
Ni-M	2.80	2.16	0.003			
Ni-M	3.13	0.99	0.003			
Ni-M	3.32	2.50	0.020			

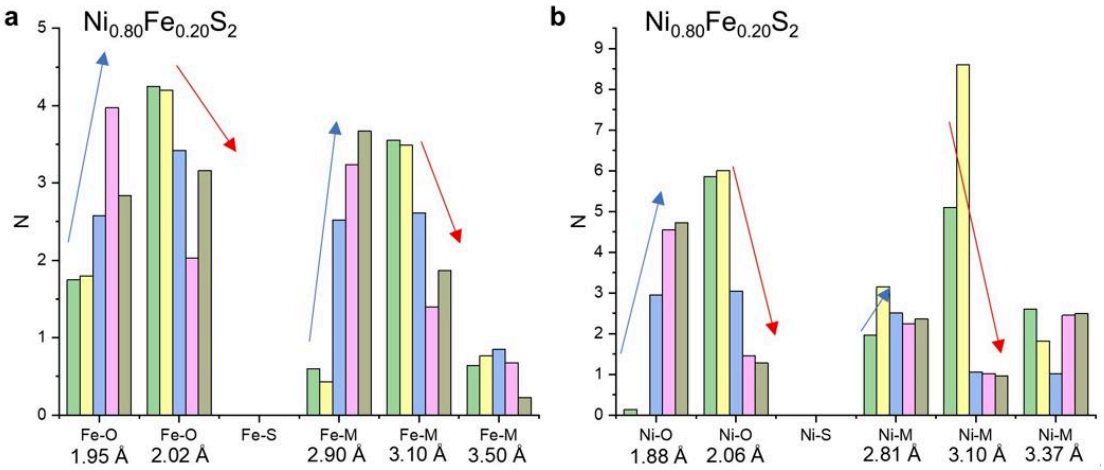

Fig. S34 | Coordination number during activation by CP. Coordination number changes in $Ni_{0.80}Fe_{0.20}S_2$ in a 0.3-1.7 V potential range (green to brown colors and arrows). **a,** iron data, **b,** nickel data.

Tab. S10 | EXAFS simulation parameters for $Ni_{0.80}Fe_{0.20}S_2$ during activation at CP: Fe.

	$Ni_{0.80}Fe_{0.20}S_2$ OCV			$Ni_{0.80}Fe_{0.20}S_2$ 0.30 V		
	R [Å]	N	$2\sigma^2$	R [Å]	N	$2\sigma^2$
Fe-O	1.91	1.63	0.014	1.95	1.75	0.012
Fe-O	2.02	4.37	0.014	2.02	4.25	0.012
Fe-M	2.88	1.34	0.015	2.90	0.60	0.015
Fe-M	3.09	2.93	0.015	3.10	3.55	0.015
Fe-M	3.44	0.44	0.015	3.50	0.64	0.015

	$Ni_{0.80}Fe_{0.20}S_2$ 0.30 V back			$Ni_{0.80}Fe_{0.20}S_2$ 1.35 V		
	R [Å]	N	$2\sigma^2$	R [Å]	N	$2\sigma^2$
Fe-O	1.96	2.48	0.013	1.96	3.12	0.017
Fe-O	2.02	3.52	0.013	2.02	2.88	0.017
Fe-M	2.86	0.96	0.015	2.84	0.57	0.015
Fe-M	3.09	4.07	0.015	3.06	2.49	0.015
Fe-M	3.51	1.03	0.015	3.51	1.00	0.015

	$Ni_{0.80}Fe_{0.20}S_2$ 1.45 V			$Ni_{0.80}Fe_{0.20}S_2$ 1.55 V		
	R [Å]	N	$2\sigma^2$	R [Å]	N	$2\sigma^2$
Fe-O	1.92	2.58	0.013	1.92	3.97	0.015
Fe-O	2.02	3.42	0.013	2.02	2.03	0.015
Fe-M	2.88	2.52	0.015	2.86	3.24	0.015
Fe-M	3.10	2.61	0.013	3.09	1.40	0.015
Fe-M	3.84	0.85	0.013	3.45	0.68	0.015

	$Ni_{0.80}Fe_{0.20}S_2$ 1.70 V					
	R [Å]	N	$2\sigma^2$			
Fe-O	1.88	2.84	0.009			
Fe-O	2.02	3.16	0.009			
Fe-M	2.86	3.67	0.015			
Fe-M	3.07	1.87	0.015			
Fe-M	3.56	0.23	0.015			

Tab. S11 | EXAFS simulation parameters for $Ni_{0.80}Fe_{0.20}S_2$ during activation at CP: Ni.

	$Ni_{0.80}Fe_{0.20}S_2$ OCV			$Ni_{0.80}Fe_{0.20}S_2$ 0.30 V		
	R [Å]	N	$2\sigma^2$	R [Å]	N	$2\sigma^2$
Ni-O	1.89	2.43	0.012	1.80	0.14	0.014
Ni-O	2.06	3.57	0.012	2.04	5.86	0.014
Ni-M	2.81	3.03	0.015	2.81	1.96	0.020
Ni-M	3.07	3.63	0.015	3.06	5.10	0.014
Ni-M	3.39	1.79	0.020	3.43	2.61	0.020

	$Ni_{0.80}Fe_{0.20}S_2$ 0.30 V back			$Ni_{0.80}Fe_{0.20}S_2$ 1.35 V		
	R [Å]	N	$2\sigma^2$	R [Å]	N	$2\sigma^2$
Ni-O						
Ni-O	2.05	6.00	0.013	2.05	6.00	0.014
Ni-M	2.82	3.62	0.020	2.80	3.15	0.020
Ni-M	3.06	10.00	0.020	3.05	8.60	0.020
Ni-M	5.34	3.06	0.020	3.42	1.82	0.020

	$Ni_{0.80}Fe_{0.20}S_2$ 1.45 V			$Ni_{0.80}Fe_{0.20}S_2$ 1.55 V		
	R [Å]	N	$2\sigma^2$	R [Å]	N	$2\sigma^2$
Ni-O	1.88	2.95	0.007	1.88	4.55	0.009
Ni-O	2.06	3.05	0.020	2.14	1.45	0.009
Ni-M	2.81	2.51	0.007	2.80	2.25	0.003
Ni-M	3.10	1.06	0.007	3.14	1.02	0.003
Ni-M	3.37	1.01	0.020	3.30	2.45	0.020

	$Ni_{0.80}Fe_{0.20}S_2$ 1.70 V					
	R [Å]	N	$2\sigma^2$			
Ni-O	1.88	4.72	0.009			
Ni-O	2.16	1.28	0.009			
Ni-M	2.81	2.36	0.003			
Ni-M	3.13	0.97	0.003			
Ni-M	3.32	2.49	0.020			

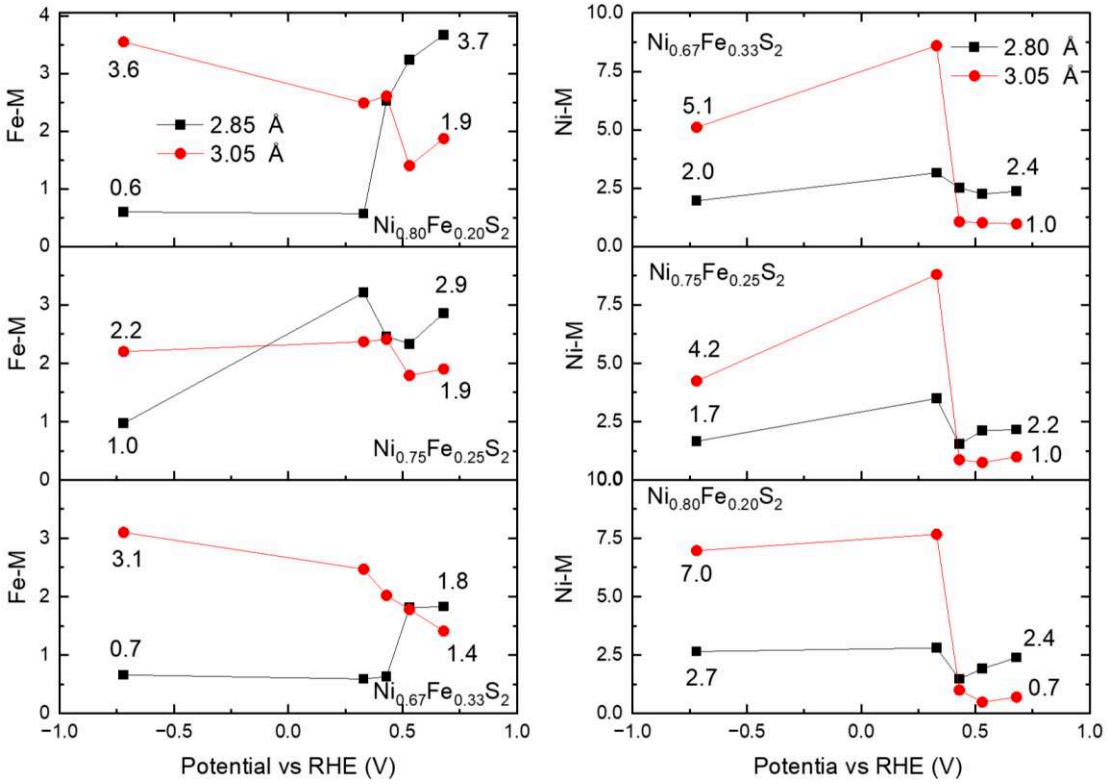

Fig. S35 | Summary of coordination number during activation by CP. Metal-metal distance coordination number changes during increasing electrochemical potentials from **a,** Fe and **b,** Ni EXAFS analysis of $Ni_xFe_{1-x}S_2$ (x=0.67, 0.75, 0.80).

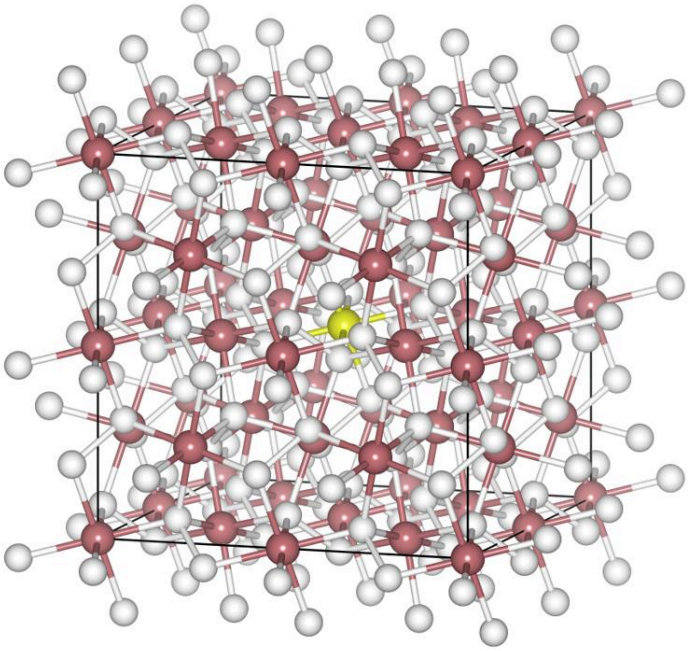

Fig. S36 | A supercell used for DFT calculation. The structure of $Ni_{0.67}Fe_{0.33}S_2$ is fcc and the supercell has in total of 96 atoms (32 Ni+Fe in total and 64 S, Fe: yellow, Ni: brown, white: S)

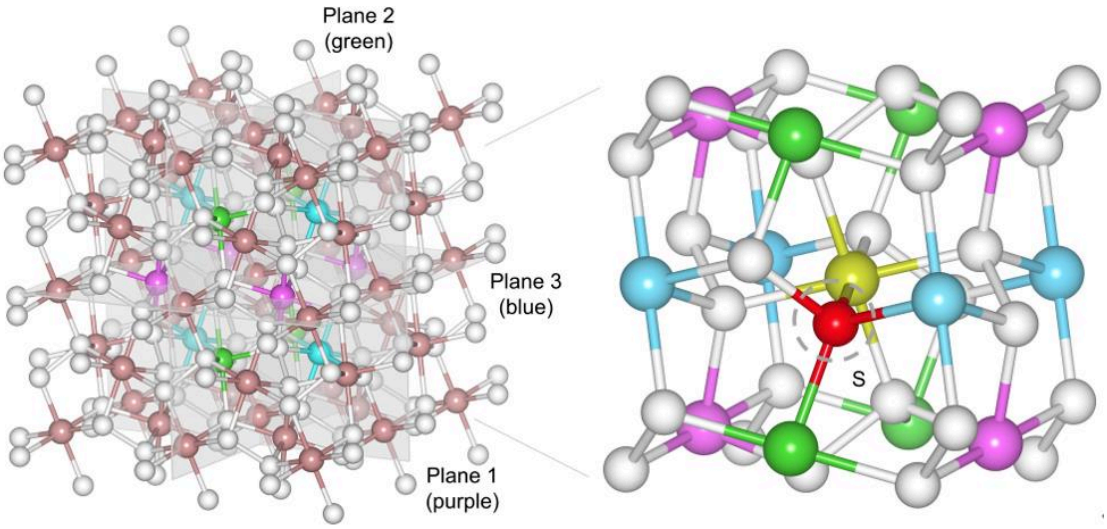

Fig. S37 | Crystal structure. A design is presented for replacing Ni with Fe in the NiS_2 and FeS_2 structures, both of which exhibit an fcc (face-centered cubic) arrangement with a coordination number of 12. To accommodate the higher Ni concentration in the material, NiS_2 serves as the fundamental structure. Planes 1, 2, and 3 limit the atomic range, and the vacancies of S atoms are formed within this limited range, *e.g.* the red S atom.

We utilized the face-centered cube (FCC) structures of NiS_2 with a 2×2×2 supercell as the initial structure, involving 94 atoms in total (**Suppl. Fig. 36**), and substituted the central Ni atom at coordinates (1/2, 1/2, 1/2) with Fe. Given that the coordination number of the FCC structure is 12, these atoms are evenly and symmetrically distributed across the (100), (010), and (001) crystal planes. Thus, these 12 Ni atoms were sequentially substituted by Fe atoms on the different crystal planes (**Suppl. Fig. 37**).

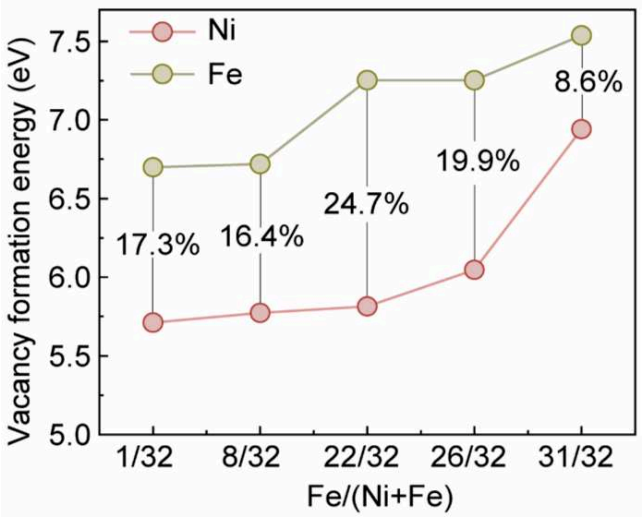

Fig. S38 | Vacancy formation energy for different $Ni_xFe_{1-x}S_2$ with Fe/Ni ratios. Fe and Ni vacancy formation energy for different $Ni_xFe_{1-x}S_2$ with Fe/Ni ratios from 1/32, 8/32, 22/32, 26/32, 31/32.

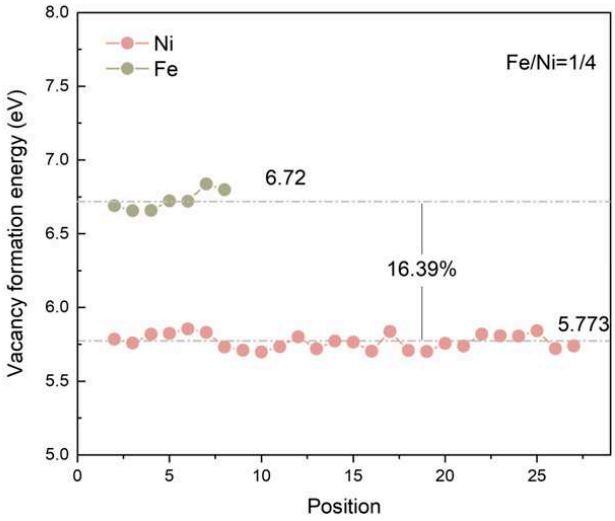

Fig. S39 | Vacancy formation energy at different positions of the supercell with Fe/Ni=1/4. Fe vacancy formation energy (yellow) at 7 positions with the average value of 6.72 eV and Ni vacancy formation energy (red) at 27 positions with the average value of 5.773 eV. The average vacancy formation energy of Fe is 16.39% higher than that of Ni, indicating Ni is easier to escape the crystal and then be oxidized.

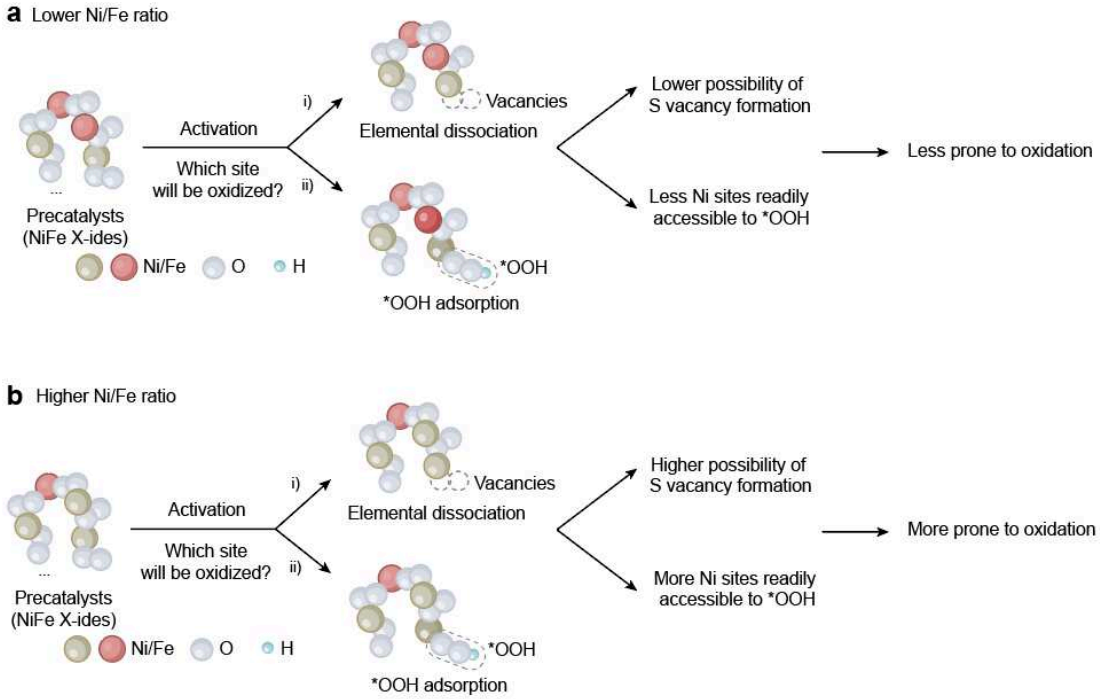

Fig. S40 | Summary of composition-dependent active site activation. a, Lower possibility of S vacancy formation, less Ni sites readily accessible to *OOH and thus less prone to oxidation. **b,** Higher possibility of S vacancy formation, more Ni sites readily accessible to *OOH and thus more prone to oxidation.

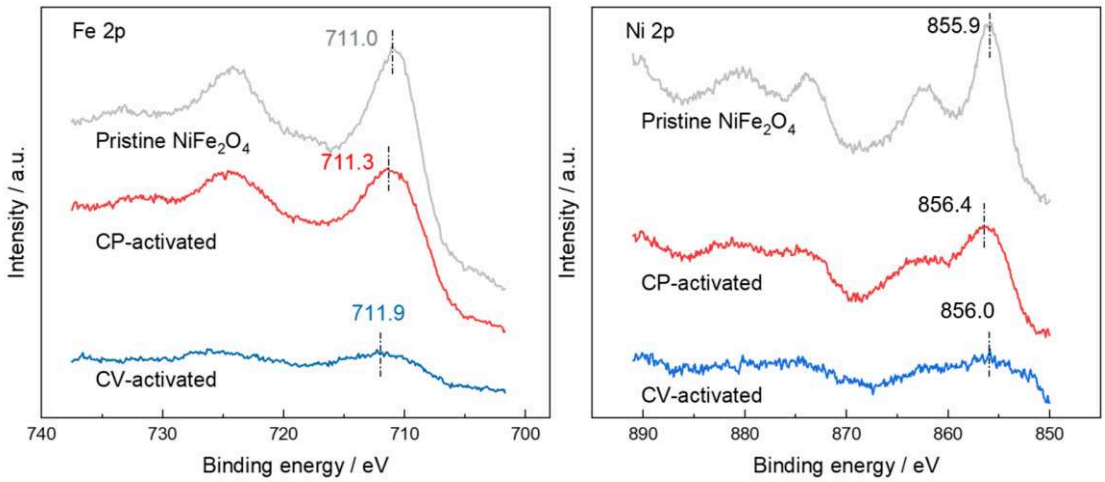

Fig. S41 | Surface chemical state analysis of $NiFe_2O_4$. XPS of $NiFe_2O_4$ before and after CP at 1.7 V or CV activation from 1.0-1.7 V at 100 $mV \cdot s^{-1}$.

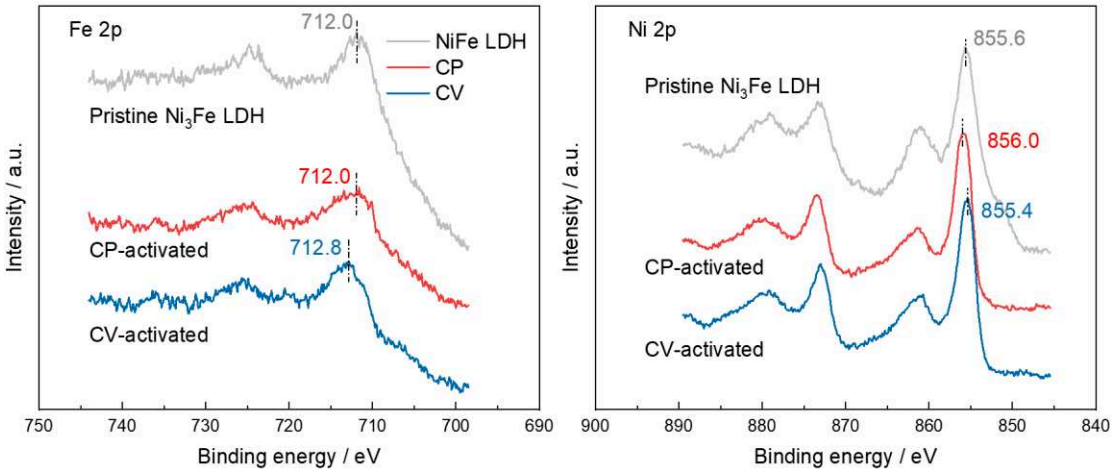

Fig. S42 | Surface chemical state analysis of Ni_3Fe LDH. XPS of Ni_3Fe LDH before and after CP at 1.7 V or CV activation from 1.0-1.7 V at 100 $mV \cdot s^{-1}$.

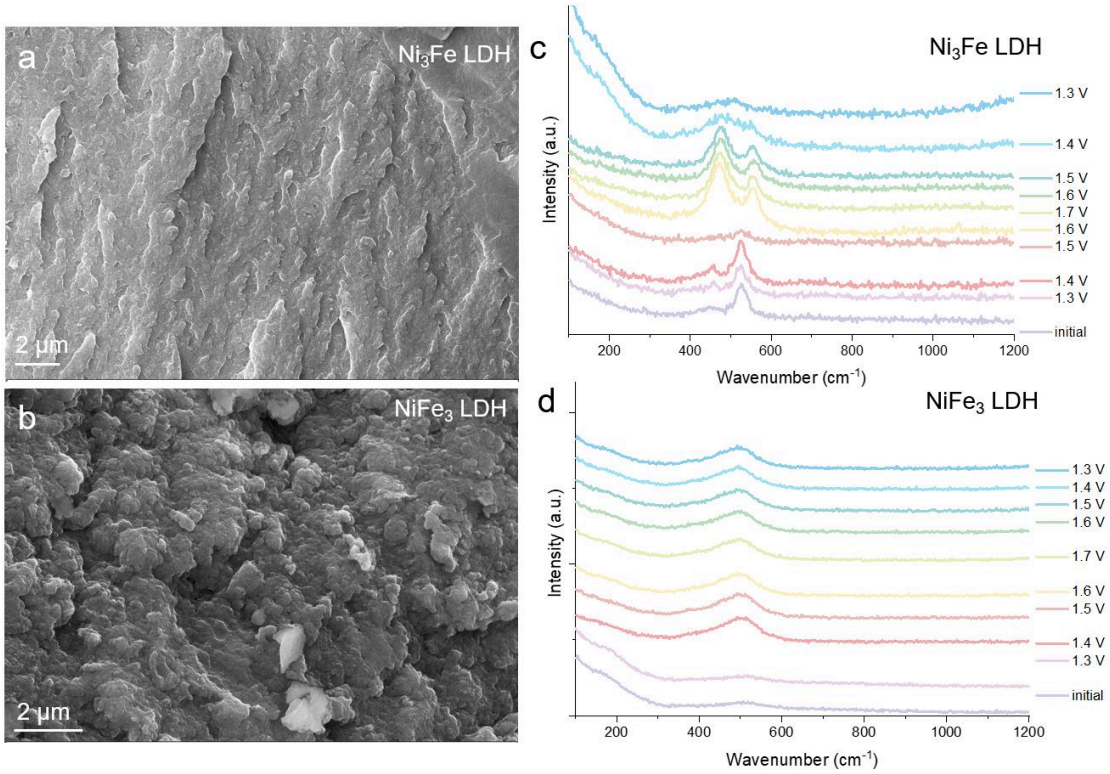

Fig. S43 | Morphology and in-situ Raman spectroscopy. a, b, SEM images of Ni_3Fe and $NiFe_3$ LDHs. **c, d,** In-situ Raman spectroscopy of Ni_3Fe and $NiFe_3$ LDHs from 1.3-1.7 V and then back to 1.3 V.

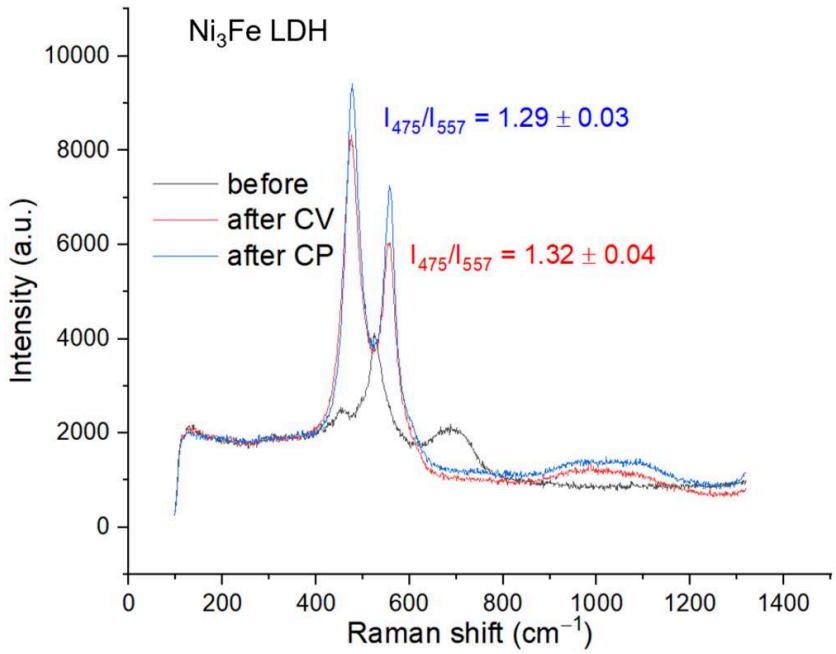

Fig. S44 | Ex-situ Raman spectroscopy. Ex-situ Raman spectroscopy of Ni_3Fe LDH before and after CP and CV activation.

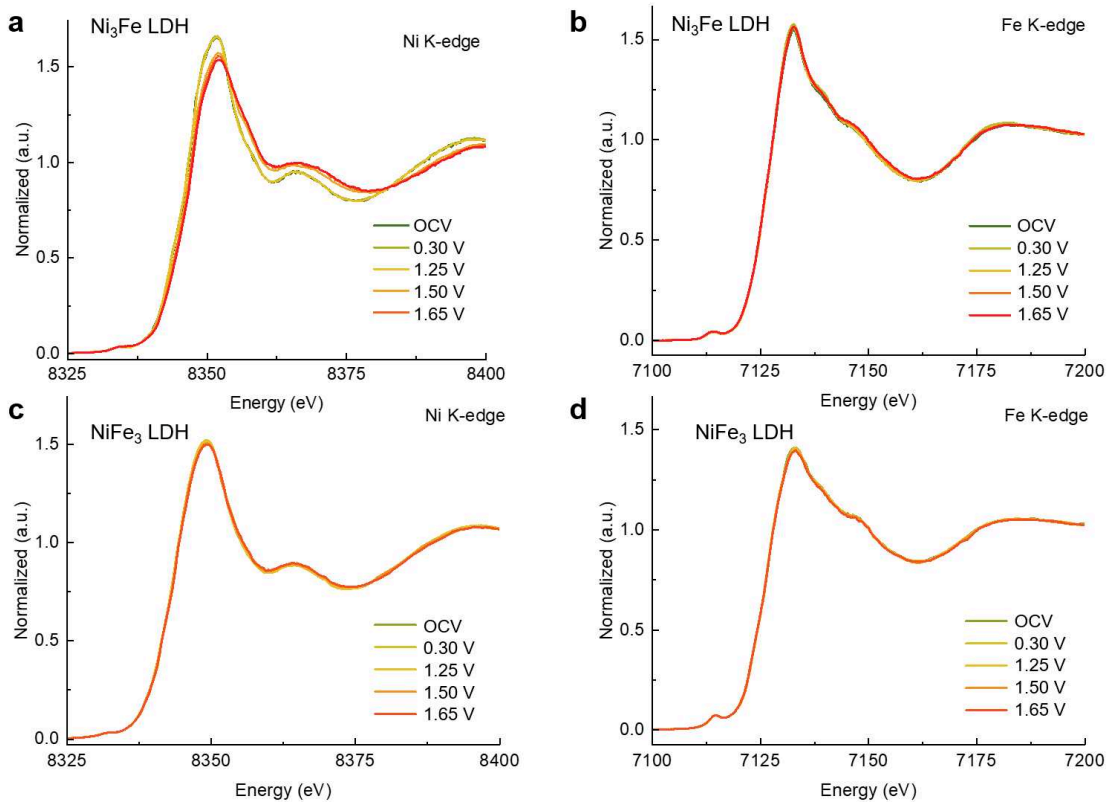

Fig. S45 | Operando XANES spectra at varying potentials for Ni_3Fe and $NiFe_3$ LDH. CP at OCP, 0.30 1.25, 1.55, 1.65 at the **a, c,** Ni and **b, d,** Fe K-edges, respectively.

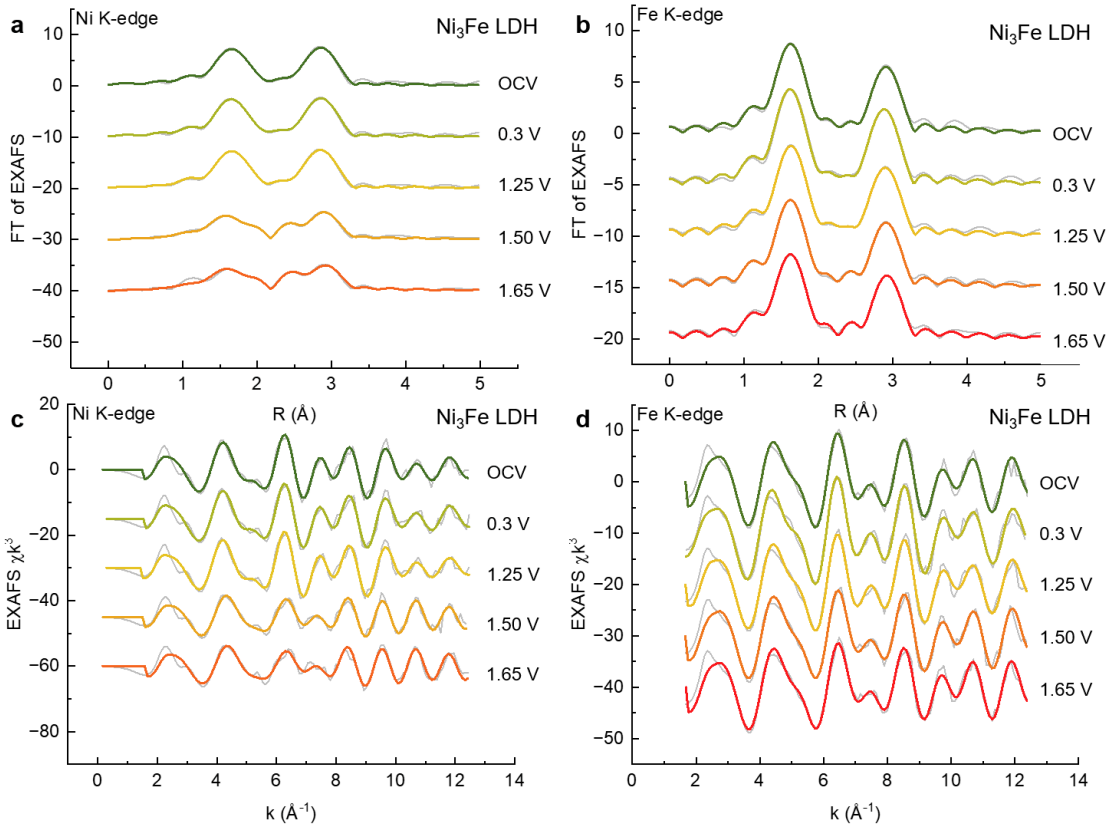

Fig. S46 | EXAFS analysis of Ni_3Fe LDH. a, c, Ni K edges and **b, d,** Fe k edges EXAFS spectra before and after CP activation at OCV, 0.3, 1.25, 1.50, 1.65 V.

Tab. S12 | EXAFS simulation parameters for Ni_3Fe LDH before and after CP activation.

		Ni3Fe LDH_Ni_K-edge_OCV		Ni3Fe LDH_Ni_K-edge_0.3 V		Ni3Fe LDH_Ni_K-edge_1.25 V		Ni3Fe LDH_Ni_K-edge_1.50 V		Ni3Fe LDH_Ni_K-edge_1.65 V	
		R [Å]	N	R [Å]	N	R [Å]	N	R [Å]	N	R [Å]	N
First shell	Ni-O	2.00	2.9	2.13	2.1	2.00	2.9	1.93	2.0	1.93	1.8
	Ni-O	2.12	2.3	2.01	3.2	2.12	2.5	2.09	2.4	2.09	2.3
Second shell	Ni-Ni	2.81	0.3	2.814	0.5	2.80	0.6	2.84	1.9	2.84	2.0
	Ni-Ni	3.10	6.4	3.10	7.0	3.10	7.5	3.10	4.1	3.10	3.5
	Ni-O total		5.2		5.2		5.4		4.4		4.1
	Ni-Ni first shell		0.3		0.5		0.6		1.9		2.0

		Ni3Fe LDH_Fe_K-edge_OCV		Ni3Fe LDH_Fe_K-edge_-0.3 V		Ni3Fe LDH_Fe_K-edge_1.25 V		Ni3Fe LDH_Fe_K-edge_1.50 V		Ni3Fe LDH_Fe_K-edge_1.65 V	
		R [Å]	N	R [Å]	N	R [Å]	N	R [Å]	N	R [Å]	N
First shell	Fe-O	1,962*	0*	1,968*	0*	1,96*	0*	1,95*	0*	1,95*	0*
	Fe-O	2.00	5.0	2.00	5.3	2.00	4.6	2.00	4.8	2.00	4.7
Second shell	Fe-Fe	2.88	0.9	2.86	1.1	2.88	0.7	2.87	1.0	2.88	1.2
	Fe-Fe	3.11	4.1	3.10	5.6	3.11	4.3	3.11	3.7	3.11	3.7
	Fe-O total		5.0		5.3		4.6		4.8		4.7
	Fe-Fe first shell		0.9		1.1		0.7		1.0		1.2

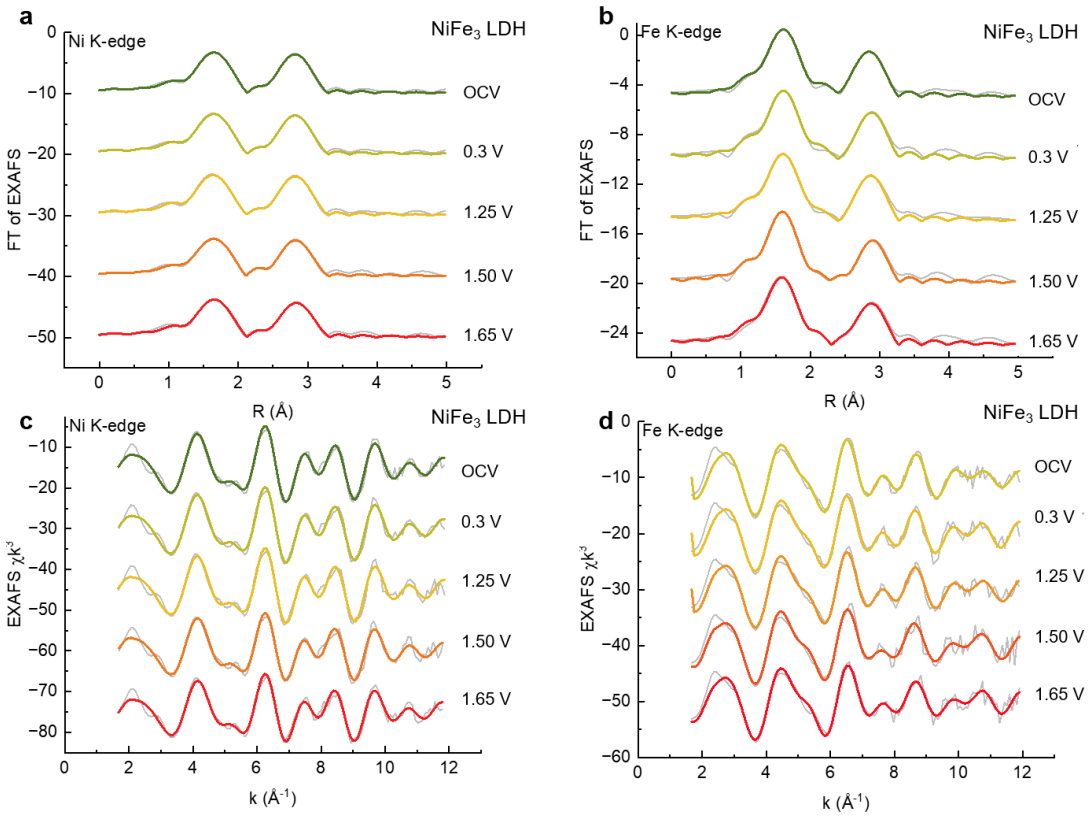

Fig. S47 | EXAFS analysis of $NiFe_3$ LDH. a, c, Ni K edges and **b, d,** Fe k edges EXAFS spectra before and after CP activation at OCV, 0.3, 1.25, 1.50, 1.65 V.

Tab. S13 | EXAFS simulation parameters for $NiFe_3$ LDH before and after CP activation.

		$NiFe_3$ LDH_Ni_K-edge_OCV		$NiFe_3$ LDH_Ni_K-edge_0.3 V		$NiFe_3$ LDH_Ni_K-edge_1.25 V		$NiFe_3$ LDH_Ni_K-edge_1.50 V		$NiFe_3$ LDH_Ni_K-edge_1.65 V	
		R [Å]	N	R [Å]	N	R [Å]	N	R [Å]	N	R [Å]	N
First shell	Ni-O	1.97	2.3	1.97	2.3	1.98	2.5	1.96	2.1	1.97	1.9
	Ni-O	2.09	3.2	2.09	3.2	2.09	2.9	2.09	3.1	2.08	3.0
Second shell	Ni-Ni	2.83	1.0	2.83	1.1	2.82	1.2	2.82	1.8	2.83	1.2
	Ni-Ni	3.07	7.7	3.07	7.8	3.07	8.1	3.07	8.4	3.08	7.5
	Ni-O total		5.5		5.5		5.4		5.2		4.9
	Ni-Ni first shell		1.0		1.1		1.2		1.8		1.2

		$NiFe_3$ LDH_Fe_K-edge_OCV		$NiFe_3$ LDH_Fe_K-edge_0.3 V		$NiFe_3$ LDH_Fe_K-edge_1.25 V		$NiFe_3$ LDH_Fe_K-edge_1.50 V		$NiFe_3$ LDH_Fe_K-edge_1.65 V	
		R [Å]	N	R [Å]	N	R [Å]	N	R [Å]	N	R [Å]	N
First shell	Fe-O	1,915*	0*	1,917*	0*	1,92*	0*	1,933*	0*	1,927*	0*
	Fe-O	1.98	4.2	1.99	4.2	1.98	4.2	1.97	4.1	1.97	4.2
Second shell	Fe-Fe	2.98	0.9	2.96	0.8	2.93	0.8	2.89	1.2	2.92	1.1
	Fe-Fe	3.11	1.4	3.11	1.7	3.09	2.4	3.09	3.1	3.09	2.2
	Fe-O total		4.2		4.2		4.2		4.1		4.2
	Fe-Fe first shell		0.9		0.8		0.8		1.2		1.1

Part 4: Mechanism of activation by different protocols

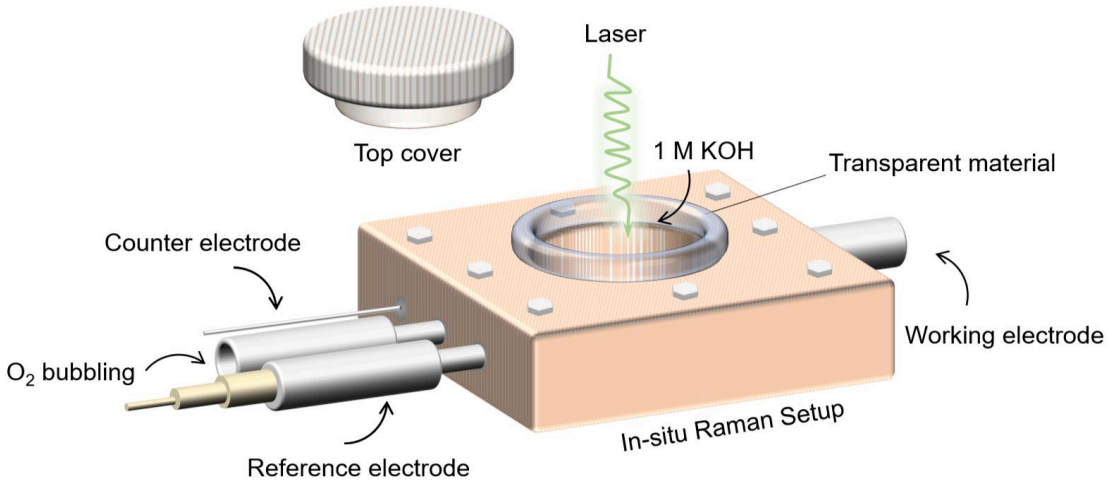

Fig. S48 | Setup for the operando Raman. The setup for an operando Raman spectroscopy experiment involves acquiring a Raman spectrometer with appropriate laser, sample handling equipment, optical components, calibration tools, operando condition control apparatus, data acquisition system, and analysis software, while prioritizing safety and adherence to experimental requirements.

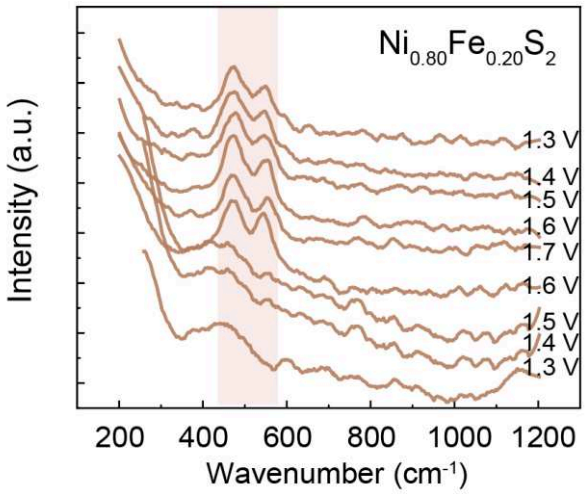

Fig. S49 | Operando Raman spectra of $Ni_{0.80}Fe_{0.20}S_2$ during CP activation within the range of 1.30-1.70 V.

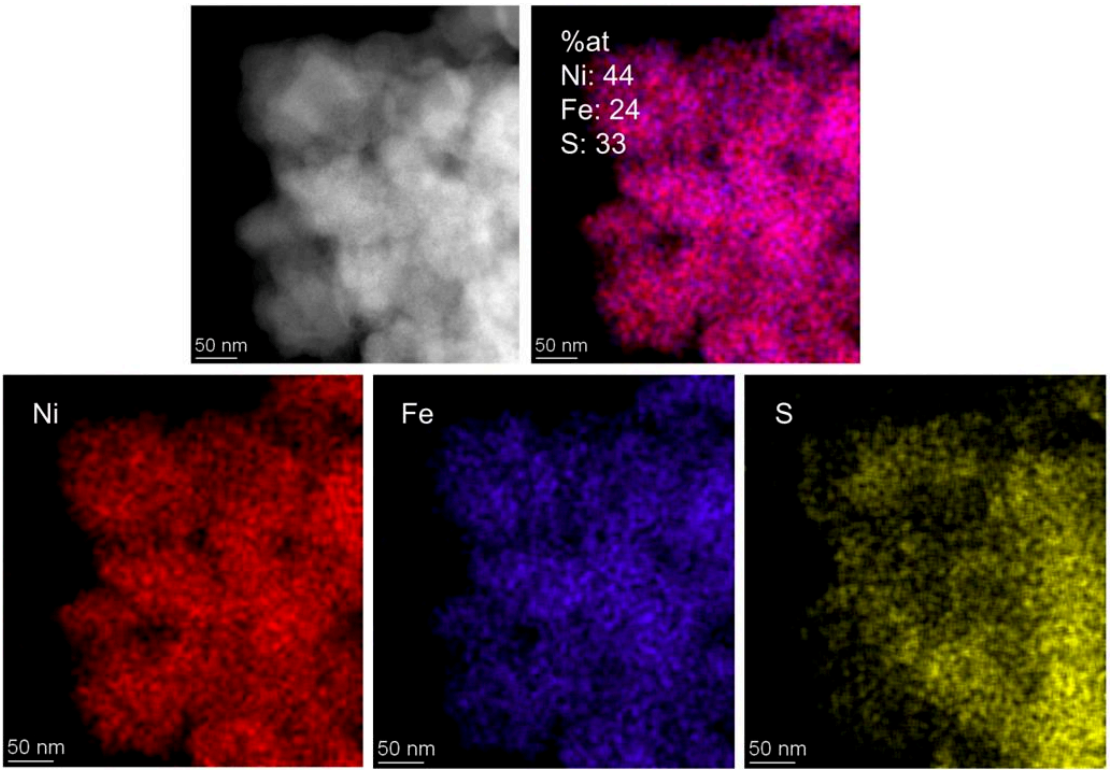

Fig. S50 | Morphology of $Ni_{0.67}Fe_{0.33}S_2$ after 50 CVs. HAADF and STEM images of $Ni_{0.67}Fe_{0.33}S_2$ nanoparticles after 50 CVs (position 1, with more S inside).

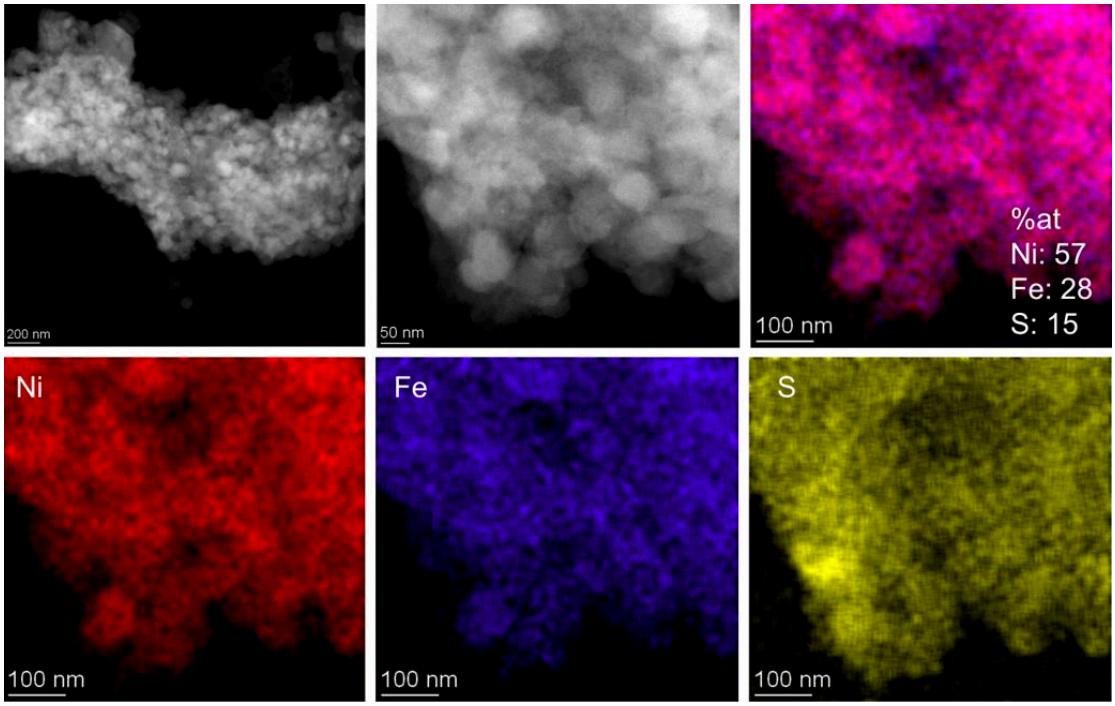

Fig. S51 | Morphology of $Ni_{0.67}Fe_{0.33}S_2$ after 50 CVs. HAADF and STEM images of $Ni_{0.67}Fe_{0.33}S_2$ nanoparticles after 50 CVs (position 2, with less S inside).

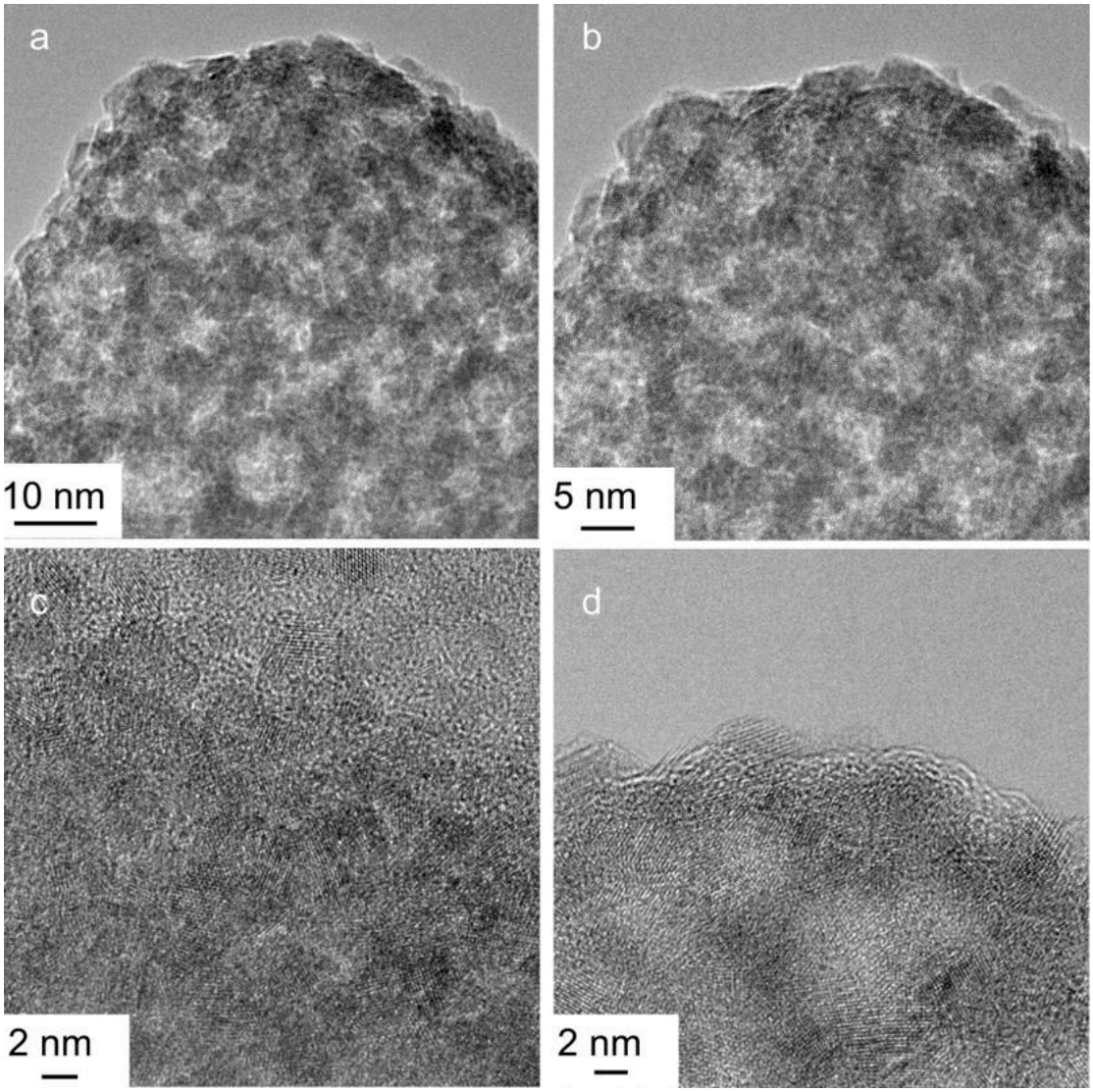

Fig. S52 | Morphology of $Ni_{0.67}Fe_{0.33}S_2$. HRTEM images of $Ni_{0.67}Fe_{0.33}S_2$ nanoparticles after 1 h at 1.7 V (position 1).

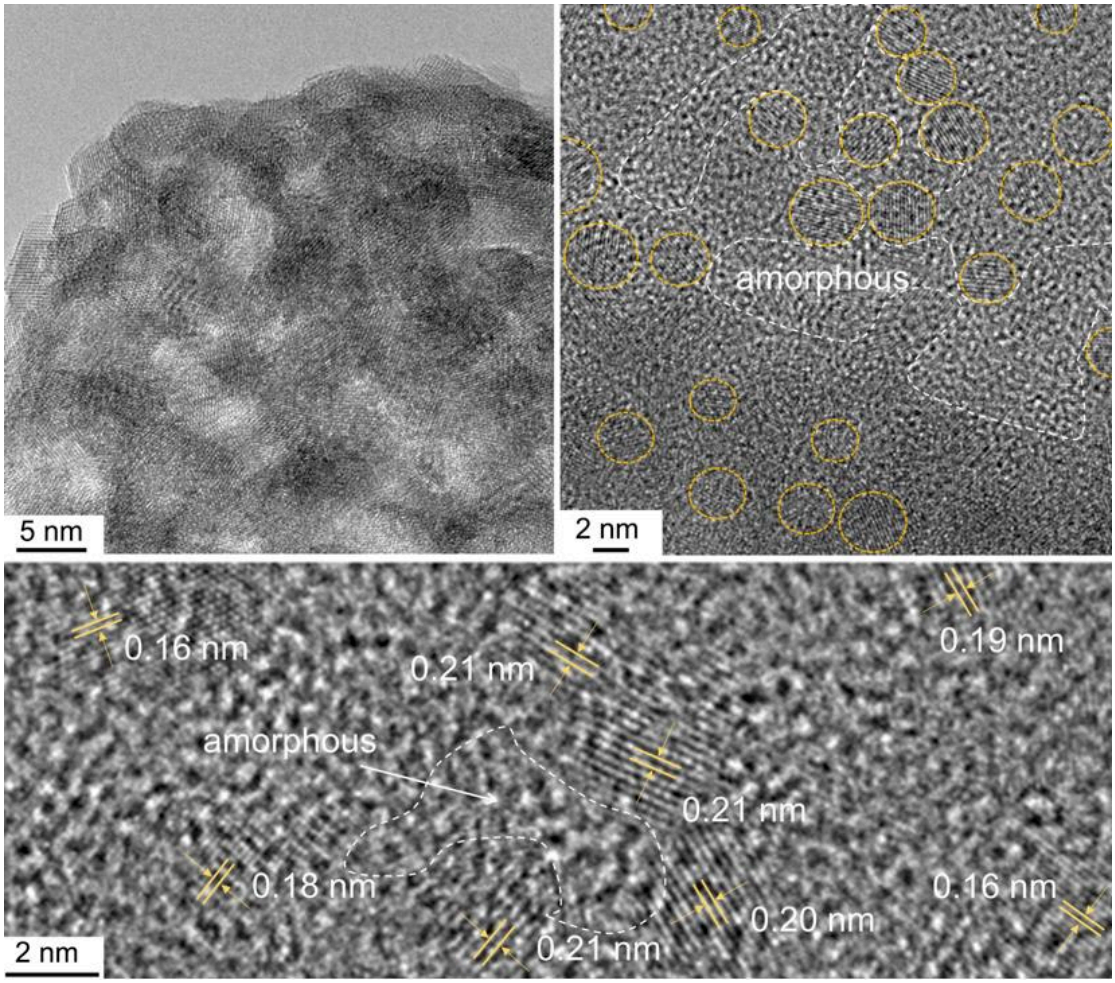

Fig. S53 | Morphology of $Ni_{0.67}Fe_{0.33}S_2$. HRTEM images of $Ni_{0.67}Fe_{0.33}S_2$ nanoparticles after 1 h at 1.7 V (position 2).

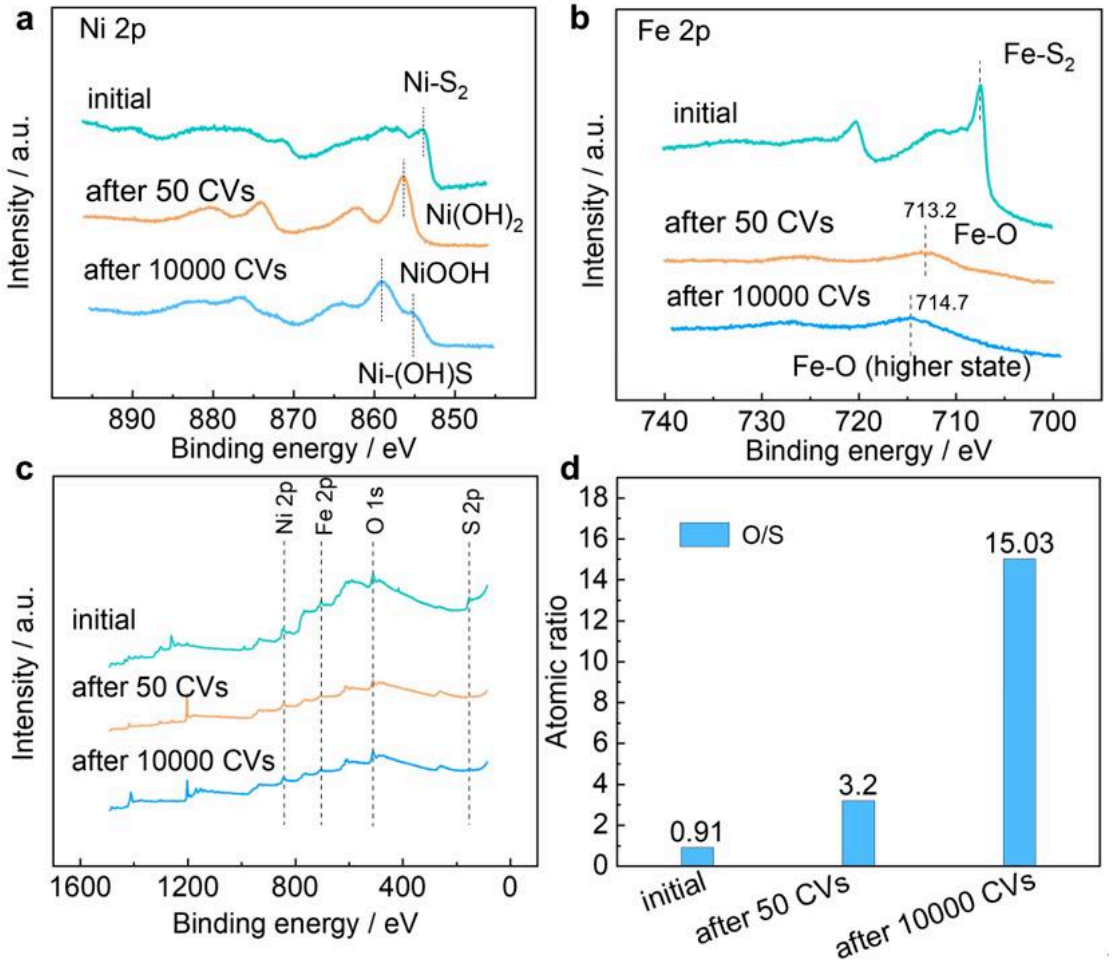

Fig. S54 | Surface chemical state of the $Ni_{0.67}Fe_{0.33}S_2$. High-resolution XPS spectra of $Ni_{0.67}Fe_{0.33}S_2$ coated on the nickel fiber in **a,** Ni 2p, **b,** Fe 2p and **c,** XPS survey of $Ni_{0.67}Fe_{0.33}S_2$, as well as **d,** summary of O/S in atomic ratio before and after 50 and 10000 CVs.

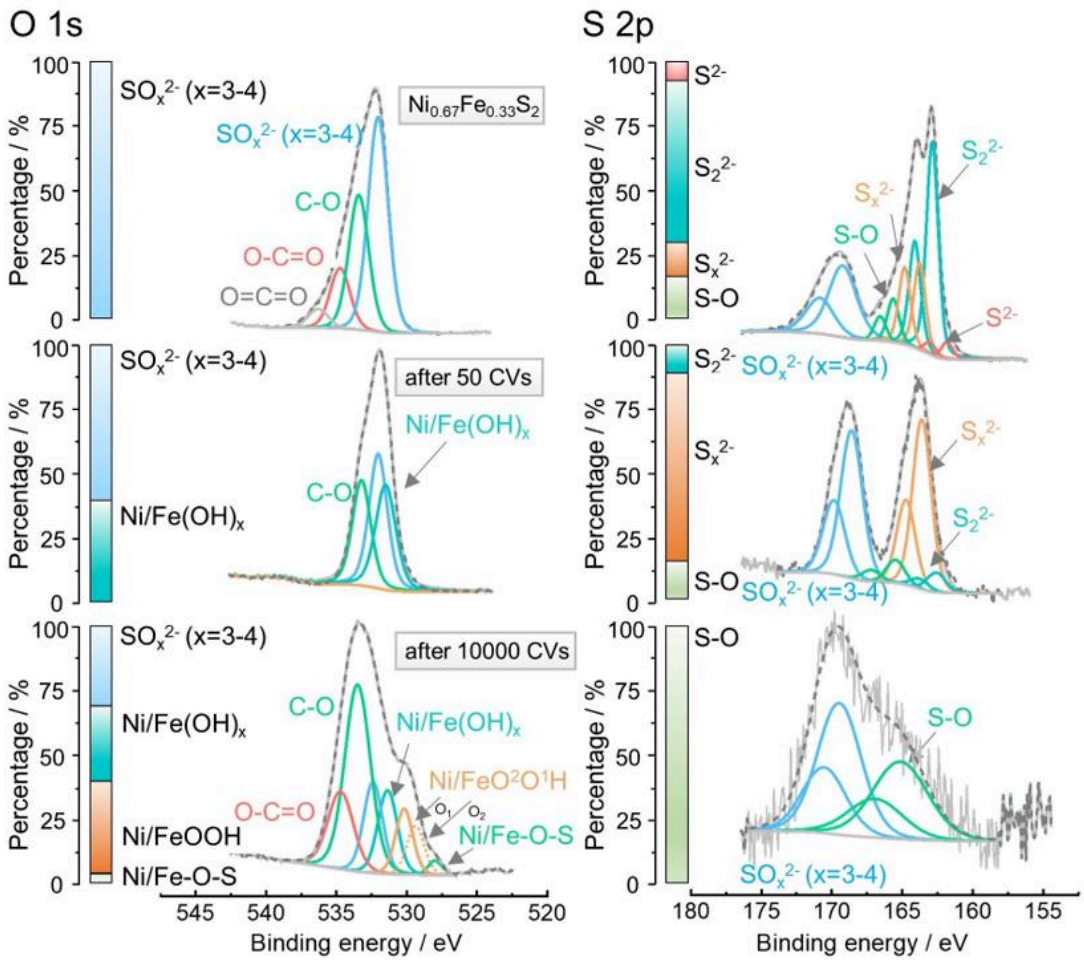

Fig. S55 | Surface chemical state of the $Ni_{0.67}Fe_{0.33}S_2$ anode. High-resolution XPS spectra of $Ni_{0.67}Fe_{0.33}S_2$ coated on the nickel fiber in O 1s, and S 2p regions after 50 and 10000 CVs.

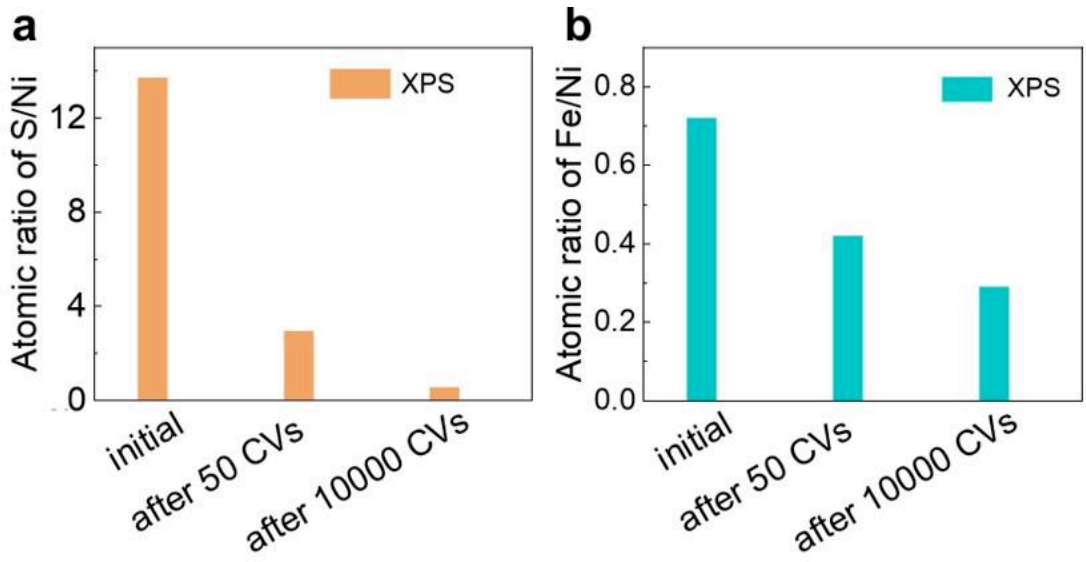

Fig. S56 | Surface composition of the $Ni_{0.67}Fe_{0.33}S_2$. Summary of O/S in atomic ratio before and after 50 and 10000 CVs by XPS survey: **a,** Atomic ratio of S/Ni. **b,** Atomic ratio of Fe/Ni.

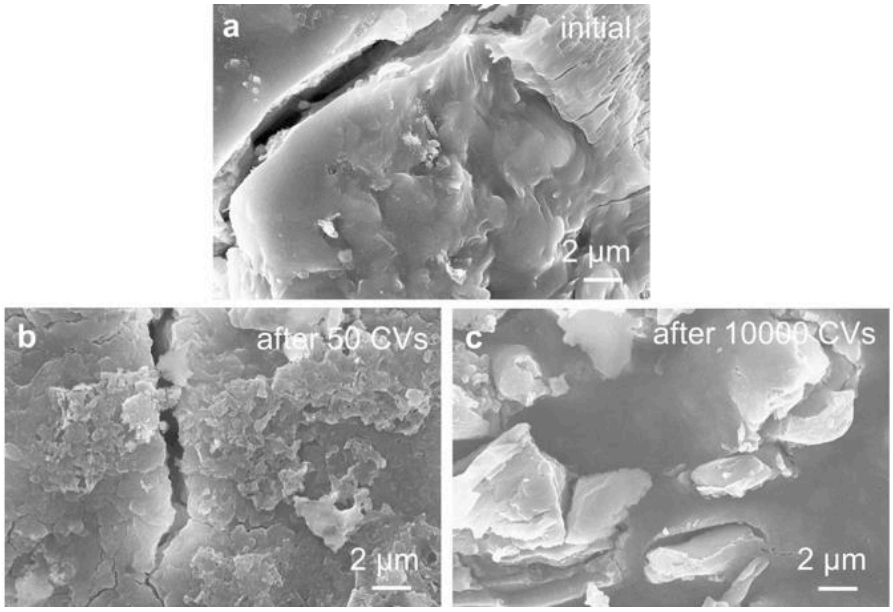

Fig. S57 | Surface morphology of $Ni_{0.67}Fe_{0.33}S_2$ anode. SEM images of $Ni_{0.67}Fe_{0.33}S_2$ anode before and after 50 and 10000 CVs.

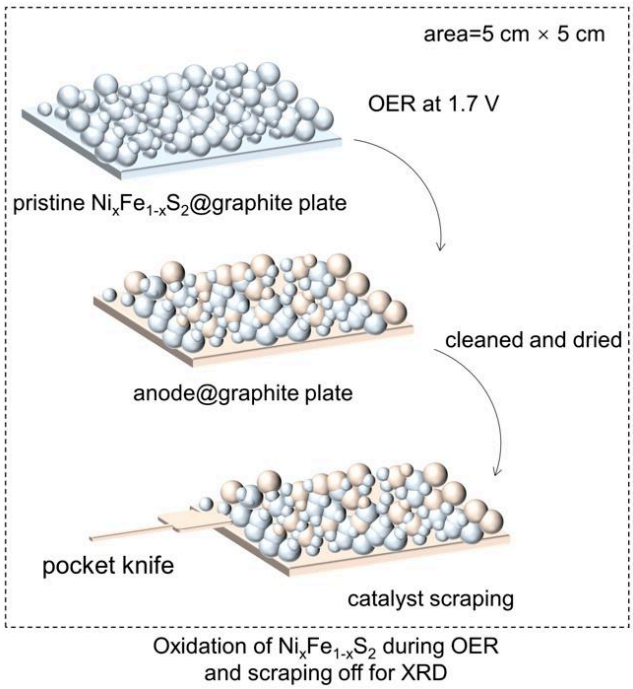

Fig. S58 | Schematic diagram of ex-situ XRD sample preparation. After OER testing (*e.g.* 1.7 V for 1 h), the catalyst was peeled off the matrix for testing the phase structures.

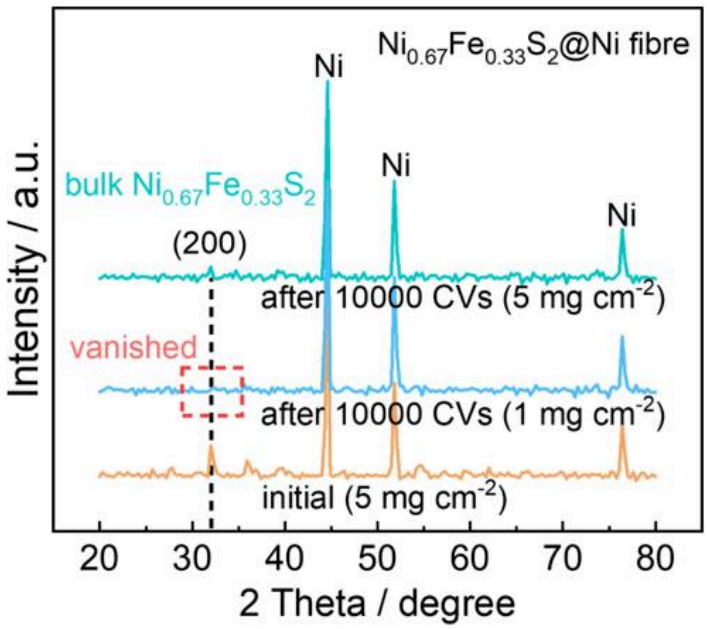

Fig. S59 | Ex-situ XRD before and after CV. Catalysts with different loadings were also sprayed on the nickel fiber electrode. After OER, the electrode was directly used for XRD testing. It can be seen that at higher loadings, the catalyst still maintains a partially crystalline state.

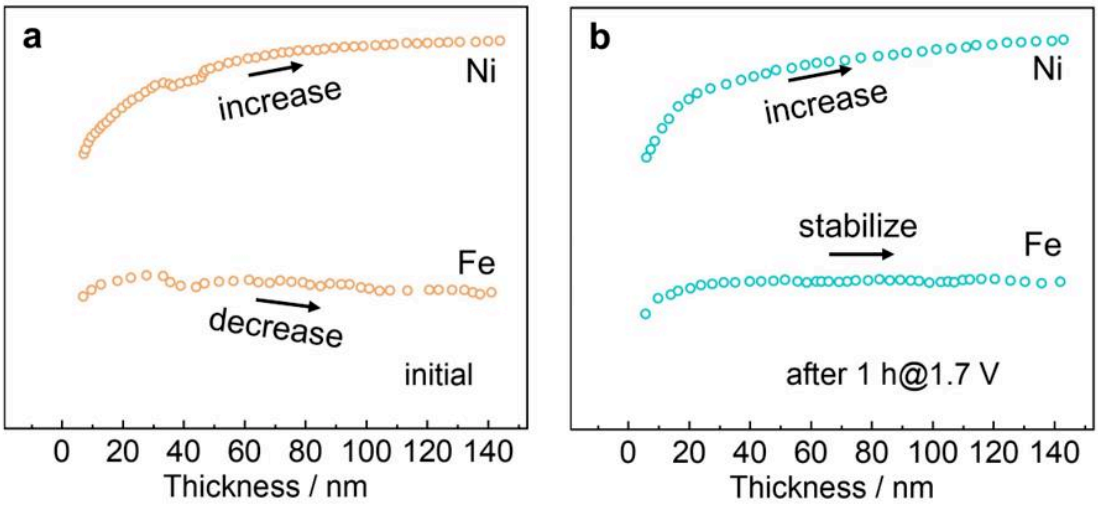

Fig. S60 | In-depth profile of $Ni_{0.67}Fe_{0.33}S_2$ before and after short-term OER. The time-of-flight secondary ion mass spectrometry (TOF-SIMS) of $Ni_{0.67}Fe_{0.33}S_2$ coated on the Si-based glass electrode: **a,** Ni, Fe trends of initial $Ni_{0.67}Fe_{0.33}S_2$ with the thickness, and **b,** corresponding trends after 1 h OER test at 1.7 V.

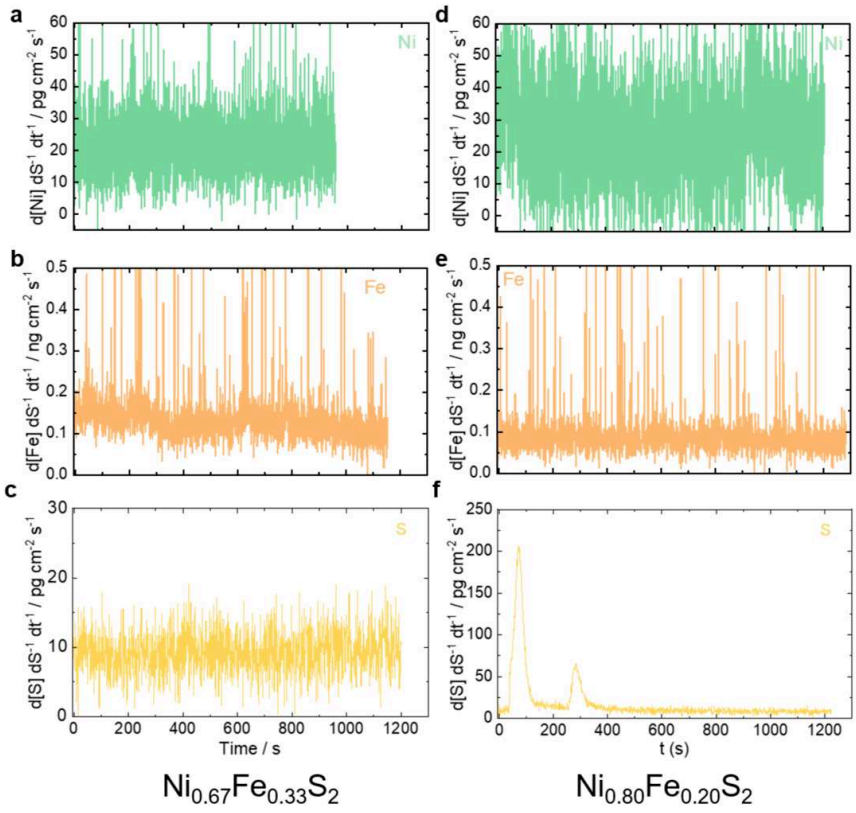

Fig. S61 | Operando ICP-MS measurements by fast cycling. Elemental dissolution via fast cycling of 50 CVs@100 mV·s^{-1} in 0.05 M KOH by using $Ni_{0.67}Fe_{0.33}S_2$ and $Ni_{0.80}Fe_{0.20}S_2$ as anode catalysts with the mass loading of 20 μg·cm^{-2} in a flow cell with the flow rate of 210 μL min^{-1}, and corresponding time-dependent dissolution rates of **a-c,** $Ni_{0.67}Fe_{0.33}S_2$, **d-f,** $Ni_{0.80}Fe_{0.20}S_2$.

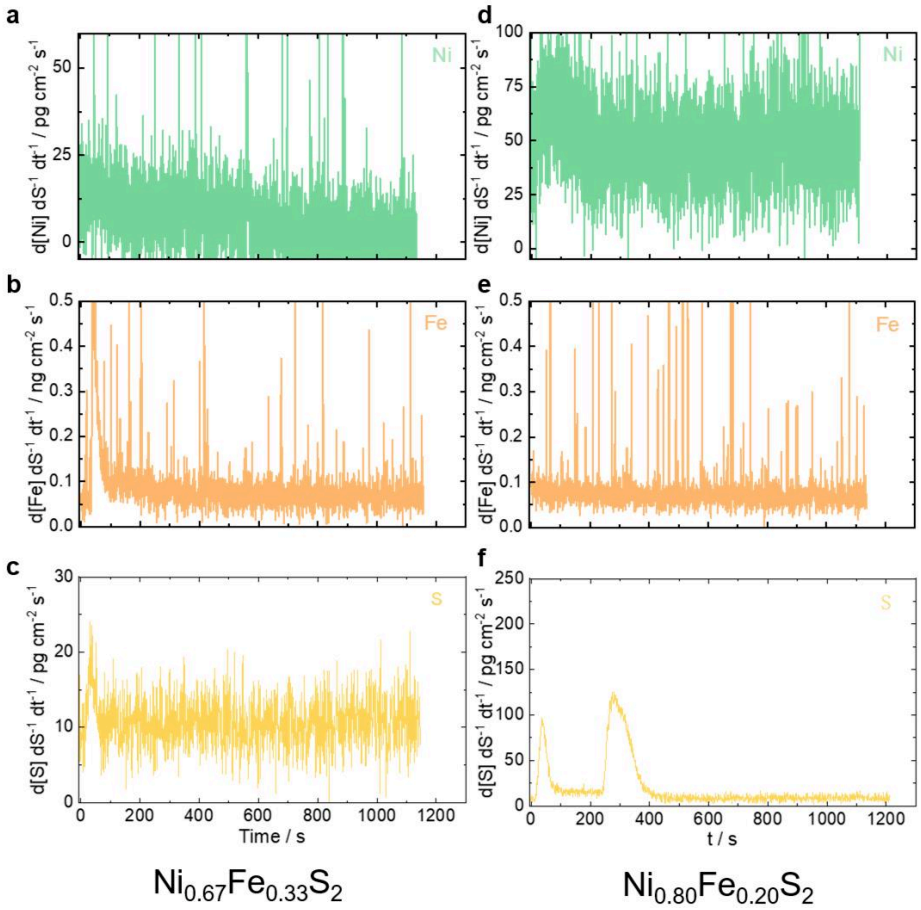

Fig. S62 | Operando ICP-MS measurements by galvanostatic hold. Elemental dissolution via galvanostatic hold at 1 mA·cm^{-2} (CP at ~1.5-1.55 V) in 0.05 M KOH by using $Ni_{0.67}Fe_{0.33}S_2$ and $Ni_{0.80}Fe_{0.20}S_2$ as anodic catalysts with the mass loading of 20 μg·cm^{-2} in a flow cell with the flow rate of 210 μL min^{-1}, and corresponding time-dependent dissolution rates of Ni, Fe, S of **a-c,** $Ni_{0.67}Fe_{0.33}S_2$, **d-f,** $Ni_{0.80}Fe_{0.20}S_2$.

Tab. S14 | Summary of catalyst dissolution.

Sample	Relative dissolution vs. initial loading, contact peak / %			Relative dissolution vs. initial loading, fast cycling/ %			Relative dissolution vs. initial loading, galvanostatic hold / %		
Elements	Ni	Fe	S	Ni	Fe	S	Ni	Fe	S
$Ni_{0.67}Fe_{0.33}S_2$	0.028±0.007	0.37±0.06	0.005±0.003	-	-	-	-	-	0.006±0.003
$Ni_{0.80}Fe_{0.20}S_2$	0.021±0.003	0.17±0.08	0.07±0.04	-	-	0.076±0.04	-	-	0.13±0.02

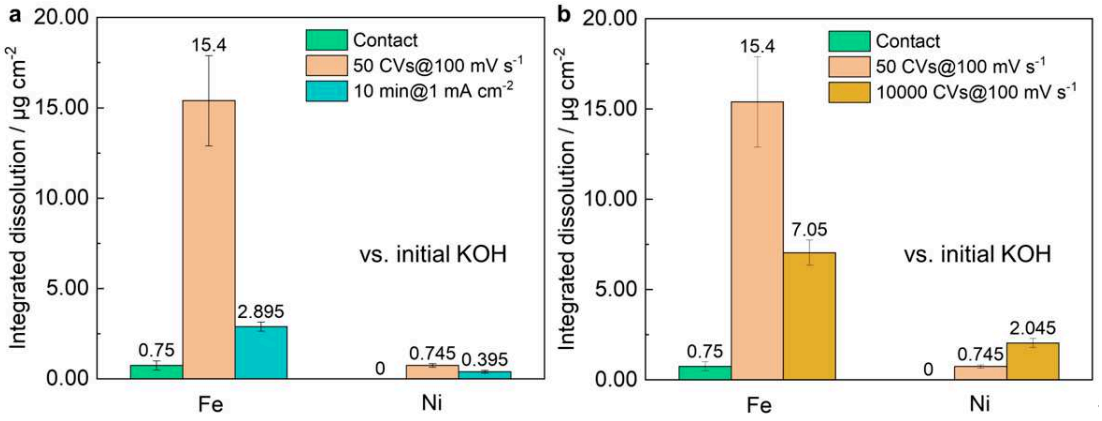

Fig. S63 | Summary of *ex-situ* ICPMS. a. Integrated dissolution of Ni, Fe, and S from $Ni_{0.67}Fe_{0.33}S_2$ during open circuit potential (contact peak), fast cycling of 50 CVs@100 mV·s^{-1}, galvanostatic hold at 1.0 mA·cm^{-2} (CP at ~1.45-1.50 V) for 10 min and 10000 CVs@100 mV· s^{-1}. **b,** Fe redeposition during long-term tests from *ex-situ* ICP-MS tests.

Tab. S15 | Summary of catalyst dissolution.

Sample	Relative dissolution vs. initial loading, contact peak / %		Relative dissolution vs. initial loading, 50 CVs / %		Relative dissolution vs. initial loading, 10 min@1 mA cm^{-2} / %	
Elements	Ni	Fe	Ni	Fe	Ni	Fe
$Ni_{0.67}Fe_{0.33}S_2$ (0.05 M KOH, in-situ)	0.028±0.007	0.37±0.06	-	-	-	-
$Ni_{0.67}Fe_{0.33}S_2$ (1 M KOH, ex-situ)	-	0.19±0.0006	0.19±0.0002	3.85±0.006	-	0.72±0.001

Protocol for ex-situ ICP-MS: Electrolyte: 1 M KOH; Catalyst loading 400 µg cm^{-2}

Sample	Relative dissolution vs. initial loading, contact peak / %		Relative dissolution vs. initial loading, 50 CVs / %		Relative dissolution vs. initial loading 10000 CVs / %	
Elements	Ni	Fe	Ni	Fe	Ni	Fe
$Ni_{0.67}Fe_{0.33}S_2$ (1 M KOH, ex-situ)	-	0.19±0.0006	0.19±0.0002	3.85±0.006	0.51±0.0006	1.76±0.002

To understand the impact of KOH concentration, we conducted the *ex situ* ICP-MS after precatalyst activation in 1 M KOH. The integrated dissolution of Ni and Fe (**Suppl. Fig. 63 and Suppl. Table 15**) shows a similar trend during the contact period, and CV greatly promotes Fe leaching and surface reconstruction, while CP is not sufficient for full catalyst activation, indicating catalyst reconstruction is highly relevant to the polarization conditions.

Notably, alkali ion concentration is another crucial factor for catalyst reconstruction, but it is

hard to enable a direct comparison between operando and *ex-situ* Fe loss during CV as catalyst loadings are different (20-fold higher for ex-situ) even though with 3.85%±0.006 Fe leaching in 1 M KOH but negligible in 0.05 M KOH. However, activation by CP clearly shows that the electrolyte plays a role: even at smaller mass-normalized current densities (2.5 mA mg^{-1}, cat.) the leached amount of Fe (0.720%±0.001) is higher than that of the operando measurement.

Part 5: Catalyst activity and stability in half cells

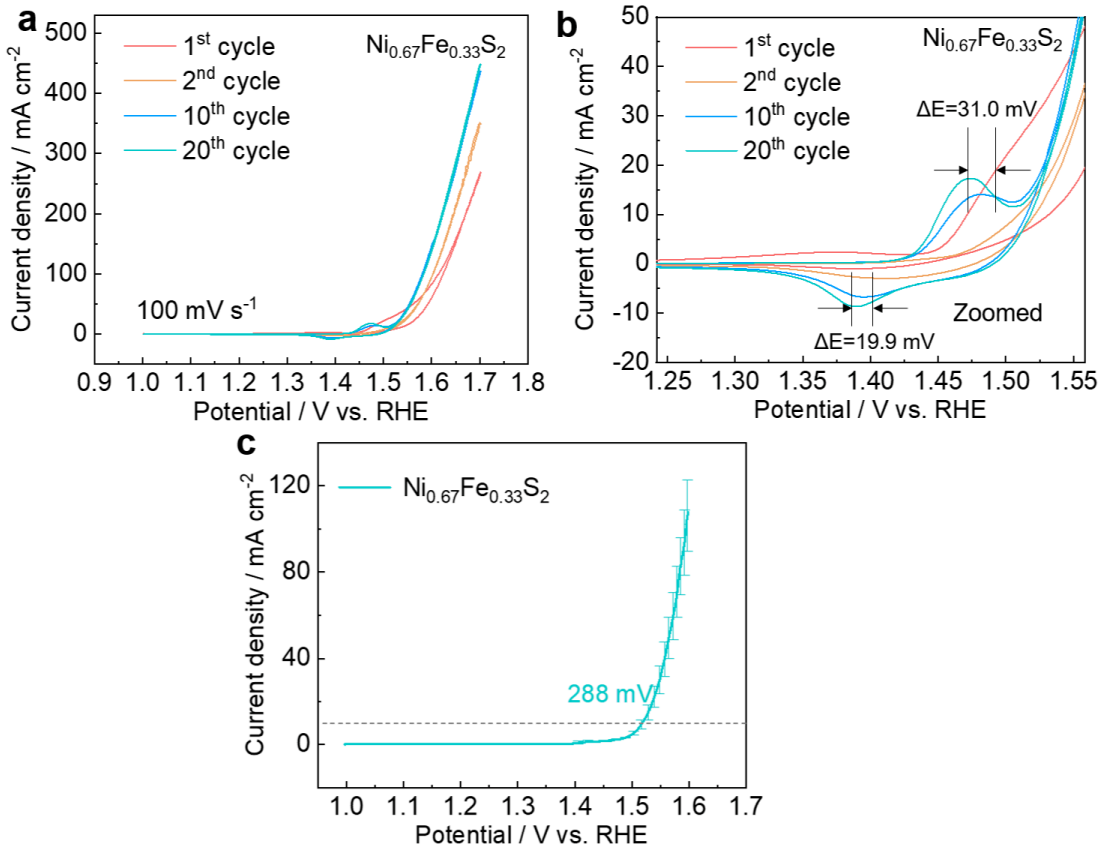

Fig. S64 | CV activation during 20 CVs and OER after activation on the RDE. a-d, CV curves of $Ni_{0.67}Fe_{0.33}S_2$ recorded at 100 mV·s^{-1} at the 1st, 10th and 20th cycle and corresponding zoomed area from 1.35-1.50 V. **c,** LSV curves of $Ni_{0.67}Fe_{0.33}S_2$ at 5 mV·s^{-1} after the above CV cycles.

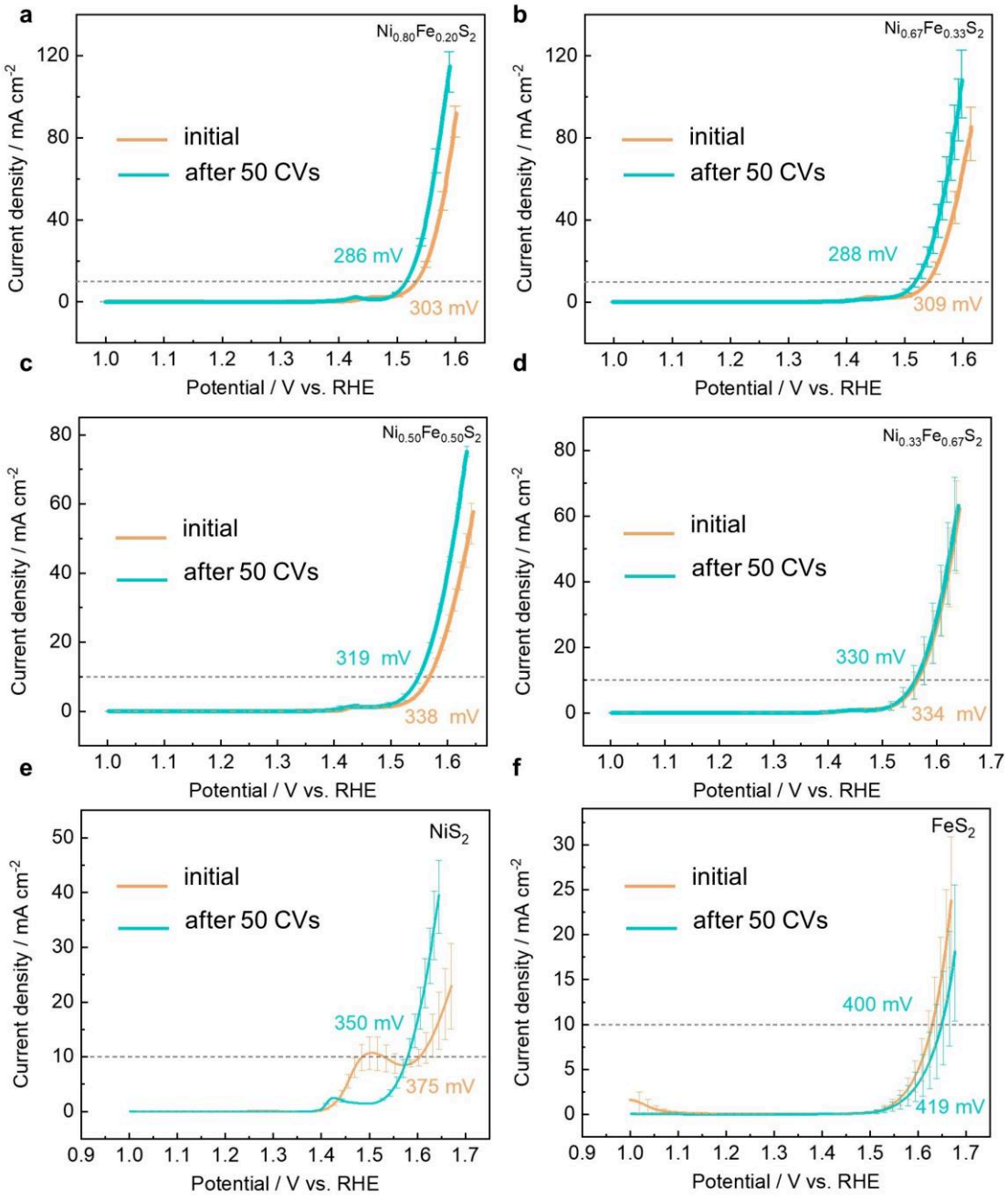

Fig. S65 | OER performance of $Ni_xFe_{1-x}S_2$ (x=0, 0.33, 0.50, 0.67, 0.80, 1) before and after 50 CVs on the RDE. LSV curves of $Ni_xFe_{1-x}S_2$ (x=0, 0.33, 0.50, 0.67, and 1) catalysts at 5 $mV \cdot s^{-1}$: **a,** $Ni_{0.80}Fe_{0.20}S_2$, **b,** $Ni_{0.67}Fe_{0.33}S_2$, **c,** $Ni_{0.50}Fe_{0.50}S_2$, **d,** $Ni_{0.33}Fe_{0.67}S_2$, **e,** NiS_2 and **f,** FeS_2.

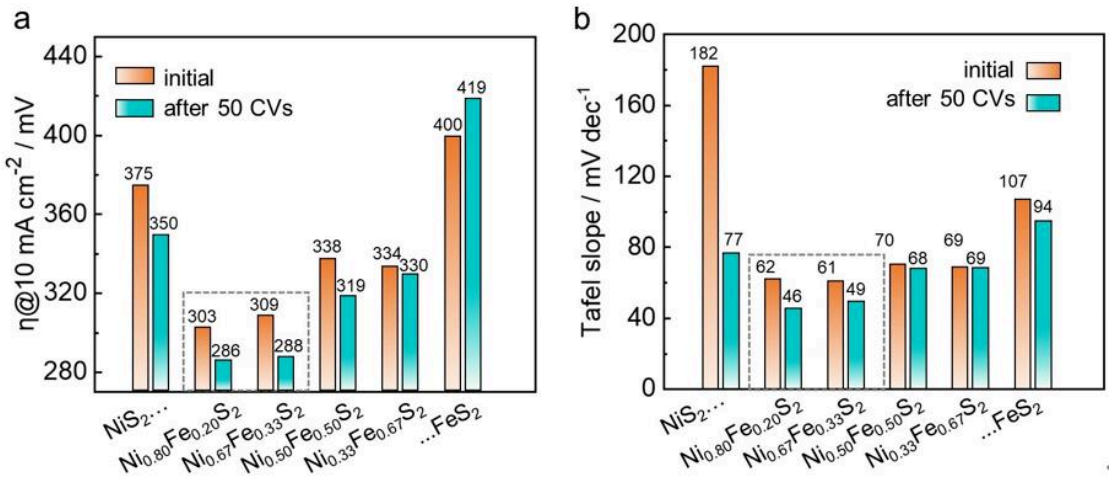

Fig. S66 | Summary of OER performance. a, Average overpotential at 10 mA·cm^{-2} and **b,** Tafel slope before and after 50 CVs.

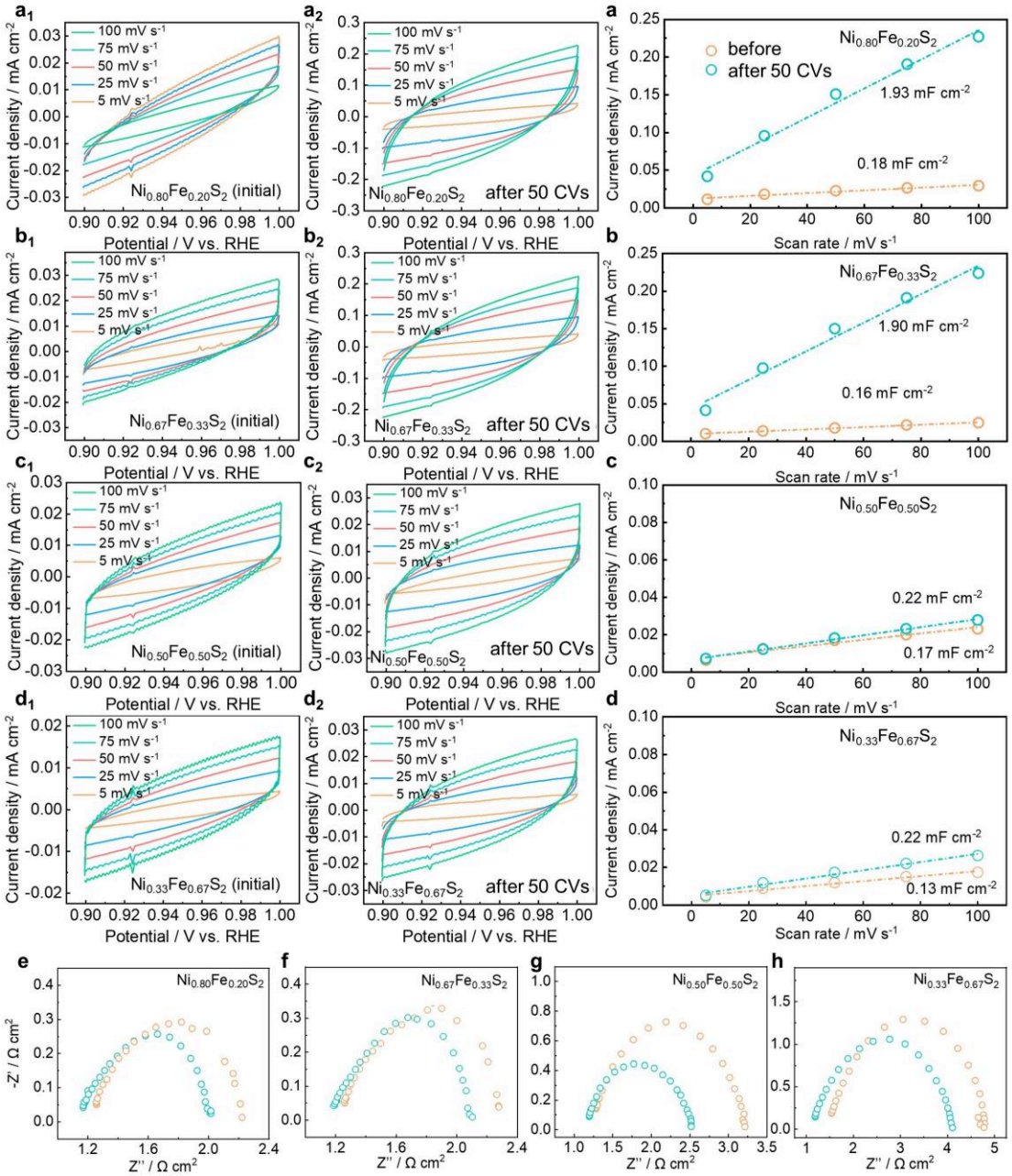

Fig. S67 | ECSA of $Ni_xFe_{1-x}S_2$ (x=0.33, 0.50, 0.67, 0.80) before and after 50 CVs. a, Double-layer capacitance measurements of $Ni_xFe_{1-x}S_2$ (x=0.33, 0.50, 0.67, 0.80) catalysts by cyclic voltammetry from 0.9~1.0 V vs. RHE at different scan rates from 5, 25, 50, 75, to 100 $mV \cdot s^{-1}$: **a_1, a_2,** $Ni_{0.67}Fe_{0.33}S_2$, **b_1, b_2,** $Ni_{0.67}Fe_{0.33}S_2$, **c_1-c_2,** $Ni_{0.50}Fe_{0.50}S_2$, **a-d,** slope of current density vs. scan rate and **e-h,** the corresponding EIS, respectively.

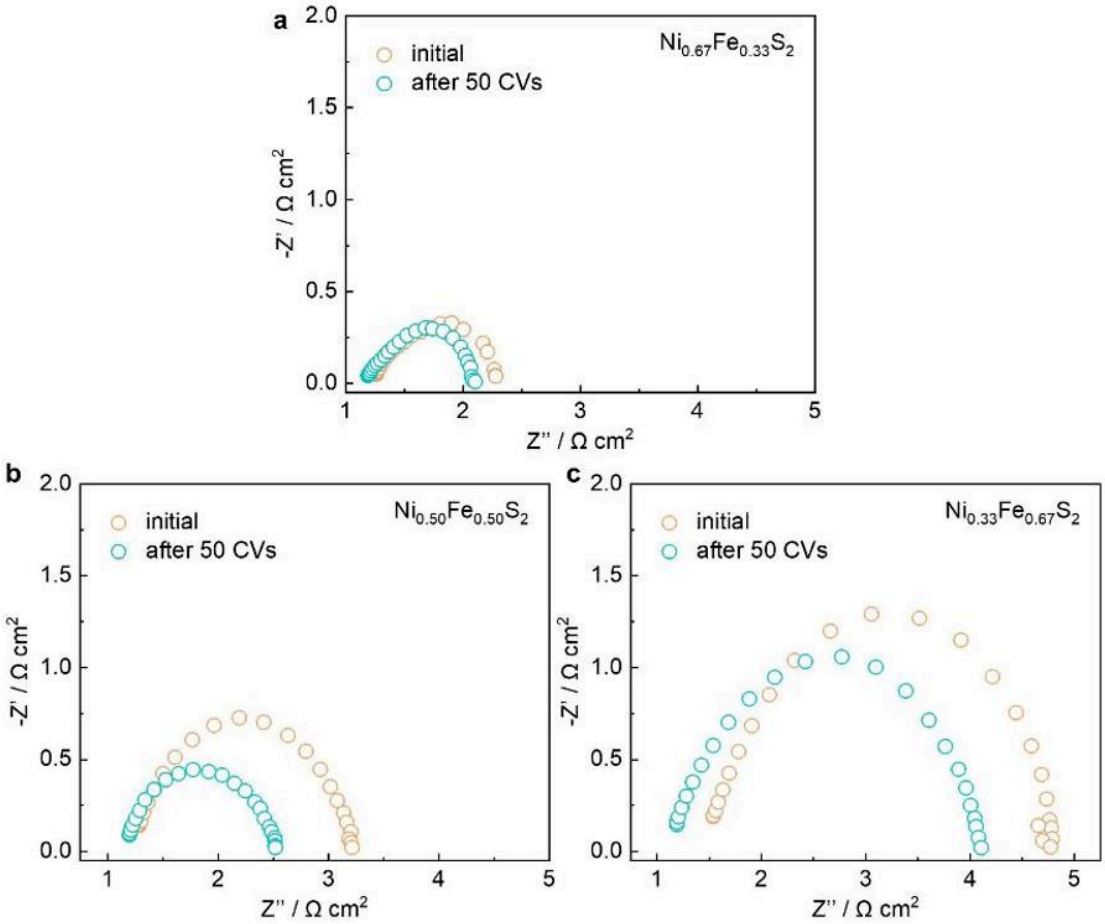

Fig. S68 | EIS of $Ni_xFe_{1-x}S_2$ (x=0.33, 0.50, 0.67) catalysts before and after 50 CVs. The curves were recorded at 1.6 V: **a,** $Ni_{0.67}Fe_{0.33}S_2$, **b,** $Ni_{0.50}Fe_{0.50}S_2$, and **c,** $Ni_{0.33}Fe_{0.67}S_2$.

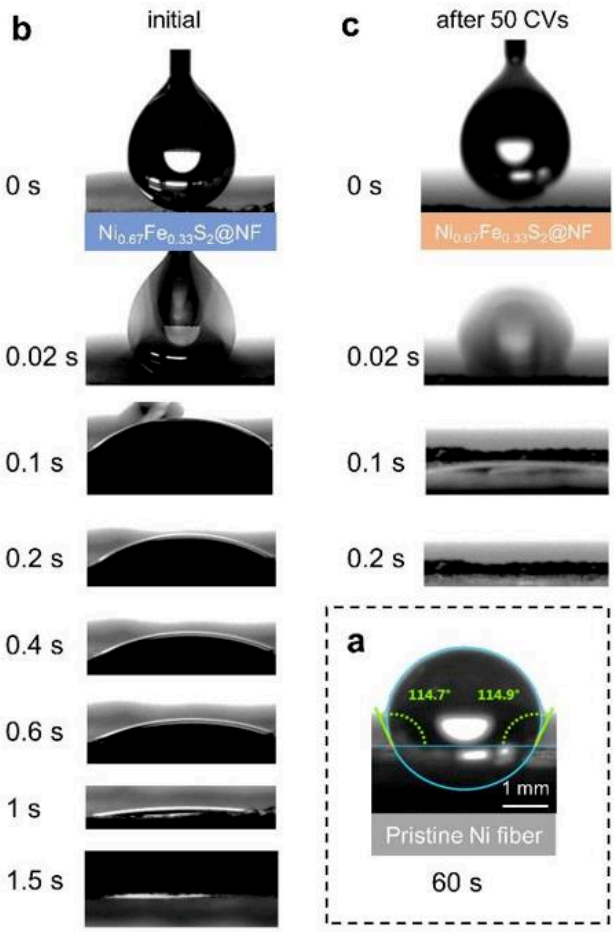

Fig. S69 | Water contact performance of the $Ni_{0.67}Fe_{0.33}S_2$ anode. Captured contact angles of **a,** pristine nickel fiber, **b, c,** $Ni_{0.67}Fe_{0.33}S_2$ coated nickel fiber before and after 50 CVs.

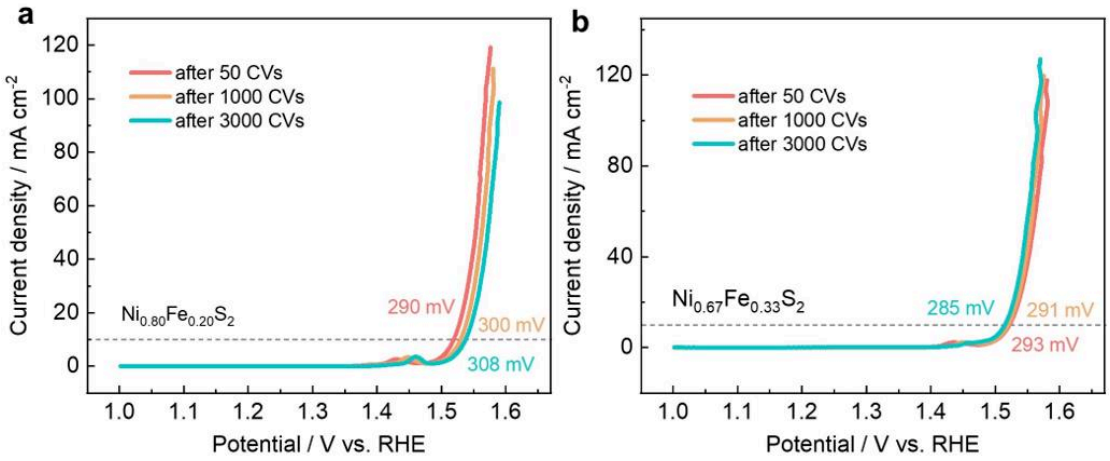

Fig. S70 | OER stability on the RDE. LSV curves of $Ni_{0.80}Fe_{0.20}S_2$ and $Ni_{67}Fe_{0.33}S_2$ after 50, 1000 and 3000 CVs. The $Ni_{0.80}Fe_{0.20}S_2$ shows performance decrease after 1000 CVs, while $Ni_{67}Fe_{0.33}S_2$ is stable for 3000 CVs).

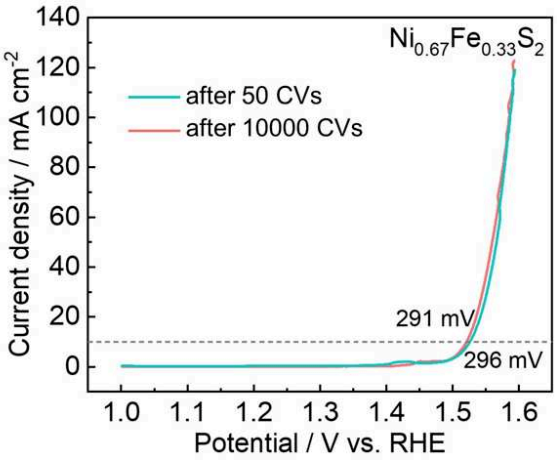

Fig. S71 | OER stability on the RDE. LSV curves of $Ni_{67}Fe_{0.33}S_2$ after 50 and 10000 CVs. The $Ni_{67}Fe_{0.33}S_2$ is stable for 10000 CVs.

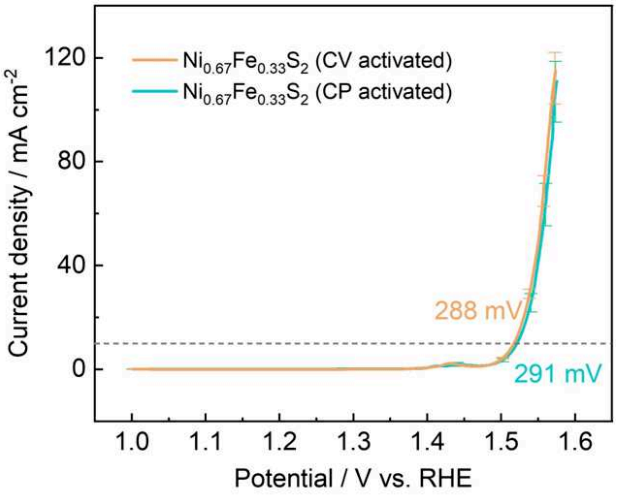

Fig. S72 | OER performance of $Ni_{67}Fe_{0.33}S_2$ on the RDE. LSV curves at 5 $mV \cdot s^{-1}$ of $Ni_{67}Fe_{0.33}S_2$ activated by CV in the range of 1.0-1.7 V for 50 cycles and CP at 1.7 V for 10 min.

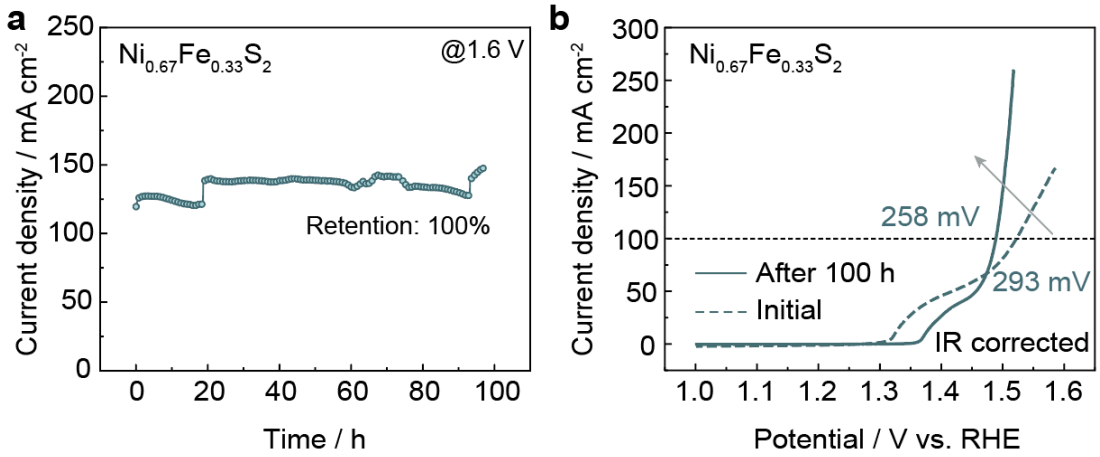

Fig. S73 | OER performance of $Ni_{67}Fe_{0.33}S_2$ (5 mg·cm^{-2}) on Ni fiber. **a,** Stability assessment of $Ni_{0.67}Fe_{0.33}S_2$-coated nickel fiber electrode at 1.6 V for 100 hours. **b,** Corresponding internal resistance (iR)-corrected LSV before and after the stability test.

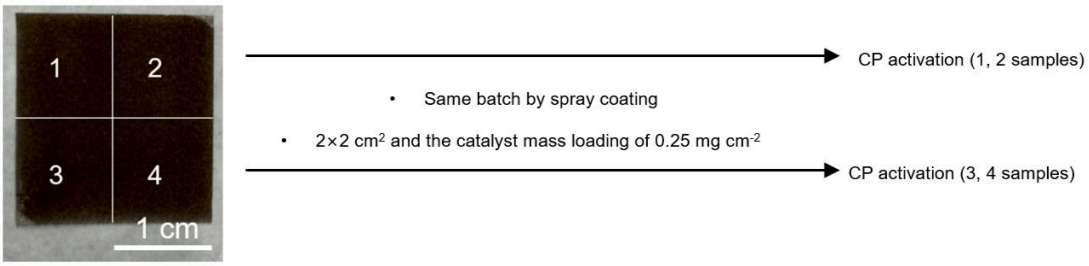

Fig. S74 | Sample preparation for broader comparison of CV and CP for catalysts beyond NiFe-based systems. All of the catalyst for broader adaptability was spray-coated onto 2×2 cm^2 Ni foam electrodes with a mass loading of 0.25 $mg \cdot cm^{-2}$, using the same batch of the electrode for consistency (1×1 cm^2 was used for each sample).

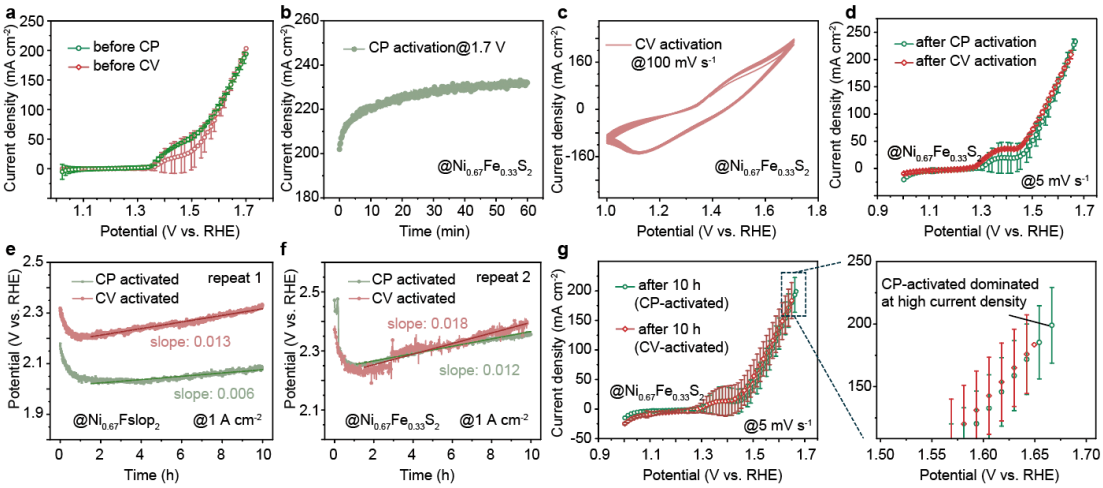

Fig. S75 | Electrochemical performance and stability of $Ni_{0.67}Fe_{0.33}S_2$ using CP and CV activation. a. LSV curves recorded before CP or CV activation, used as quality control. **b.** Current density versus time for a sample activated via CP at 1.7 V for 1 hour. **c.** Potential profile during CV activation of one typical sample, cycled between 1.0 and 1.7 V at a scan rate of 100 $mV \cdot s^{-1}$. **d.** LSV curves after CP or CV activation. **e, f.** Comparison of potential profiles between CP and CV-activated samples over a 10-hour period at 1 $A \cdot cm^{-2}$ in a three-electrode system (the slope was fitted from the lowest potential point to the final one). **g.** LSV curves for CP- and CV-activated samples after 10 hours of stability testing.

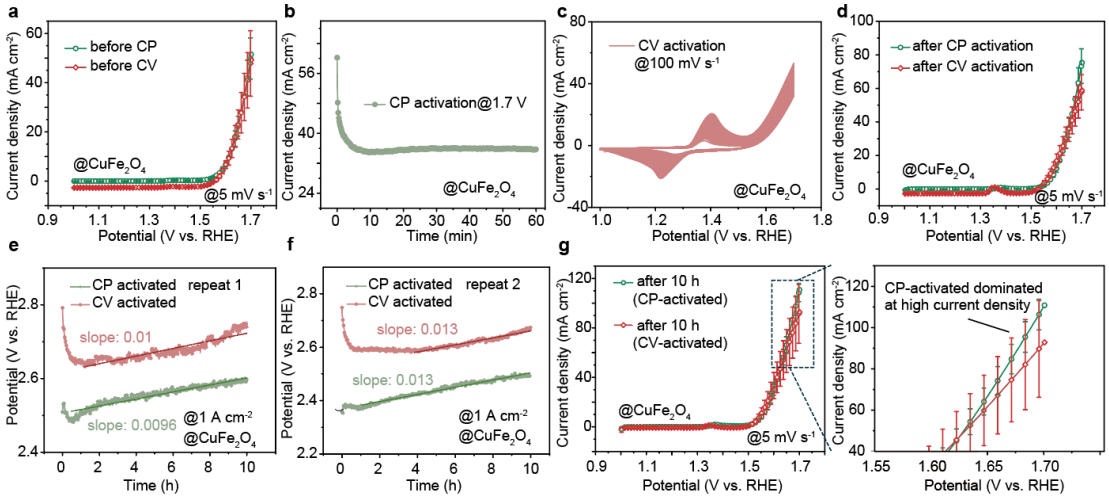

Fig. S76 | Electrochemical performance and stability of $CuFe_2O_4$ using CP and CV activation. a. Current density versus time for one sample activated via CP at 1.7 V for 1 h. **b.** CV activation of one example from 1.0-1.7 at 100 $mV \cdot s^{-1}$, illustrating the potential profile during cycling. **c, d.** Comparison of potential profiles between CP and CV activated samples over a 10-hour period at 1 $A \cdot cm^{-2}$ in a three electrode system, with the fitting range is from the lowest potential point to the last. **e, f.** Current density versus potential for a CP-activated and CV-activated sample, respectively.

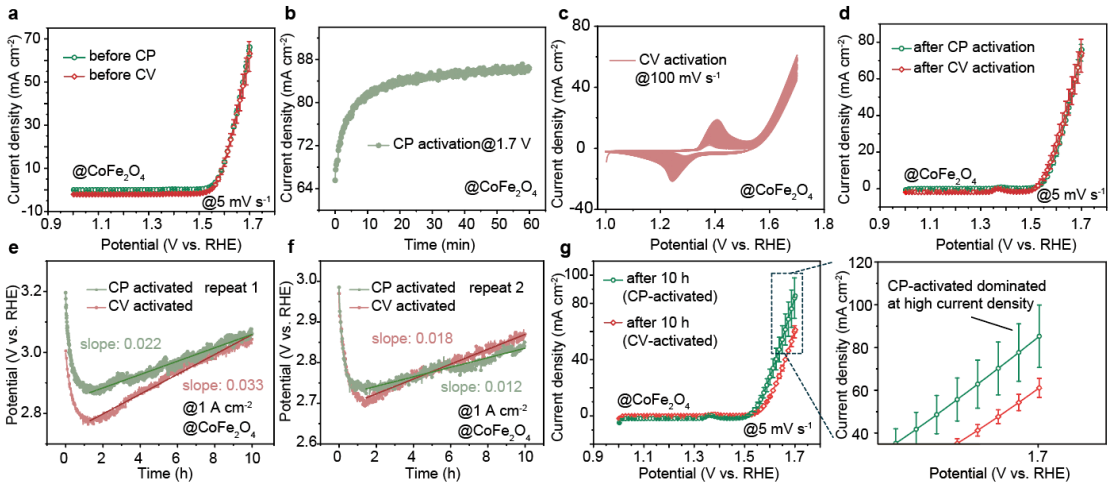

Fig. S77 | Electrochemical performance and stability of $CoFe_2O_4$ using CP and CV activation. a. Current density versus time for one sample activated via CP at 1.7 V for 1 h. **b.** CV activation of one example from 1.0-1.7 at 100 $mV \cdot s^{-1}$, illustrating the potential profile during cycling. **c, d.** Comparison of potential profiles between CP and CV activated samples over a 10-hour period at 1 $A \cdot cm^{-2}$ in a three electrode system, with the fitting range is from the lowest potential point to the last. **e, f.** Current density versus potential for a CP-activated and CV-activated sample, respectively.

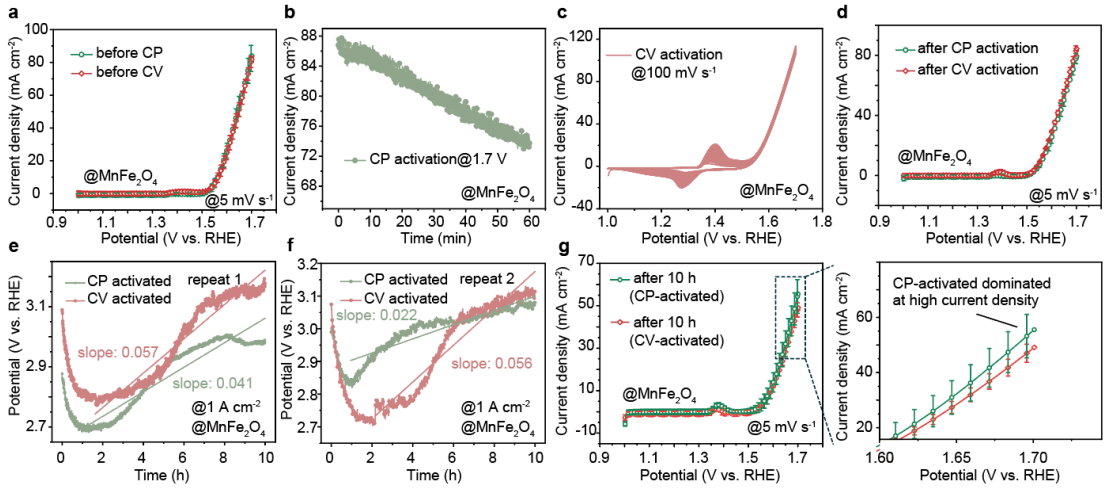

Fig. S78 | Electrochemical performance and stability of $MnFe_2O_4$ using CP and CV activation. a. Current density versus time for one sample activated via CP at 1.7 V for 1 h. **b.** CV activation of one example from 1.0-1.7 at 100 $mV \cdot s^{-1}$, illustrating the potential profile during cycling. **c, d.** Comparison of potential profiles between CP and CV activated samples over a 10-hour period at 1 $A \cdot cm^{-2}$ in a three electrode system, with the fitting range is from the lowest potential point to the last. **e, f.** Current density versus potential for a CP-activated and CV-activated sample, respectively.

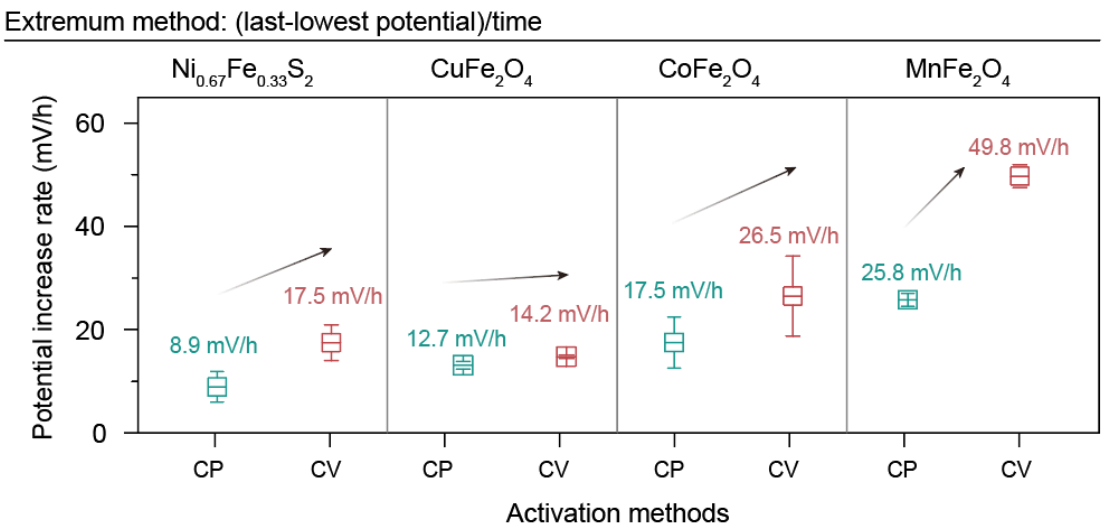

Fig. S79 | Summary of the potential increase rate (mV/h) from Fig. S75-78 (e, f panels). Two approaches were used for calculation: ***i)*** **Linear fitting (as shown in Figure 5a)**, where the rate was determined by fitting a line from the lowest potential point to the final point; and ***ii)*** **Extremum method**, where the difference between the lowest potential and the final potential was divided by the time period to obtain the rate.

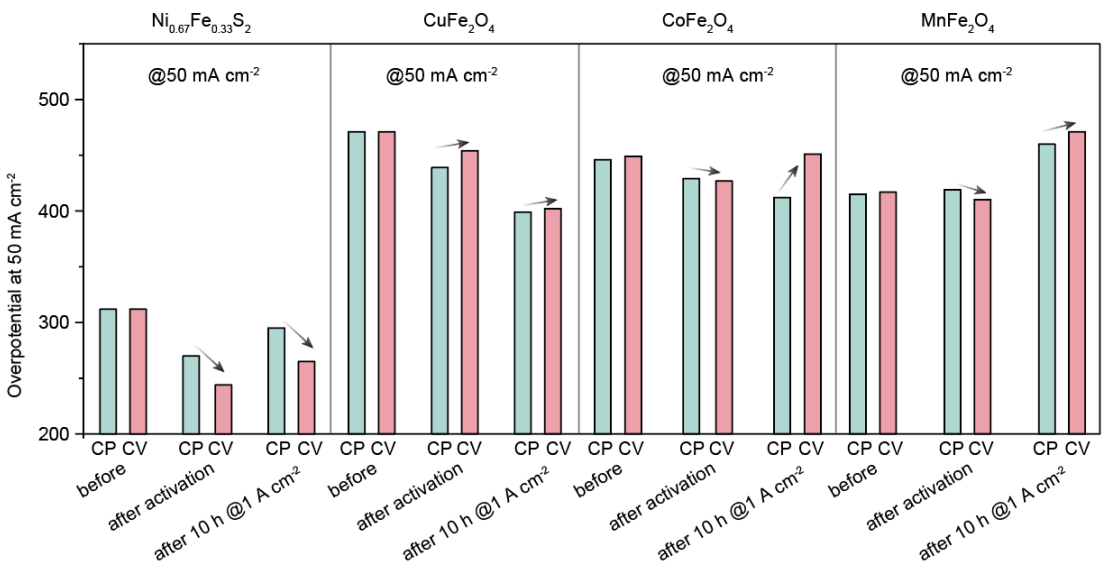

Fig. S80 | Summary of voltage penalty from Fig. S75-78 (a, d, g panels). Overpotential comparison at 50 mA·cm^{-2} for $CuFe_2O_4$, $CoFe_2O_4$, $MnFe_2O_4$, and $Ni_{0.67}Fe_{0.33}S_2$ after CP and CV activation.

Part 6: Activity and stability in full cells

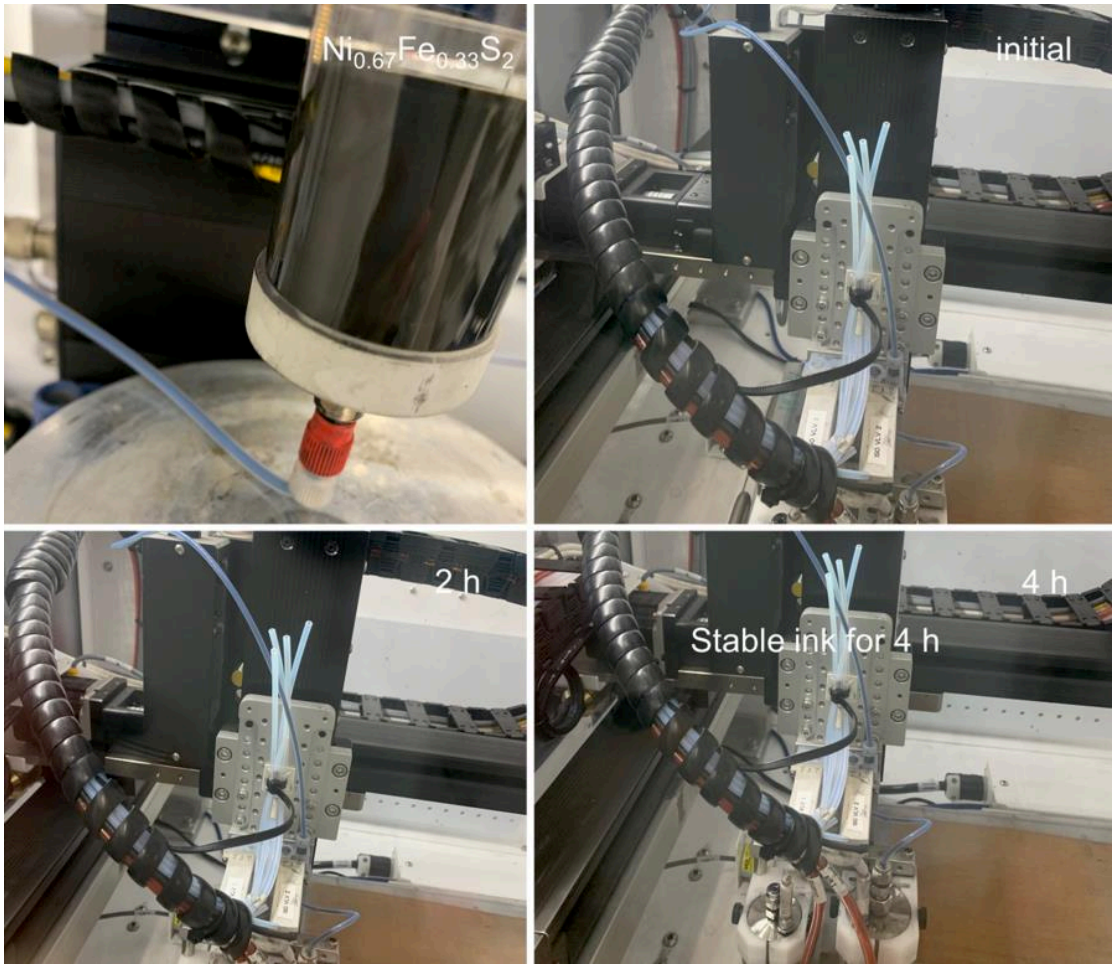

Fig. S81 | Ink stability and spray coating. The ink of $Ni_{0.67}Fe_{0.33}S_2$ is highly stable due to its nanostructure, without precipitation after 4 h spray coating.

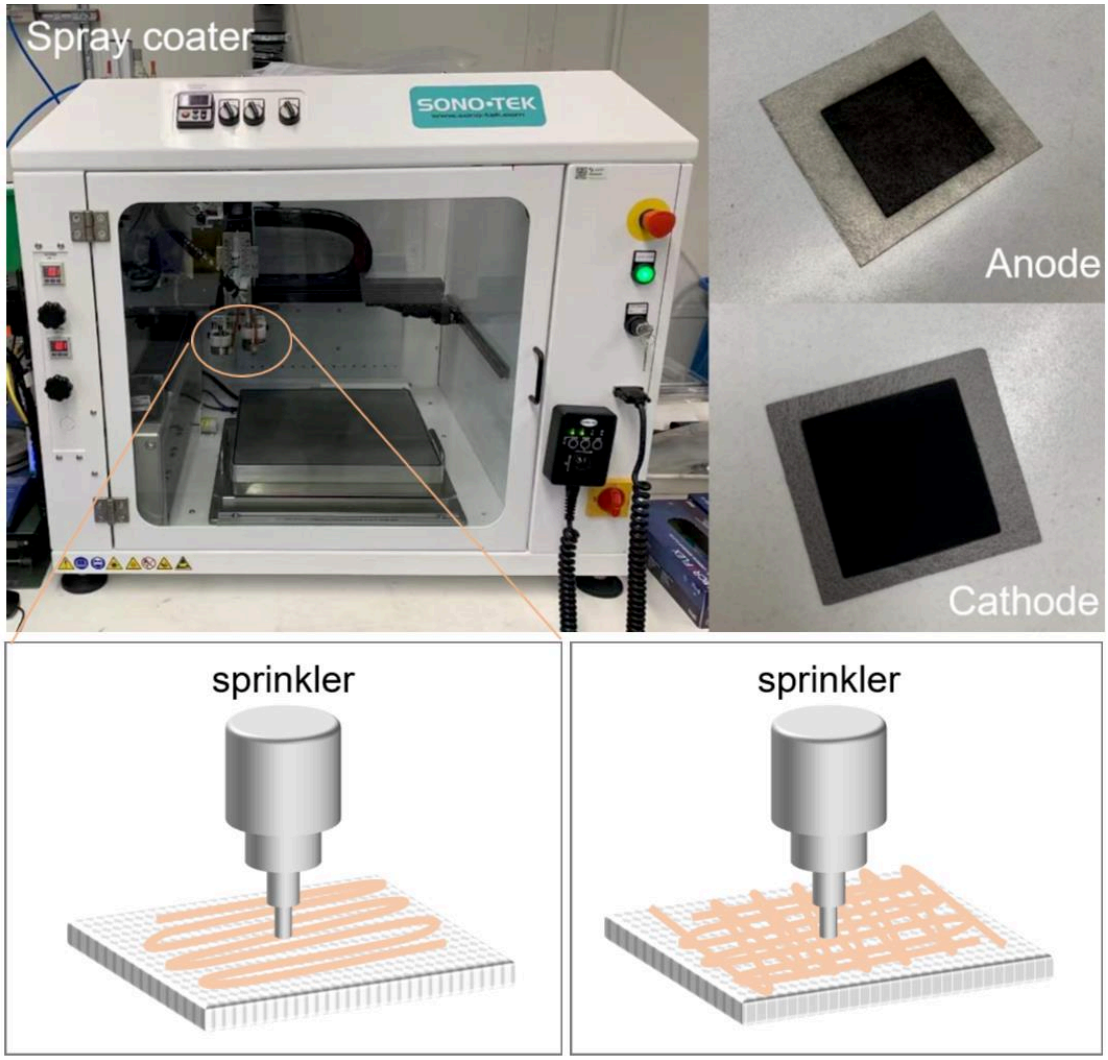

Fig. S82 | Spray coating processes. The ink of $Ni_{0.67}Fe_{0.33}S_2$ sprayed onto the nickel fiber by a commercial spray coater from SONO-TEK.

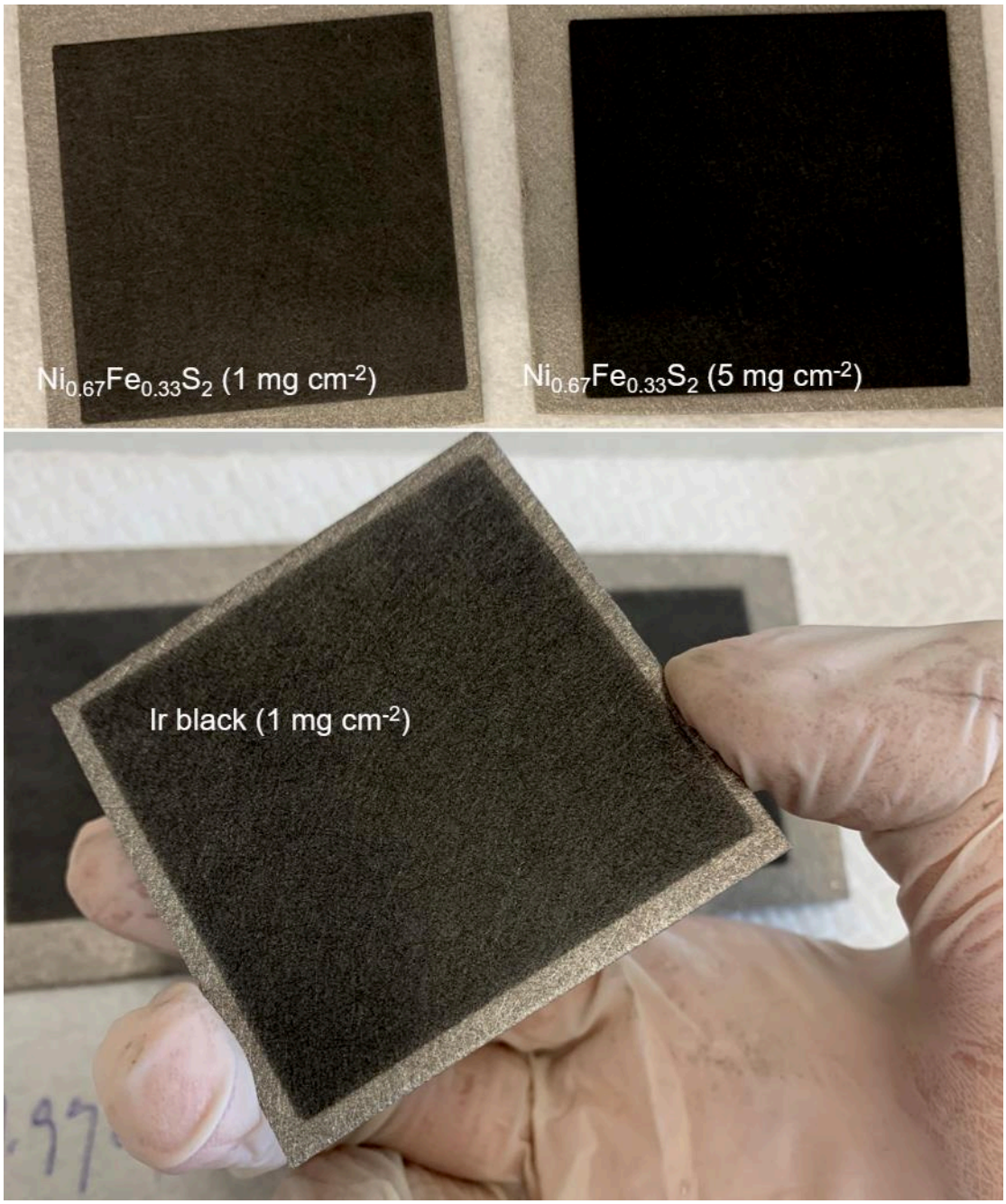

Fig. S83 | Sprayed coated anodes. The $Ni_{0.67}Fe_{0.33}S_2$ and Ir black coated anodes with different mass loading. Each sprayed anodes will be cut into 4 pieces for single-cell measurements.

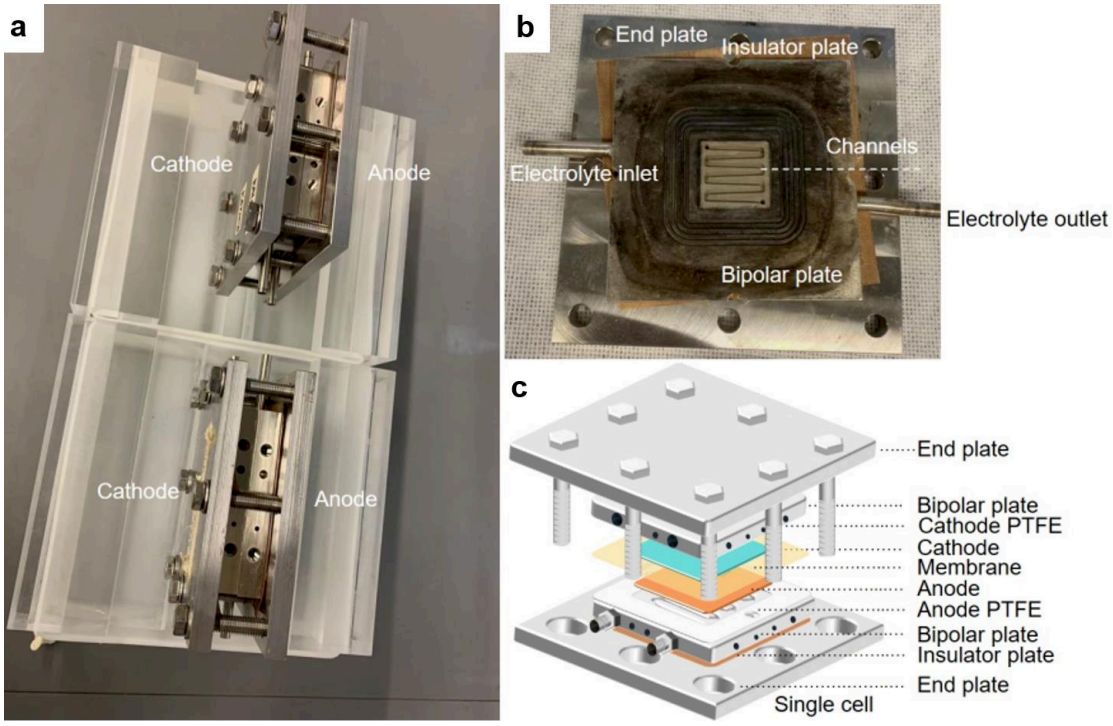

Fig. S84 | single cells and configuration. a, Photo of two single cells and **b,** current collector and flow channel, **c,** illustration of the configuration of a single cell.

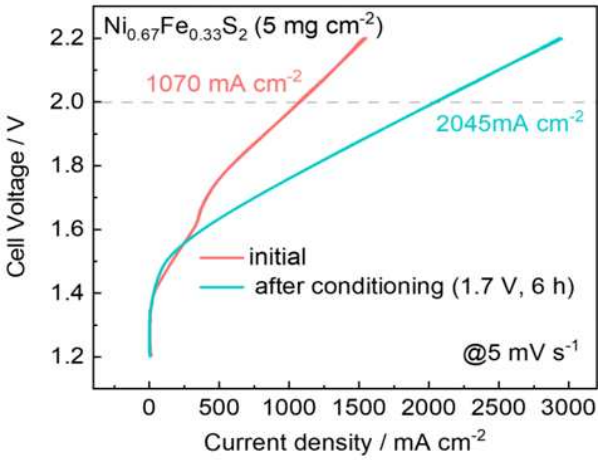

Fig. S85 | Full-cell performance of the $Ni_{0.67}Fe_{0.33}S_2$ based cells compared with commercial iridium black based ones. Polarization curves of the initial $Ni_{0.67}Fe_{0.33}S_2$-based cell and that of after conditioning at 1.7 V for 6 h in 1 M KOH at 60°C.

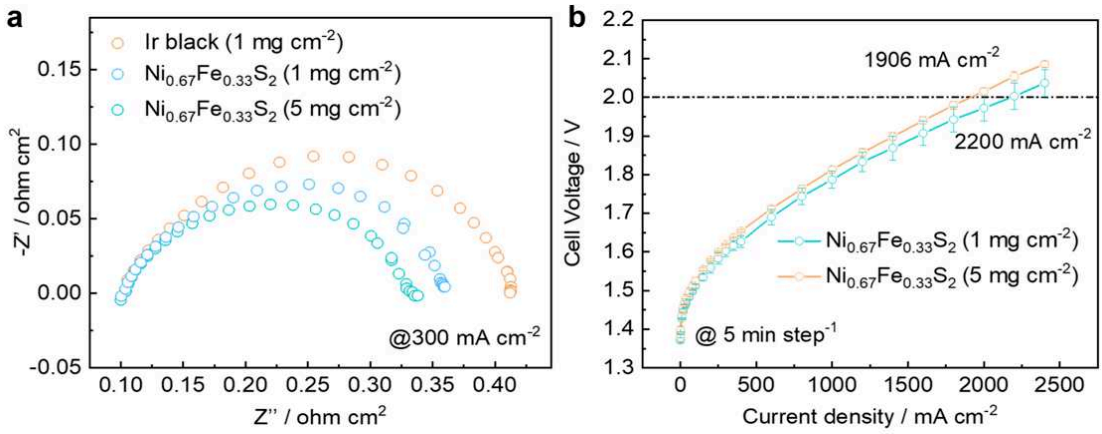

Fig. S86 | Full-cell performance of the $Ni_{0.67}Fe_{0.33}S_2$ based cells compared with commercial iridium black based ones. a, EIS plots of iridium black- (1 mg·cm^{-2}) and $Ni_{0.67}Fe_{0.33}S_2$- (1 or 5 mg·cm^{-2}) based cells at 300 mA·cm^{-2}. **b,** Polarization curves of $Ni_{0.67}Fe_{0.33}S_2$-based cells with different mass loadings of 1 and 5 mg·cm^{-2}.

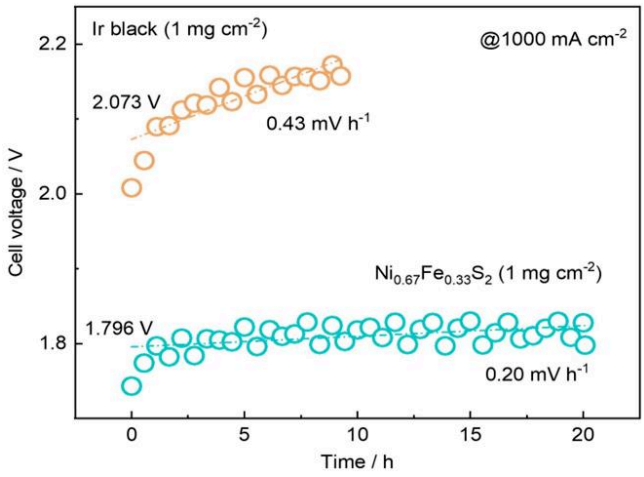

Fig. S87 | Short-term stability. Stability of $Ni_{0.67}Fe_{0.33}S_2$ based cells compared with commercial iridium black based ones for 20 h at 1000 mA·cm^{-2}. Iridium based cells show doubled voltage increase rate of 0.43 mV·h^{-1} than that of the $Ni_{0.67}Fe_{0.33}S_2$ counterpart.

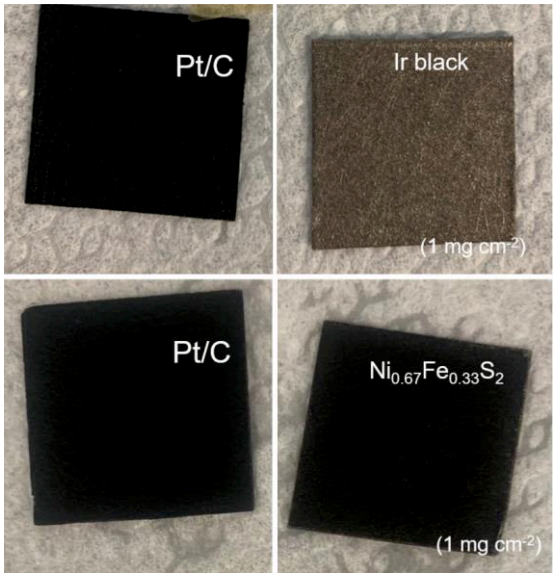

Fig. S88 | Electrodes after electrolysis. The photos of Pt/C, Ir black and $Ni_{0.67}Fe_{0.33}S_2$ after a short-term electrolysis. The Ir black was unstable in alkaline conditions and was washed out into the electrolyte.

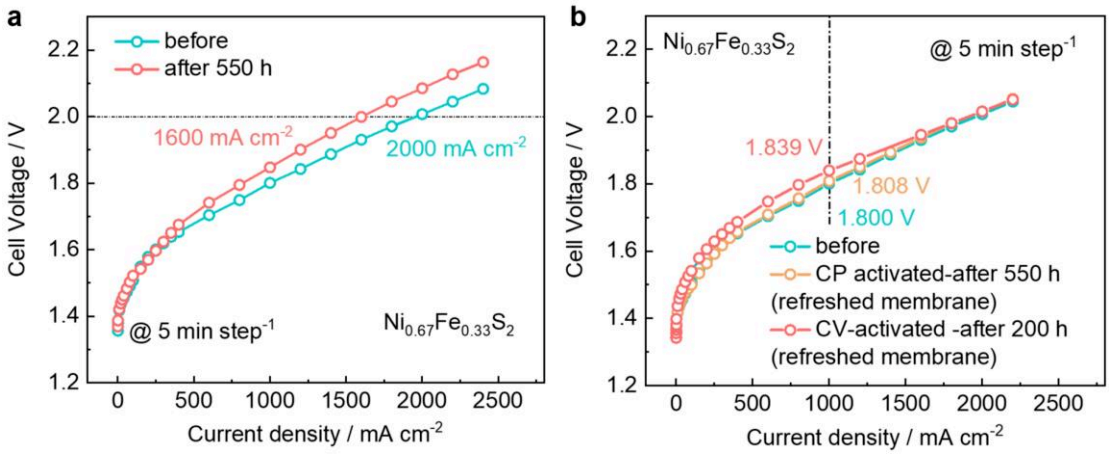

Fig. S89 | Full-cell polarization curves of the $Ni_{0.67}Fe_{0.33}S_2$ based cells before and after stability tests. a, Polarization curves of the cells based on Pt/C||AF1-HNN8-50||$Ni_{0.67}Fe_{0.33}S_2$-CP activated before and after 550 h and **b,** before and after membrane refreshing (CP-activated after 550 h and CV-activated after 200 h), only refreshing the membrane with a newly pretreated one, and keep other conditions unchanged).

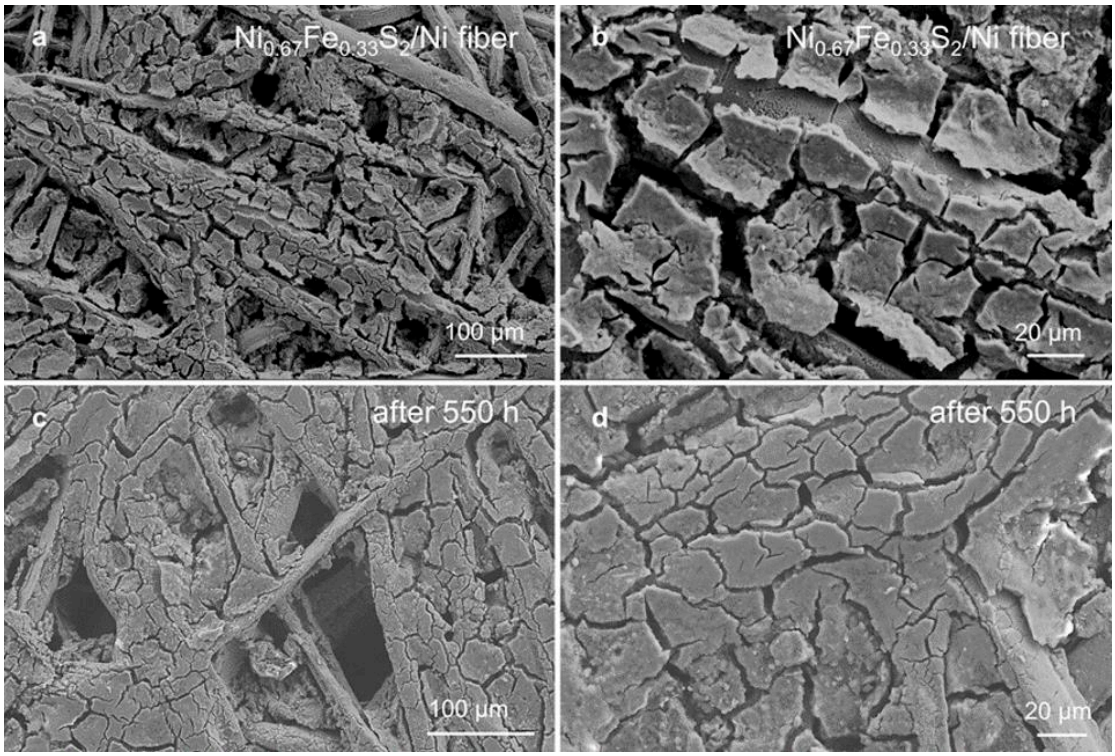

Fig. S90 | Surface Morphology of the $Ni_{0.67}Fe_{0.33}S_2$ anode. SEM of **a, b,** initial $Ni_{0.67}Fe_{0.33}S_2$ coated Ni fiber, consisting of big catalyst/ionomer clusters (~20 μm) due to ink dispersion issue and high mass loading, and **c, d,** $Ni_{0.67}Fe_{0.33}S_2$ coated Ni fiber after 550 h at 1000 $mA \cdot cm^{-2}$.

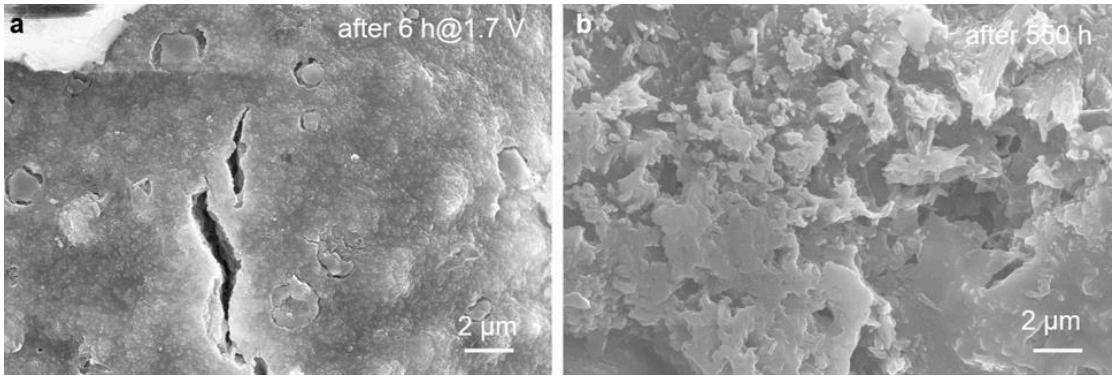

Fig. S91 | Surface Morphology of the $Ni_{0.67}Fe_{0.33}S_2$ anode. SEM of **a,** $Ni_{0.67}Fe_{0.33}S_2$ coated Ni fiber after 6 h at 1.7 V and **b,** after 550 h at 1000 $mA \cdot cm^{-2}$.

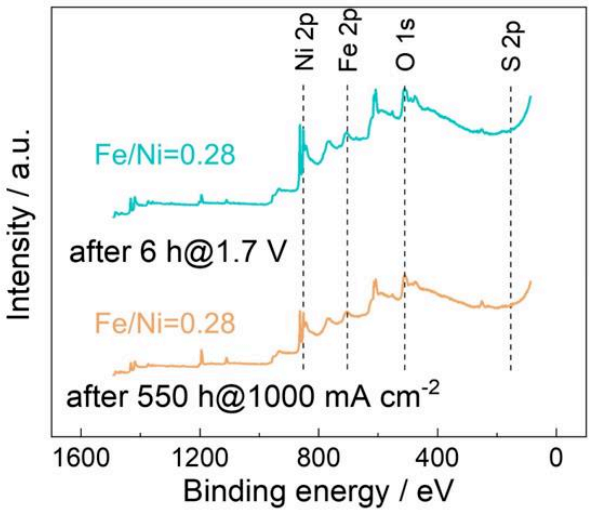

Fig. S92 | XPS survey. XPS survey of the $Ni_{0.67}Fe_{0.33}S_2$ coated nickel fiber electrodes after conditioning at 1.7 V for 6 h, after 550 h at 1000 mA·cm^{-2}.

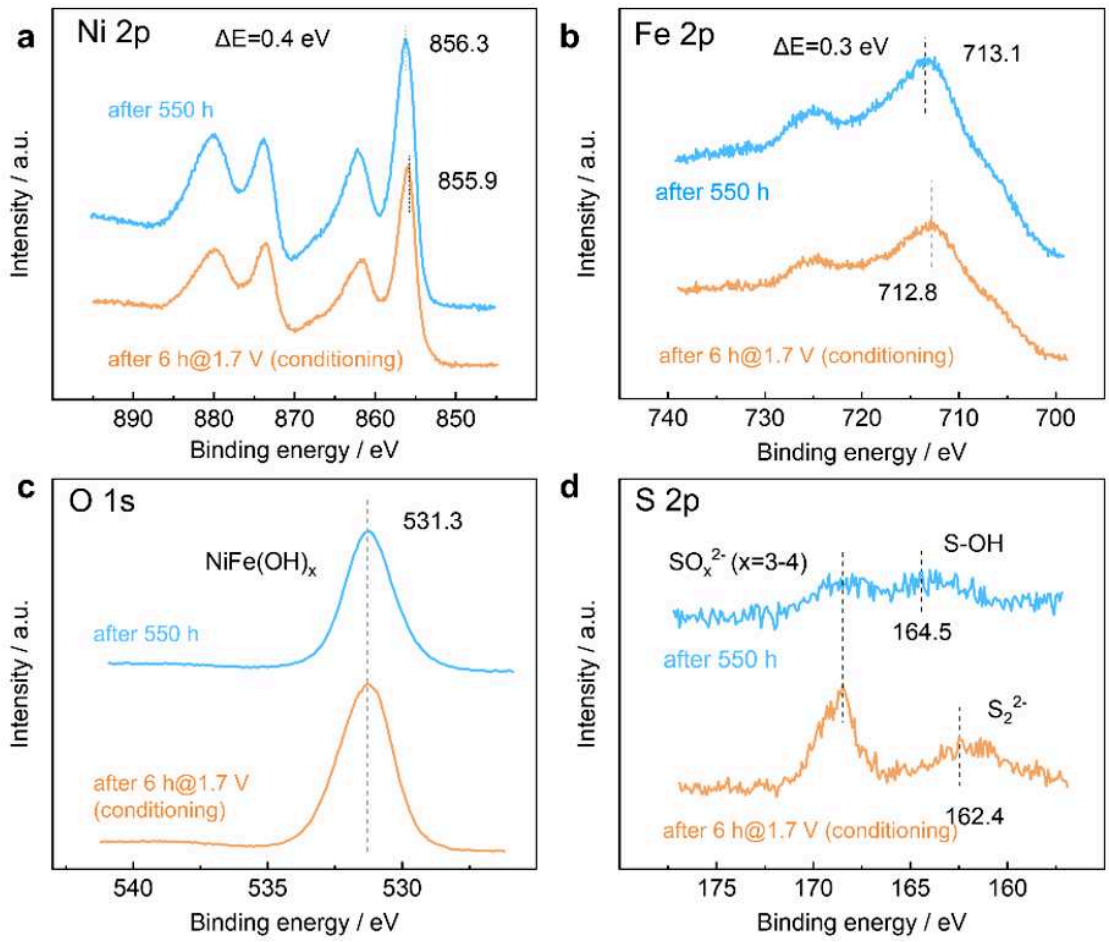

Fig. S93 | Surface chemical state of the $Ni_{0.67}Fe_{0.33}S_2$ anode before and after 550 h. High-resolution XPS spectra of $Ni_{0.67}Fe_{0.33}S_2$ coated on the nickel fiber in **a,** Ni 2p and **b,** Fe 2p, **c,** O 1s, and **d,** S 2p regions after conditioning at 1.7 V for 6 h and 550 h at 1000 mA·cm^{-2}.

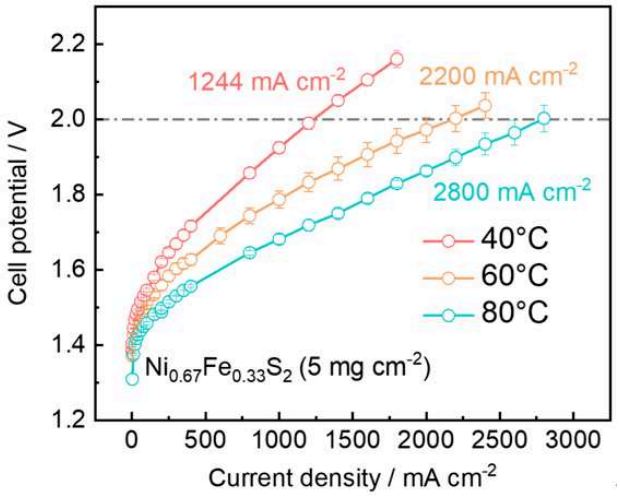

Fig. S94 | Full-cell performance at different temperature of the $Ni_{0.67}Fe_{0.33}S_2$ based cells. Polarization curves of the cells based on Pt/C||AF1-HNN8-50||$Ni_{0.67}Fe_{0.33}S_2$ at different temperatures from 40, 60 to 80℃ after conditioning.

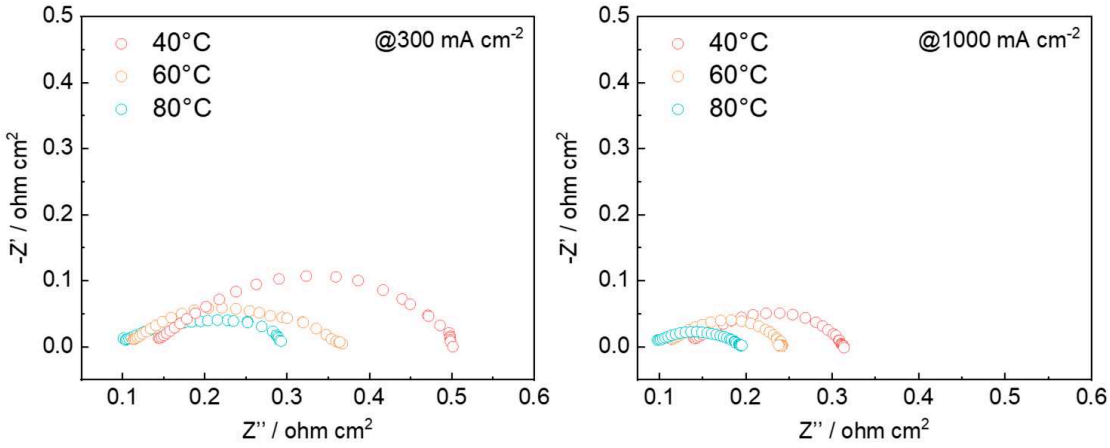

Fig. S95 | EIS at different temperature and current density. EIS of the cells based on Pt/C||AF1-HNN8-50||$Ni_{0.67}Fe_{0.33}S_2$ at different temperatures from 40, 60 to 80℃ after conditioning at different current densities from 300 to 1000 mA·cm^{-2}.

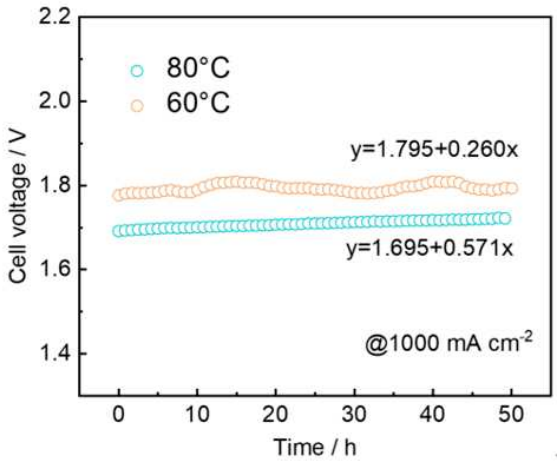

Fig. S96 | Stability at different temperature. Short-term stability test of $Ni_{0.67}Fe_{0.33}S_2$ for 50 h at 60 and 80°C under 1000 mA·cm^{-2}. The membrane stability limited the application of high-temperature AEMWE.

The first-generation AF1-HNN8-50 membrane is much more unstable at higher temperature, causing more than two times higher cell voltage increase rate (0.571 mV·h^{-1}, **Suppl. Fig. 96**) at 80°C than that at 60°C (0.260 mV·h^{-1}). Therefore, membrane materials, with high-temperature stability, are crucial to improve the electrolysis efficiency in the future, further releasing the potential of programed activation for electrocatalysts.

References

1. Pan, G. X., Cao, F., Xia, X. H. & Zhang, Y. J. Exploring hierarchical FeS_2/C composite nanotubes arrays as advanced cathode for lithium ion batteries. *J. Power Sources* **332**, 383–388 (2016).

2. Bastola, E., Bhandari, K. P. & Ellingson, R. J. Application of composition controlled nickel-alloyed iron sulfide pyrite nanocrystal thin films as the hole transport layer in cadmium telluride solar cells. *J. Mater. Chem. C* **5**, 4996–5004 (2017).

3. Boursiquot, S., Mullet, M. & Ehrhardt, J.-J. XPS study of the reaction of chromium (VI) with mackinawite (FeS). *Surf. Interface Anal.* **34**, 293–297 (2002).

4. Thangasamy, P., Maruthapandian, V., Saraswathy, V. & Sathish, M. Supercritical fluid processing for the synthesis of NiS_2 nanostructures as efficient electrocatalysts for electrochemical oxygen evolution reactions. *Catal. Sci. Technol.* **7**, 3591–3597 (2017).

5. Nesbitt, H. W., Legrand, D. & Bancroft, G. M. Interpretation of Ni2p XPS spectra of Ni conductors and Ni insulators. *Phys. Chem. Miner.* **27**, 357–366 (2000).

6. Chen, X. *et al.* Sulfur-doping/leaching induced structural transformation toward boosting electrocatalytic water splitting. *Appl. Catal. B* **305**, 121030 (2022).

7. Pallassana, V., Neurock, M., Hansen, L. B., Nørskov, J. K. *et al.*, First principles analysis of hydrogen chemisorption on Pd-Re alloyed overlayers and alloyed surfaces. *J. Chem. Phys.* **112**, 5435–5439 (2000).

8. Hammer, B. Nørskov, J. K. *et al.*, Theoretical surface science and catalysis—calculations and concepts. *Adv. Catal.* **45**, 71-129 (2000).